AN EXPERIMENTAL STUDY OF THE FLOW FIELD SURROUNDING A SUBSONIC JET IN A CROSS FLOW

A Thesis

Presented to the Faculty of

California Polytechnic State University

San Luis Obispo

In Partial Fulfillment

of the Requirements for the Degree of

Master of Science in Aeronautical Engineering

by

Robert Foster Dennis

June 1993

APPROVAL PAGE

TITLE : An Experimental Study of the Flow Field Surrounding a Subsonic Jet in a Cross Flow

AUTHOR : Robert Foster Dennis

DATE SUBMITTED : June 1993

Dr. Jin Tso
Thesis Advisor

Prof. Jon A. Hoffmann
Committee Member

Mr. Richard J. Margason
Committee Member

Dr. Russell M. Cummings
Department Head

ABSTRACT

AN EXPERIMENTAL STUDY OF THE FLOW FIELD SURROUNDING A SUBSONIC JET IN A CROSS FLOW

Robert Foster Dennis

June 1993

An experimental investigation of the flow interaction of a 5.08 cm (2.00 in.) diameter round subsonic jet exhausting perpendicularly to a flat plate in a subsonic crossflow was conducted in the NASA Ames 7x10 Ft. Wind Tunnel No. 1. Flat plate surface pressures were measured at 400 locations in a 30.48 cm (12.0 in.) concentric circular array surrounding the jet exit. Results from these measurements are provided in tabular and graphical form for jet-to-crossflow velocity ratios ranging from 4 to 12, and for jet exit Mach numbers ranging from 0.50 to 0.93. Laser Doppler Velocimeter (LDV) three component velocity measurements were made in selected regions in the developed jet plume and near the flat plate surface, at a jet Mach number of 0.50 and jet-to-crossflow velocity ratios of 6 and 8. The results of both pressure and LDV measurements are compared with the results of previous experiments. In addition, pictures of the jet plume shape at jet velocity ratios ranging from 4 to 12 were obtained using schleiren photography. The LDV measurements are consistent with previous work, but more extensive measurements will be necessary to provide a detailed picture of the flowfield. The surface pressure results compare closely with previous work and provide a useful characterization of jet induced surface pressures. The results demonstrate the primary influence of jet velocity ratio and the secondary influence of jet Mach number in determining such surface pressures.

ACKNOWLEDGEMENTS

I would like to express my gratitude to the people who helped make this project possible and made my learning experience at Ames enjoyable, and in particular Dr. Jin Tso, of Cal Poly; and Mr. Richard J. Margason and Dr. W. Clif Horne of NASA/Ames Research Center. I would also like to thank Stephane Couillaud, Donald Cooper, and the many people of the Full Scale Aeronautics Division for their collaboration, assistance and companionship. The thesis research was supported by NASA-Ames through Grant #NCC 2-731.

TABLE OF CONTENTS

LIST OF FIGURES

List of Tables

LIST OF SYMBOLS AND ABBREVIATIONS

Symbols.

C_p	Induced coefficient of pressure due to jet
D	Jet diameter at exit
M_j	Jet Mach number at exit
R	Effective velocity ratio, $(V_j/ V_\infty) * \sqrt{(\rho_j/\rho_\infty)}$
Rn_D	Reynolds number based on diameter and freestream velocity
r	Radial location of pressure port from jet centerline
V	Velocity
V_e	Effective velocity ratio, 1/R
x, y, z	Cartesian coordinates relative to jet centerline and plate surface: x positive streamwise, z positive up, y positive to left
x_p, y, z_p	Rotated and translated coordinates of cross sectional plane
Δx	Interference fringe spacing
α	Angle of pitch on y axis of cross sectional plane
ϕ	Half-angle of convergence of laser beam pair
λ	Wavelength of laser light
θ	Angular location of pressure port, clockwise from leading edge
ρ	Density

Subscripts.

∞	Indicates freestream condition
j	Indicates jet exit condition

Abbreviations.

CFD	Computational fluid dynamics
JICF	Jet in a crossflow
LDV	Laser Doppler velocimeter
SWTS	Standard Wind Tunnel System, 7x10 foot Wind Tunnel No. 1
VSTOL	Vertical / short takeoff and landing

CHAPTER 1

Introduction

1.1 Objectives and Motivation

The present investigation was performed as a thesis study in partial fulfillment of the requirements for the degree of Master of Science in Aeronautical Engineering of the California Polytechnic State University, San Luis Obispo.

Flowfield Study. The first goal of this study was to provide improved data describing the surface pressure patterns and flowfield velocities created by the interaction of a round subsonic jet exhausting perpendicularly from a flat plate in a subsonic crossflow (Jet-In-Cross-Flow, or JICF). The motivation for acquiring this data was to assist in the evaluation of computational fluid dynamics (CFD) codes applied to this flow interaction.

The Fixed Wing Aerodynamics Branch and the Applied Computational Fluids Branch of National Aeronautics and Space Administration (NASA) Ames Research Center are participating in a combined experimental/CFD program to validate computational methods for complex jet flows. This goal required data of sufficient detail and quality to evaluate the capability of CFD to predict important flow parameters. A database was also needed for improving the modelling capability of OVERFLOW or other CFD algorithms.

The available data was generally not adequate to provide meaningful comparisons between theory and experiment. Additional grant support was therefore provided towards the goal of obtaining a sufficient data base. A first phase of this project was completed in 1989 by Karlin Roth with an experimental investigation of surface pressure patterns

resulting from lift jets exhausting beneath a delta wing aircraft model. A CFD investigation by Roth of the model flowfield is currently underway.

Grant support was approved in 1991 to conduct the present study as a continuation of this work. The grant was directed towards obtaining a data base for a geometrically simple JICF model. At the same time, support for a CFD study of the same configuration was approved. This CFD study was conducted from 1991 to 1993 by Stephen Chiu, Richard Margason, and Jin Tso.

Laser Doppler Velocimetry. The second goal was to complete, calibrate and evaluate the performance of a three dimensional orthogonal fixed-focus laser Doppler velocimetry (LDV) system. The LDV system had been previously designed and fabricated at NASA Ames Research Center to be installed as dedicated instrumentation for the NASA Ames Research Center 7x10 Foot Wind Tunnel No. 1. A versatile 3-D LDV system is highly desirable for obtaining experimentally a detailed overall description of the complex pattern of separated shear structures and vortices involved in jet flows.

Previously, a three dimensional non-orthogonal zoom focus portable LDV system was developed for the 7x10 Foot tunnel using backscatter signals for each component. This system was developed and used successfully at NASA/Ames by Phillip Snyder, Kenneth Orloff and Kiyoshi Aoyagi. However, it was recognized that there were certain inherent limitations of the system due to its backscatter receiving optics and the small out-of-plane angle used to resolve the third component of velocity.

To address these limitations, an orthogonal fixed-focus 3-D LDV system was designed using separate large aperture forward-scatter receiving optics and a permanently mounted traverse system. The system was to use the laser, motor controllers and signal processing hardware of the previous system. The new optical and traverse subsystems were designed and fabricated at NASA Ames Research Center by Steve Dunagan and Clif Horne. Although the optics had been previously tested in the laboratory, the LDV system

had not been assembled or used prior to this test. In addition, the control software coding and interface needed to be completed for the system to be fully functional.

Although not the subject of this thesis, an additional investigation was prepared and conducted in conjunction with the current investigation by Stephane Couillaud, a San Jose State University graduate student, using much of the same experimental hardware. This study used the JICF model as a jet source and symmetry plane for an investigation of spanwise blowing along the leading edge of a highly tapered trapezoidal wing, and used LDV measurements, flow visualization, and panel method computation. The wing was mounted perpendicularly to the flat plate with the jet exhausting tangentially to the upper surface of the wing. Mr. Couillaud and the author collaborated on those aspects of the preparation for each investigation which involved common equipment and resources, including the completion of the LDV data acquisition program, model preparation, and LDV system preparation and calibration.

1.2 The Present Study.

Chapter 1 includes a review of prior research on the aerodynamics of the JICF. Chapter 2 contains a description of the experimental model, the wind tunnel, high pressure air system, and related instrumentation. Chapter 3 contains a description of the specific hardware and instrumentation used to study the surface pressure distribution, the experimental methods, and a discussion of the experimental results. Chapter 4 describes the equipment used to obtain schlieren photographs of the JICF and a discussion of these photographs. Chapter 5 contains a description of the specific hardware and instrumentation used to obtain LDV measurements of the flowfield, the experimental methods, and a discussion of the experimental results.

1.3 Prior Jet-In-Cross-Flow Research

General Features. The characteristics of a jet-in-a-crossflow have been the subject of a substantial body of study over a period of many years, due to the importance of these

phenomena to a number of practical applications, including vertical/short takeoff and landing aircraft (V/STOL) in transitional flight, reaction control, fluid dispersion, and combustion. A comprehensive survey of JICF research has been done recently by Margason [1] covering experimental and computational work over the last fifty years.

Figure 1.1 shows the general flowfield features created by a circular jet exhausting perpendicularly into a crossflow. The dominant feature is the deflection of the jet downstream into a curved path by the pressure and shearing forces exerted on the jet by the mean flow. The deflection of the jet is accompanied by the distortion of the jet cross-section and the creation of lateral counter-rotating vortices due to the shearing action of the mean flow on the jet boundary. The shear layers so formed progressively roll up into a pair of vortices which propagate below and to the sides of the centerline of the curve jet path. Figure 1.2 depicts an analytical solution of the evolution of the vortex pair by Margason [2]. The potential core of the jet decays rapidly, and the vortex pair becomes the primary jet plume feature within a few jet diameters.

A secondary feature is a horseshoe vortex at the plate surface created by the deflection and rolling up of the plate boundary layer by the jet. Behind the horseshoe vortex is a complex and unsteady wake region. The flow in this wake region reflects the combined effects of flow entrainment by the jet and the shedding of vortices as the cross flow separates from the jet near the jet trailing edge [3,4] (see Figures 5.12 and 5.13)

Correlation Parameter. The effective velocity ratio has been established as the most suitable parameter for correlating the effect of variation in size, density, and velocity in the jet-in-a-crossflow. This is defined as:

$$R = (V_j / V_\infty) * \sqrt{(\rho_{jt}/\rho_\infty)} \qquad \text{(Equation 1.1)}$$

and can be seen to be the square root of the ratio of the jet and freestream dynamic pressures. Work by Williams and Wood [5] has shown that this parameter effectively accounts for the effect of variations in density and temperature between jet and freestream,

and is a more suitable parameter than a simple ratio of velocity. The reciprocal of **R** is also widely used ($\mathbf{1/R = V_e}$). $\mathbf{V_e}$ is a convenient parameter for describing VSTOL transition flight, since it is zero at hover, whereas **R** becomes infinite at hover.

Jet Trajectory. A number of empirical and analytical studies have related the jet trajectory as a function of effective velocity ratio, jet exit angle, vertical and horizontal distance [1]. The jet trajectory is here defined as the locus of points of maximum velocity on the plane of symmetry in the jet plume. These empirical and analytical expressions have been summarized and evaluated by Margason [6] and Smy and Ransom [7]. For a perpendicular exit, the following relationship by Wooler has been shown to realistically predict jet trajectory:

$$x/D = 2.63\ (V_e)^2\ (z/D)^2 \qquad \text{(Equation 1.2)}$$

Similar expressions have been used to characterize jet trajectory for non-perpendicular jet exits [6, 7].

Induced Pressures. The pressure distribution induced by a JICF has been studied by a number of investigators [8, 9,10]. A comparison of experimental results [1] shows that transducer uncertainties are significant in areas with shallow pressure gradients. Figure 1.3 shows that the discrepancy between experimental results is greatest in the wake region behind the jet exit. The results by Fearn and Weston [9] show a larger negative pressure region, possibly due to higher Reynolds numbers.

Velocity Profiles and LDV. Velocity profiles of the developed jet plume were measured by Fearn and Weston [11, 12]. Figure 1.4 shows a vector/contour plot from reference 11. The plot is of a cross-sectional plane at an angle approximately normal to the jet trajectory. The centerline can be seen to be about 3 jet diameters above the vortex core in this section. In addition LDV studies have demonstrated the ability of this instrument to obtain flowfield data [3, 13]

CFD Studies. CFD studies using finite difference representations of the Navier-Stokes equations have been used effectively to characterize a large portion of the JICF velocity and pressure field[1]. However, such solutions show significant discepancies when compared to experimental data in the region on the near-surface wake. A recent study by Chiu, et al.[15], used separate grids to represent the jet plume and the surrounding flowfield, with the solutions being interpolated by the Chimera technique [31]. The paper compares the effects of a variety of different grids, turbulence models, and boundary conditions.

CHAPTER 2

Jet-In-Cross-Flow Experimental Hardware

2.1 Wind Tunnel Description

The present experimental investigation was conducted in the NASA/Ames Research Center subsonic 7x10 foot Wind Tunnel No. 1. Figure 2.1 depicts the general layout of the tunnel. The tunnel is a closed-return type and is of rectangular cross-section, except for the power section. The tunnel has a relatively high freestream turbulence intensity, and is used for general aerodynamic research at velocities up to about 200 knots.

The test section, control room, and assembly bay are contained in a sealed three-story pressure structure that is maintained at test section static pressure during tunnel operation. The pressure structure is sized to allow access to the test section from above, below, and each side. There is no provision for suction or blowing of the test section walls. The test section roof and side walls contain windows of approximately 6 x 4 foot dimensions. In the floor of the test section is an eight foot diameter rotatable turntable attached to integral balance scales located beneath the test section. The turntable remained fixed for this test and the balance was not used.

The power section is located near the end of the diffuser length and is faired to a circular cross-section. The power section contains a single controllable pitch electrically powered fan. The tunnel is cooled and vented aft of the power section by a system of controllable air exchange louvers. The tunnel settling chamber prior to the contraction section is not equipped with either turbulence screens or honeycomb.

2.2 Wind Tunnel Instrumentation

The wind tunnel is equipped with a permanently installed data acquisition system. The system includes a VAX computer, data interface and calibration units, data acquisition software, and instrumentation required to determine tunnel air state and flow conditions. This system is referred to as the Standard Wind Tunnel System (SWTS). In addition, the controls and monitoring instrumentation for tunnel velocity, air exchange, turntable, model balance system, and high pressure air supply are located in the tunnel control room.

The test section freestream conditions were determined by the permanently installed instrumentation linked to the SWTS. The reference for test section static pressure was the permanently installed static port ring located aft of the wind tunnel nozzle contraction at the beginning of the test section. The static ring ports consists of a linked array of 6 ports, with 3 ports on each tunnel wall. A total temperature thermocouple is located in the test section. Prevailing atmospheric pressure, temperature and humidity are measured by a barograph, thermocouple, and relative humidity gage. The SWTS software computes the test section freestream density and dynamic pressure. This values are corrected using calibration polynomials developed for this wind tunnel system.

2.3 Model Description

The model geometry, depicted in Figure 2.2, consisted of a rectangular groundplane with a jet blowing perpendicularly from the upper surface at the one-third chord position. The ground plane was supported 2.58 ft above the tunnel floor on 4 tubular steel legs of streamline cross section.

The groundplane consisted of a 0.083 ft. thick sandwich plate of aluminum face sheets bonded to a plywood core. A 0.167 ft. wide leading edge strip was constructed of fiberglass covered wood and was faired smoothly into the plate. The trailing edge strip was of the same construction as the leading edge and was 0.5 ft. wide. The left and right

groundplane tips were formed of semi-circular section wood. The total groundplane chord was 4.5 ft. and the total span was 4 ft.

The jet exit at the groundplane surface was sharp cornered, perpendicular to the surface, and was 0.167 ft. in diameter. The jet exit was at the center of the groundplane span, and was located at the one-third chord location, 1.5 ft. aft of the leading edge of the groundplane.

For the LDV measurements only a rectangular glass mirror plate with a circular cutout for the jet exit was mounted on the ground plane. The plate was 2 feet long by 1.5 feet wide, and was 1/8 inch thick. The purpose of the plate was to allow LDV measurements to be taken near the surface of the model without capturing intense glare from diffuse reflection of the laser beams from the matte surface of the aluminum groundplane. The mirror surface allowed the path of the reflected vertical beam pair to be controlled to minimize stray light entering the receiving telescope.

The nozzle and plenum supplying high velocity air flow to the jet were mounted underneath the groundplane and extend beneath the tunnel floor through removable access plates in the turntable. That portion of the nozzle and plenum above the tunnel floor were contained in an aluminum fairing which was 1.1 ft. thick, and which extended from 0.5 ft. aft of the leading edge to the trailing edge of the groundplane. The groundplane as a unit was aligned with the test section centerline and was parallel to the tunnel floor.

2.4 Jet and Air Supply Description

The jet exit was contained in a plate that was machined from carbon steel and contained an integral 0.167 ft. long straight cylindrical nozzle extension. The exit plate had a diameter of 0.71 ft. and was mounted flush with the groundplane surface. The nozzle extension was clamped to the discharge end of the nozzle, and was of the same diameter as the nozzle end. The aluminum nozzle was 0.75 ft. long and had a 14.5:1 convergent contraction which faired smoothly into the nozzle extension.

The cylindrical carbon steel plenum chamber was 1.83 ft. long and of 0.635 ft. inside diameter. Figure 2.3 shows the plenum structure to scale. The plenum chamber was of the same diameter as the nozzle entrance.

The flow in the plenum was conditioned by a graded series of perforated plates and turbulence screens to produce a uniform exit pressure profile. The perforated inlet pipe and two perforated plates were sized to create a substantial pressure drop between each stage. The turbulence screens were of 20 mesh and 50 mesh. The final screen was 4 inches from the nozzle entrance. The plenum chamber was designed and certified to American Society of Mechanical Engineers/American National Standard code as a pressure vessel, and was hydrotested to 250 psi.

The wind tunnel high pressure air supply is from a large 3000 psi storage tank located outside the tunnel which is in turn trickle charged from the main Ames Research Center high pressure air facility. The air can be heated using a electrical heater system located in an adjacent building prior to entry into the tunnel pressure structure. After entry into the tunnel structure, a primary pressure reducing valve regulates pressure as needed for test specific hardware. The supply then is passed by means of flexible hoses to a distribution manifold located on the turntable structure under the test section. For this test, the primary reducing valve limited the supply pressure to 500 psi.

The air supply control hardware for the present investigation was located on the ground floor of the tunnel pressure structure beneath the test section. This hardware included a secondary reducing valve to permit more precise control of jet mass flow rate. The secondary supply pressure was limited to a maximum of 125 psi. Each section of the air supply was protected by an appropriately rated burst disk to prevent overpressure. Both pressure reducers and the heater were controllable from the wind tunnel control room.

Downstream from the secondary pressure reducer was an orifice plate flow meter which was used as a qualitative check on jet dynamic pressure calculations. A pair of "T" junctions and a bypass valve downstream of the flow meter permitted a small portion of the

supply air to be passed through a "seeder" vessel prior to entering the plenum chamber during LDV operation. A low resistance ball valve located in the main supply pipe between the "T" junctions allowed the pressure drop across the seeder vessel to be controlled. Where possible, the supply piping was sized in relation to anticipated maximum mass flow and estimated local air density to limit pipe flow Mach number to about 0.4.

2.5 Jet Instrumentation

The jet exit conditions were determined by means of a thermocouple and a static pressure port located in the plenum chamber immediately upstream of the jet nozzle contraction. Due to the nozzle contraction ratio of 14.5:1 and the density change across the nozzle, the plenum chamber velocity was estimated to be only approximately 47 fps at a value of Mj of 0.91, the highest jet exit Mach number used in the investigation. At this low plenum velocity, the plenum temperature and static pressure measurements accurately represented the total pressure and stagnation temperature. The isentopic expansion relationships [15] were incorporated into the data acquisition software to compute jet exit velocity, density, dynamic pressure and Mach number. The calculated values were displayed in the control room on a real time basis.

In a previous investigation by Fearn and Weston [12] using a geometrically similar JICF model the jet exit velocity profile was determined by dynamic pressure measurements. It was shown that the actual jet exit velocity is quite accurately predicted by the assumption of ideal isentropic expansion across the nozzle. The velocity profile was shown to be quite flat, except for a thin nozzle boundary layer.

The model was not equipped with a static pressure port at the jet exit plane. The nozzle pressure ratio used to calculate jet exit conditions was the ratio of plenum chamber total pressure to the freestream static pressure measured at the entrance to the test section. Although the jet exit plane static pressure is not identical to the test section freestream static pressure, it is believed that this uncertainty is acceptable. The values of the jet exit

conditions based on isentropic assumptions were confirmed qualitatively by the mass flow measurements from the high pressure air system. The JICF model used in the present investigation was used in previous investigations [3, 13, 18]. In these investigations the test section freestream static pressure was used to determine the effective velocity ratio from isentropic expansion relationships.

The air supply hardware included static pressure transducer upstream and another pressure transducer and a thermocouple downstream of the orifice plate. Another pressure transducer was mounted on the flow meter case and referenced both upstream and downstream to obtain a more sensitive measure of the pressure difference across the orifice plate. The controls for the stepper motor actuating the secondary pressure regulator were also located in the control room.

CHAPTER 3

Surface Pressure Investigation

3.1 Description of Groundplane Instrumentation

The general groundplane geometry is described in Section 2.2. The surface pressure measurements were made using a radial array of 400 pressure ports, each with a diameter of 0.5mm. The array was divided along the line of symmetry of the groundplane. The left side was a dense array containing 330 ports along 15 radial lines, and the right side was a sparce array containing 70 ports along 6 radial lines. The radial port spacing was also varied with the closest spacing near the jet exit where larger gradients were expected. The port spacing is shown in tabular form in Table 3.1.

The pressure ports were connected by vinyl tubes to a total of 14 transducer modules calibrated to 10 and 20 inches of water. The modules were referenced to the test section static pressure ring. Pressure data from Reference 9 was used to assure that ports were assigned to modules with a reasonable range of calibration and sensitivity. The 20 inch H_2O modules were placed near the jet exit where higher pressure differentials were expected Individual transducers calibrated to 2.5 psi were assigned to 6 ports at a radial position of 0.58 jet diameters, in the 75° to 105° and -60° to -120° angular positions, where the peak suction pressure was expected to exceed 20 inches of water (0.72 psi). Table 3.1 shows the transducer assignments for each port.

3.2 Measurement Methodology:

General. The measurements of groundplane surface pressures was made over a range of jet Mach numbers and effective velocity ratios. The range of jet Mach numbers was selected was selected to determine the effect of Mach number on surface pressure and to allow comparison with previous experimental results. The range of effective velocity ratios was selected to represent the changing velocity of a VSTOL aircraft in transition between hover and wing borne flight, and to allow comparison with previous experiments. Transition in jet-borne VSTOL aircraft such as the Harrier occurs at values of R of about 3.5 and below. This is the range selected for the present investigation. VSTOL aircraft utilizing low pressure ration lift fans may begin transition at values of R of about 2.

The effective velocity ratio is defined as the square root of the ratio of the jet dynamic pressure to the dynamic pressure of the undisturbed freestream. This definition scales the effects of density variations between the freestream and the jet efflux. Although the high pressure air supply included a heater of sufficient capacity to maintain jet exit temperature at near freestream levels, the large thermal inertia of the supply/heater system and the varying degree of isentropic expansion over the Mach range made precise control of jet exit temperature unfeasible. In general, the jet exit temperature was substantially below freestream temperature.

Test Conditions. The matrix of test conditions included Mach numbers of 0.50, 0.74 and 0.91 and effective velocity ratios of 4, 6, 8, and 12. The combination of Mach number 0.94 with a effective velocity ratio of 4 would have resulted in an expected peak pressures exceeding the calibration range of many on the the groundplane pressure transducers, and was not tested. The remaining 11 matrix combinations were tested.

The freestream dynamic pressures ranged from 2.71 psf to 54.26 psf, corresponding to a velocity range from 47.7 fps to 217.1 fps. To assure a consistently turbulent groundplane boundary layer, an abrasive grit trip strip was used near the leading edge.

In practice, the tunnel velocity control was far more precise and repeatable than the control of the jet velocity by means of the supply air pressure regulator. For this reason the test sequence was planned to test at a fixed jet Mach number through the full range of tunnel velocities before adjusting to a new Mach number.

During the course of a test run, the high pressure air supply storage tank pressure gradually decreased. Due to the limiting precision of the pressure regulator, small variations (1 to 2%) in the measured jet Mach number and the resulting effective velocity ratio occurred between measurements at a given target jet Mach number.

In addition to the test measurement matrix described above, measurements without jet flow were made. Due to blockage effects of the model supports and nozzle fairing, a small induced upwash was expected to create a chordwise pressure gradient over the groundplane in the "jet-off" condition. These measurements were used to distinguish the effect of jet interaction from the effect of model blockage and alignment.

The term "induced pressure" will be used to refer to the net change in pressure between the jet-on and jet-off condition. Even though the comparison was to be made using normalized pressure coefficients, the jet-off measurements included the full range of freestream dynamic pressures used in the jet-on measurements. This allowed the comparison for each data point to be made with a jet-off measurement taken at like freestream dynamic pressure in order to minimize scale effects on pressure transducer sensitivity and groundplane boundary layer thickness.

Data Acquisition. Data was acquired using the permanently installed data acquisition system (SWTS) in conjunction with the PSI 8400 integrated calibration and data acquisition system, which was used to take data from the groundplane pressure transducer modules. The Appendix contains the specifications of this system and its performance. The system returned the pressure difference in pounds per square inch, time averaged over a period of 20 seconds. This data was recorded by the SWTS.

Due to system limitations, the data for tunnel and jet conditions as well as the 6 individual groundplane transducers could not be acquired at the same time as the groundplane pressure data. Therefore this data was acquired immediately following the groundplane pressure data, and was also time averaged over 20 seconds.

The reference pressure for the groundplane pressure transducer modules and individual transducers was the permanently installed test section static port ring described in Chapter 2. Thus the measured pressure represented the difference between freestream and local static pressures. The test section freestream conditions were determined by the permanently installed instrumentation linked to the SWTS. The jet exit conditions were determined by means of a thermocouple and static pressure port located in the plenum chamber, as described in Chapter 2.

3.3 Data Reduction

The data for each run sequence was initially stored by the data acquisition software in ASCII text data files on disk drives of the SWTS. For the PSI data, this included only the reduced values of pressure for each port, since the PSI 8400 system does not retain raw transducer voltage data. For all other data acquired by the SWTS the files included both reduced values and raw voltage measurements, calibration coefficients and tare voltages. The data files were later transferred to a MICROVAX computer system dedicated for research use in the Full Scale Aerodynamics Division of Ames Research Center. The data files were then available by network for further reduction and display using the VAX system, Iris work stations, and Macintosh personal computers.

The data was subsequently further reduced using FORTRAN programs to compute net induced pressure coefficients and to prepare input files for graphic display using Plot3D and Kaleidagraph programs.

3.4 Results and Discussion

Pressure Data. Figures 3.1 to 3.4 are contour plots of the jet induced pressure coefficient for values of R from 4 to 12 over a half-plane. The freestream dynamic pressure is the normalizing parameter. In each of these plots, the freestream is indicated by arrows, the leading edge of the jet is located at the zero degree azimuth. These plots are of the data for the highest available Mach number (generally 0.91) for each value of the effective velocity ratio, as the effect of Mach number will be discussed separately. The data used are listed in tabular form in Tables 3.2 to 3.12. The locations of the pressure ports are indicated as dots, and the jet exit lip is outlined as a solid line.

Figures 3.5 to 3.8 are plots of the jet induced pressure coefficient plotted along radial rays for angles from 0 to 180 degrees, and for values of R from 4 to 12, at the same Mach numbers as used in the contour plots. The radial location of the jet lip is shown as a vertical dashed line in each plot.

General Pattern. The contour plots show the general pattern of a relatively small quasi-stagnation region at the leading edge of the jet, in which positive pressures prevail. The radial plots show that the C_p value does not approach unity. Due to jet entrainment, the maximum values are about 0.5.

At the side of the jet there is a region of intense suction due to the high speed flow in this region and the entrainment of the flow by the jet. The radial plots show that the values of C_p may be less than -4 near the jet exit. The negative values of C_p smoothly approach zero at increasing distance from the jet.

At the trailing edge of the jet the suction becomes less intense, but remains substantial. The radial plots show a reflex in the pressure gradient at distances of less than one jet diameter, for angles greater than 150 degrees.

Effect of Effective Velocity Ratio. The most dramatic parameter influencing the induced pressure distribution is the effective velocity ratio. Figure 3.9 shows comparison

contours of C_p values of 0, -0.25 and -1.0, for values of R from 4 to 12. The contours are presented in two plots for clarity.

The contours of $C_p = 0$ shows that the region of positive pressure coefficient dramatically contracts as effective velocity ratio increases. The largest change is between values of R of 4 and 6. As the value of R exceeds 4, the region of positive pressure becomes bounded by a closed curve near the leading edge, with negative pressures propagating ahead of the jet at distances of greater than about 1.5 D. This effect appears to be due to the increased magnitude of entrainment of flow by the jet.

The contours of $C_p = -0.25$ shows the shape of the far-field suction region. Due to the relatively large area, this accounts for much of the thrust loss of the jet. As R increases, the area within the contour increased, and moves forward. The greatest change is again between values of R of 4 to 6, with the extended "tail" of the suction region at the trailing edge disappearing as R exceeds 4.

The contours of $C_p = -1.0$ shows the shape of the near-field suction region. The trend is similar to that of the contour of $C_p = -0.25$. However, it is noteworthy that the area under the contour reaches a maximum at R = 6. The radial plots of Figures 3.5 to 3.8 show that the most intense suction also occurs at this value of effective velocity ratio.

Effect of Jet Mach Number. The effect of jet Mach number can be seen to be a secondary influence on pressure distribution. It should be noted that, since the geometry is fixed, increase in Mach number is accompanied by an increase in Reynolds number. Figures 3.10 to 3.13 compare the effect of jet Mach number for values of R from 4 to 12, and for value of M_j of 0.50, 0.74, and 0.91 (no data was taken at R = 4 and $M_j = 0.91$ due to transducer scale limits).

Figure 3.10 shows that the effect is uniformly small at R = 4. As R increases, the effect of Mach number appears to increase, but is limited chiefly to specific areas of the pressure signature. The greatest effect appears to be in the wake region, at angles

exceeding 135 degrees. There is also a region at the front of the far-field suction lobe which shows Mach number effect. The overall effect is to move the suction region rearward as Mach number increases.

The comparison of groundplane surface pressure distributions at differing jet exit Mach numbers necessarily is affected by the various sources of measurement uncertainty. Thus the variation in C_p contour location with respect to M_j is in part due to the uncertainty in the measurement of effective velocity ratio, as discussed in Section 2.5, and the effect of transducer scale and sensitivity, as discussed at the conclusion of this section. However, these influences do not affect comparisons made of the relative magnitude of variation on different regions on the pressure footprint.

Comparison with Other Work. Figures 3.14 to 3.16 are contour plots comparing the experimental data with data obtained from Reference 9, for values of R of 4, 6, and 8. The reference data are from a geometrically similar model with D = 4 inches, at a Mach number of 0.93. In general, the experimental data is in good agreement with the reference data. Some of the deviations of the reference data may be due to round-off limits in the tabular data used to produce the plots. There are no apparent differences in the contours of a magnitude greater than the uncertainty of the data.

Figure 3.17 shows a comparison with CFD solutions obtained from related work done a NASA/Ames by Chiu, et al. [14] with the experimental measurements in the present investigation. The plots compare the radial C_p distribution for the 0°, 90°, and 180° azimuths. The experimental measurements are at R = 6 and M_j = 0.74. The CFD solutions plotted were done with version 1.6q of the OVERFLOW code at values of R = 6 and M_j = 0.78. The computational upper boundary was at z/D = 20 and the lateral boundary was at y/D = 10. The boundary conditions were of the extrapolated outflow type.

The study in Reference 14 found that the CFD solutions of groundplane surface pressure were sensitive to the grid geometry in the shear region, the type of boundary

conditions, the turbulence model used, and the version of the code used. No single combination of these parameters was found to be superior to all others in comparison with experiment in all regions of the surface pressure signature.

The first CFD solution plotted corresponds to the grid 3 solution shown in Figure 14 of Reference 14, and was computed using the Baldwin-Lomax turbulence model for 11,150 iterations. Grid 3 used an intermediate grid density in the jet lip region. The second CFD solution corresponds to the Baldwin-Barth solution shown in Figure 15 of Reference 14, and was computed using the finer grid 2 for 11,000 iterations.

At the 0° azimuth, Figure 3.17 shows both CFD solutions to be generally close to the experimental values, although the Baldwin-Barth solution is not quite asymptotic to zero as radius becomes large. The value of C_p as the jet exit lip is approached is also higher for the CFD solutions than the experimental value, and exceeds the physical limit of unity at the jet lip is reached.

At the 90° azimuth, Figure 3.17 again shows both CFD solutions to be generally quite close to the experimental values, and the comparison remains close as the jet lip is approached. Although the Baldwin-Barth solution is slightly closer to the measured values near the jet, the Baldwin-Lomax solution is closer as the radius becomes large.

At the 180° azimuth, Figure 3.17 shows that both CFD solutions to diverge substantially from the experimental values. It is not surprizing that the correlation of the CFD solutions with experiment is more limited in this region of separated wake flow than in the other quadrants. The Baldwin-Lomax solution bears little resemblance to the experimental values and remains very near a zero C_p value.except at the jet lip. The Baldwin-Barth solution curve has generally the same shape as the curve of experimental values, but shows a consistent positive pressure offset in comparison to experiment.

Comparison with Solid Cylinder Models. Figure 3.18 plots the angular distribution of pressure of the innermost circular row of pressure ports (r/D = 0.58) for values of R

from 4 to 12 against the inviscid theoretical results for the surface pressure of a two dimensional solid cylinder, from Reference 17. The static pressure at the innermost row of pressure ports is intended to represent, by analogy, the surface pressure of the roughly cylindrical jet flow structure near the jet exit.

The purpose of this comparison is to gain a qualitative understanding of the relative effect of jet entrainment and flow deflection in producing the observed pressure signature. It should be noted, of course, that the analogy of the three dimensional jet to a two dimensional solid cylinder is only an approximation of the flow physics, since the JICF interaction of free shear layers and the groundplane boundary layer is a flowfield which is qualitatively different from boundary layer flow about a 2-D solid cylindrical body.

Figure 3.18 shows that the general shape of the inviscid model is best approximated at the highest value of R = 12, although the C_p values are consistently more negative.

Figure 3.19 compares the experimental jet induced pressures for values of R of 4 and 12 with experimental solid cylinder data from Reference 17. The cylinder data are shown at both a subcritical Reynolds number ($Re_D = 1.9 \times 10^5$) and a supercritical Reynolds number ($Re_D = 6.7 \times 10^5$). It can be seen that the shape of the plot of the data for R = 12 roughly approximates the shape of the supercritical experimental solid cylinder data.

Figures 3.20 and 3.21 are plots showing the magnitude of the pressure difference between the experimental jet data and supercritical reference data depicted in Figure 3.19. For this purpose, the term "local difference" means the difference in C_p value, at a particular angular measurement location, between the JICF and the cylinder data (displayed as an interpolated curve). The term "mean difference" refers to a least squares curve fit to the local difference values at the various measurement locations. Since the data is reflected about the symmetry plane for display purposes, the mean difference curve is horizontal.

It can be seen from Figure 3.20 that for R = 12 the departure of the local difference curve from the mean difference is generally quite small. This shows that at this relatively

high value of R, the difference in C_p magnitude between the JICF and the solid cylinder is remarkably constant with respect to angular position. However, Figure 3.21 shows much less constancy at R = 6.

It appears that at the higher value of R the surface pressure distribution near the jet lip can be qualitatively viewed as a superposition of the effect of velocity changes due to flow blockage by the jet shape and acceleration by flow entrainment in the shear layer at the jet boundary. This comparison becomes progressively weaker as R decreases.

Symmetry Plane Comparison. In order to assure that the flow about the model was symmetrical, the sparse field data from the left side was compared with the denser data from the comparable angular position on the right side. Figures 3.22 to 3.25 show this comparison for values of R from 4 to 12, for angles of ±10°, ±60°, ±120°, and ±170°. The comparison is quite close throughout this range of velocity ratios and angles, and there are no regions of significant discrepancy. It is therefore concluded that the flowfield about the model, at least as it affects surface pressure, is symmetrical on a time-averaged basis.

Experimental Uncertainty and Interference Effects. The specified accuracy of the PSI 8400 transducer system is 0.1% of the full transducer scale. The system specification and description is contained in Appendix B. The predicted magnitude of uncertainty of the normalized pressure coefficient measurement depends on the transducer module used, as well as the magnitude of the freestream dynamic pressure used to normalize the pressures.

Table 3.13 shows the calculated uncertainty in C_p for each combination of R and M_j (and thus each value of q_∞ used). For a given level of coefficient, the actual pressure measured was lowest at minimum jet Mach number and maximum effective velocity ratio. The greatest uncertainty thus is at R = 12 and M_j = 0.50. For this reason, the most accurate data for each value of R is from the highest jet Mach number used.

Examination of radial raw data plots showed that there was a small but abrupt discontinuity at r / D = 2.0, at the junction between the 20 inch H_2O modules and the 10

inch H_2O modules. This discontinuity is consistent with the differing transducer scales and specifications. The effect of uncertainty is most visible in the low gradient areas of the pressure signature at a distance from the jet. Figure 3.26 show an example plot of contours with an uncertainty band width of $\pm$ 0.003 C_p, a typical value at the higher Mach number measurements.

An additional source of uncertainty is due to flow blockage and interference by the model supports and plenum chamber fairing. The fairing had a cross-sectional area of 2.7 ft^2, constituting 3.9% of the test section area. The pressure measurements made with jet off on the 0° and 180° azimuths show a slight longitudinal gradient of pressure, indicating a small negative pressure peak at the groundplane leading edge. The blockage effect of the plenum chamber fairing under the groundplane was expected to cause a slight upwash at the leading edge of the groundplane. This effect was expected to be greatest near the plane of symmetry, and to decrease as the distance above the groundplane increased. At the port nearest the leading edge, at the 11% groundplane chord the C_p value was -0.275. The suction C_p decreased to -0.13 at one jet diameter from the jet centerline, equivalent to the 30% chord position. The C_p measured aft of the jet was essentially constant at -0.125 out to the aftmost port location at the 55% chord location. These negative values of the pressure coefficient indicate that the velocity near the groundplane surface in the jet exit region was increased by blockage effects to slightly above V_∞.

Since the tare Cp values are deducted from the jet-on Cp measurements to determine the induced pressure coefficient, the interference effects are not believed to effect the accuracy the surface pressure data. In addition, since the interference effects appear to decrease rapidly aft of the groundplane leading edge, it is not believed that there is any significant effect on the jet plume shape or velocity distribution.

CHAPTER 4

Schlieren Photography

4.1 General Principles

Schlieren techniques exploit the deflection of light ray paths through a medium to obtain a visual display of density variations in the medium. The term schlieren stems from the German word *schliere*, which refers to a localized inhomogeneity or striation in a transparent material. Schlieren photography belongs to a class of techniques for visualizing density or refractive index variation in transparent mediums, such as are found in fluid flow and shock wave propagation. Related methods include interferometry and shadowgraph imagery [19].

Schlieren techniques are sensitive to first derivatives of density (actually refractive index) perpendicular to the axis of illumination, and use focal plane blocking effects to discriminate between deflected and undeflected light. Deflection of light in a continuous medium is a function of refractive index gradient. Schlieren techniques are generally used for qualitative imagery, although quantitative measurement is possible [19, 20].

By comparison, interferometry is directly sensitive to variations in density since it exploits the phase shifts induced by light velocity variation in the test region to produce an alteration in a pattern of interference fringes [19, 21]. Interferometry requires precise optics to control both measuring and reference beam alignment and path lengths. It is useful for both quantitative measurement and qualitative visualization.

Shadowgraph systems are sensitive to second derivatives of density perpendicular to the axis of illumination, and exploit differing degrees of deflection produced by changes

in the gradient of density. No focal plane blocking occurs and the collimated beam need not be brought to a focus after passing through the test region. Thus a constant gradient of density (producing constant deflection) results in no concentration or rarefaction of light intensity at the image plane. Shadowgraph systems can use relatively simply optics and are particularly useful in discriminating abrupt changes or discontinuities in density, such as shock features [19].

Principle of System. Figure 4.1 shows a simplified schematic of a typical schlieren system. A light source **A** is focused by lens **B** on a slit $\mathbf{S_1}$ to produce a finite source with respect to the direction perpendicular to the slit. The slit is located at the focal point of a lens **C** which produces a uniform collimated beam, the collimation angle of which is determined by the slit width. The collimated beam is then passed through the test medium or fluid region **D** (it is assumed that there are no density gradients in the beam path outside the test region).

After passing through the test region, the beam is brought to a focus by a second lens **E**. A knife edge $\mathbf{S_2}$ is located at the focal point of the second lens. The knife edge is adjusted so that it covers part or most of the image of the source slit $\mathbf{S_1}$. If the test region contains no density gradient perpendicular to both the light path and slit, the beam will be undeflected, and will be sharply focused by the lens. In this case the slit image will be partially blocked by the knife edge as it passes through the focal point. Due to the finite collimation angle, the unblocked portion of the image will uniformly but dimly illuminate a projection screen or photographic plate **P** located beyond the focal point.

In air, the refractive index is nearly proportional to density. For small angles of deflection, the deflection induced in the path of a light ray during travel through an incremental portion of a flow test region is proportional to the local gradient of refractive index perpendicular to the path. If the test region does contain density gradients perpendicular to both the light path and slit, the portions of the collimated beam passing

through such gradients will be deflected. Depending on the direction of deflection, the deflected rays will either miss the knife edge and create a brighter point on the screen, or the light will be further blocked and create a darker point on the screen. In this manner, an image of the density gradients in the test region will be created.

For a system sensitive to density gradients in any direction perpendicular to light path, the source slit S_1 may be replaced by a pinhole and the knife edge S_2 may be replaced by another pinhole. In this case the undeflected beam will uniformly illuminate the screen, and any deflection will create dark points on the screen.

Since the collimated beam is incrementally deflected by localized density gradients as it travels through increments of the test region, the total deflection is the integral of the such localized deflections over the path through the test region. Therefore a conventional schlieren system does not resolve structures on the axis of illumination. Various schemes do exist for obtaining focused schlieren images which can resolve a relatively thin plane within the test region, but these will not be discussed here [see reference 22].

For schlieren systems designed for large fields of view, such as in wind tunnels, the use of focusing mirrors rather than lenses is advantageous, as large mirrors are cheaper and easier to produce than large lenses. In this type of system the light source and imaging optics may be located at small angles off axis to the collimated beam path. To keep the optical path simple, it is desirable that the distance of each mirror from the measuring region be greater than the focal length of the mirror. The system used in this experiment is of this type.

4.2 Description of System

Figure 4.2 shows the system used in this experiment. The system was designed specifically for the 7x10 ft wind tunnel, and is designed to have a relatively large field of view. When in use, the system is mounted as four distinct portable units located on the floor area on both sides of the test section. The test section wall windows are used to

transmit the collimated beam. The beam path is limited to a roughly horizontal plane, but can be adapted to experimental requirements by choice of position and height of the mirror stands and the imaging optics tripod. The knife edge and slit may be oriented in any direction.

The beam is collimated and focused by two identical 17.5 inch astronomical telescope mirrors of 78.75 inch focal length mounted on separate stands on each side of the test section. The mirrors are mounted on gimballed stands of adjustable height. The mirrors are fitted with hinged covers to protect them between test runs.

The light source is mounted on a separate tripod with an optics mounting rail. A Stobex model 236 adjustable trigger stroboscope emits light through an rectangular aperture window approximately 1/2 by 2 inches in size. The light is focused by a simple magnifying lens on a slit composed of two razor blades in an adjustable mounting. The slit width was about 0.05 inch. A slide projector lens set was inserted in the optical path near the slit to allow vernier adjustment of focal length without moving either the light source tripod or mirror stand.

Due to space limitations, the light source could not be directly aligned with the collimating mirror, and an adjustable plane mirror is used to direct the divergent light from the slit to the mirror. The stroboscope power supply can be triggered by a remote switch which is located on the opposite side of the test section near the imaging optics.

The imaging optics are also mounted on a separate tripod with an optics mounting rail. The rail contains a vernier traverse mounting for a razor blade knife edge at the focal point of the mirror, and a polaroid film pack camera. For adjustment purposes, the camera has a ground glass image screen which is viewable when the film pack is removed.

4.3 Experimental Procedure

The rough adjustments were made to the various components by positioning mirrors stands and optics tripods on the assembly area floor according to the known focal

length of the mirrors, and by adjusting the heights of the stands to give a beam height appropriate to the model dimensions. The field of view was targeted to put the jet exit in the lower upstream corner of the field to allow as much of the jet plume to be displayed as possible.

The stroboscope trigger was set to give a continuous short period sequence flashes to provide a quasi-continuous light source for adjustment purposes. Preliminary adjustments were made to the light source optical components to yield a divergent beam just covering the face of the collimating mirror. The room was partially darkened, and a paper screen was taped over the focusing mirror to allow the rather dim collimated beam to be aimed through the test section to fall on the center of the focusing mirror. The slide projector lens on the light source optical rail was then adjusted until the beam coverage on both mirrors was equal within about 1 to 2 inches. Since the mirrors were located 38 feet apart, the beam was thus parallel to within about 0.25 degrees.

The focal plane of the collimating mirror was adjusted using the slide projector lens set until the the slit was at the focal plane (the slit was in a horizontal position). The paper screen was removed from the focusing mirror, and the imaging optic rail and camera location adjusted until the image of the slit was focused on the ground glass screen of the camera with the uniform intensity view field just covering the 4 x 5 inch camera screen. The knife edge was then adjusted longitudinally to the focal plane of the focusing mirror, and adjusted vertically until the field was partially dimmed by blockage.

To check the location of the jet in the image, and to provide a magnification scale, a 2 x 12 inch transparent grided ruler was mounted in the jet exit, and a test photograph was taken.

During photography of tunnel and jet flow, the stroboscope was set to manually triggered single flash operation. ASA 1000 film was used. The room was darkened as much as possible to minimize stray light. The knife edge position and camera focus were checked by viewing the camera screen just before insertion of the loaded film pack to make

certain a clear image of the jet plume was being obtained. Rapid manual triggering of the strobe gave a sufficiently continuous image for this final check. After insertion of the film pack, the camera shutter was opened and closed manually immediately before and after the manual strobe trigger was depressed.

4.4 Test Conditions

At each flow condition used for schlieren photography, a measurement of tunnel and jet flow data was made using the SWTS data acquisition system, the same instrumentation used to record tunnel and jet flow during laser Doppler velocimetry and pressure measurements. This system and instrumentation are described in Section 2.

In general, at least two photographs were made at each condition. Each polaroid photograph was examined and labeled immediately after taking the photograph. Due to the sensitivity of the imaging optics to the high vibration level from tunnel operation and manual operation of the camera shutter, the degree of light blockage by the knife edge was not consistent from shot to shot. When a photograph showed reduced contrast from too little or too much blockage, the photograph was repeated. Tunnel conditions were changed after at least one reasonable quality exposure was obtained.

The primary series of schlieren photographs were taken over the same range of jet/tunnel velocity ratios used for the LDV and surface pressure measurements in this experiment. The purpose was to provide a visual record of the subsonic jet plume structure as a function of effective velocity ratio. No attempt was made to visualize the effect of variation of jet Mach number.

All photographs in the primary series were made at a jet Mach number of 0.94. This was the highest Mach number used in surface pressure measurements, and was selected to maximize density gradients in the jet plume, without causing localized shock structures near the jet exit. The initial photograph was made with the tunnel flow stopped

to visualize the free jet. The tunnel velocity was progressively increased at constant jet Mach number through a range of effective velocity ratios from 12.8 to 4.7.

A second series of schlieren photographs was taken without tunnel flow at nozzle pressure ratios slightly less then and slightly greater than required for choked flow. The test conditions were chosen to demonstrate jet exit shock structures. The values of pressure ratio tested were 1.75 and 1.98, corresponding to calculated Mach numbers of 0.93 and 1.04 respectively.

4.5 Results and Discussion

Figure 4.3 shows a schlieren photograph of the jet plume at R = 4.65, with M_j = 0.95. The leading edge of the jet can be seen to develop roll-like structures similar to the ring vortices present in the turbulent mixing of free jets. These structures decay rapidly. The plume can be seen to become very broad within a few jet diameters as the vortex pair propagates below the jet centerline.

Figure 4.4 shows a schlieren photograph of the jet plume at R = 6.49, with M_j = 0.94. The development of the lateral shear layers, rolling away from the jet centerline can be seen more clearly than in Figure 4.3. In addition, distinct wave-like structures can be seen separating from jet plume in the wake region.

Figure 4.5 shows a schlieren photograph of the jet plume at R = 12.82 with M_j = 0.93. The ring vortex-like system is quite distinct compared with previous figures. The plume vortex pair develops more slowly as the jet core momentum is maintained for a greater distance.

Figure 4.6 shows a schlieren photograph of the undeflected jet without crossflow with M_j = 0.94. Although the photograph contrast is not strong, it can be seen that the jet develops an organized pattern of ring vortices within 2 or 3 jet diameters. The jet potential core decays rapidly. The vortices propagate upwards as large scale turbulence structures involving the entire jet width.

CHAPTER 5

Laser Doppler Velocimetry

5.1 General Description of LDV system

The orthogonal 3-dimensional real fringe fixed-focus laser Doppler velocimeter (LDV) system used has been under development by the Full Scale Aerodynamics Division of Ames Research Center since 1989 as a permanently mounted system for the 7x10 foot wind tunnel. In an orthogonal LDV system the illuminating beam pairs are aligned at 90° angles to one another. The focal point location of each beam pair is changed by moving the entire optical system on a 3-dimensional traversing mechanism, rather than by use of zoom lens mechanisms to change the focal length of the optics. The system uses independent optics for transmission and signal receiving, and can be adapted to use either backward scattering or forward scattering when the optical path is clear. The system is based on a single 4 watt argon ion laser, which is separated into as many as four beam pairs

The system uses Macrodyne time domain burst counter-processors to determine the Doppler frequency, and uses a Macrodyne LVABI autocorrelating data buffer to acquire and validate processor data prior to transmission to a PC/386 computer.

The LDV system may also be converted for laser sheet illumination of the test section for flow visualization. For this purpose a cylindrical lens is substituted which spreads the beam into a two dimensional sheet, illuminating either from above or from the side of the test section.

5.2 General LDV Principles

Reference Beam Systems. The earliest LDV systems were of the reference beam or heterodyne type. Figure 5.1 shows schematically a reference beam system. In a reference beam system a coherent laser beam is split into two beams, one of which is an illuminating beam focused on the measurement point, and one of which is a reference beam. Light scattered by particles suspended in fluid moving through the measurement point undergoes a true Doppler frequency shift [23, 24].

In a high density fluid such as water, the density of naturally occurring particulates is often sufficient to provide an adequate signal. However, in wind tunnel measurements it is generally necessary to provide a seeding of dispersed particles. In order to avoid inertial particle lag in accelerating or turbulent flow [25] and to improve scattering efficiency, the particles should generally be of a size comparable to the wavelength of the laser output.

In a reference beam system, the scattered light from the measurement point is detected by receiving optics located out of the line of the illuminating beam. The Doppler shift is proportional to the component of particle velocity along a line bisecting the angle between the transmitted beam and the scattered light received. The scattered light is then mixed with the reference beam. Interference between the shifted and unshifted beams results in a beat frequency which is equal to the frequency difference, and which is thus proportional to the velocity component [23].

In spite of their inherent simplicity, reference beam systems have practical limitations. They require very precise beam alignment and path length adjustment, and are consequently sensitive to vibration. In addition the intensity of the reference beam must be adjusted to be of the same order as the shifted beam for reasonable signal strength. The reference beam configuration is most practical in small laboratory systems where all optical components can be mounted on a single rigid optical bench.

Real Fringe Systems. Real fringe LDV systems overcome some of the practical limitations of the reference beam type, and real fringe systems are generally more suited to

wind tunnel applications. The remainder of the discussion will apply to real fringe systems, where a distinction is relevant.

Figure 5.2 schematically depicts a generalized real fringe system. In a real-fringe LDV system the laser beam is split and the two beams are spatially separated. The beam pair is then focused to intersect at a small angle at the measuring point, Generally the same optics are used to focus both beams and the beam separation (and thus convergence angle) is limited by the focusing lens diameter. Figure 5.3 shows a schematic of a back-scatter system where the receiving optics are located in line with the illuminating optics.

Constructive and destructive wave front interference between the intersecting beam pair results in a three dimensional "fringe" structure of illumination in the region in which the beams overlap . This overlap region is referred to as the "measurement volume." The fringes are aligned along the line bisecting the angle of convergence, and are perpendicular to the plane of the converging beams [26, 27]. In an orthogonal 3-D LDV system the three separate component channels form an overlap region in which three distinct mutually perpendicular fringe systems are present. Figure 5.4 shows schematically an orthogonal 3-D measuring volume.

A particle passing through the measurement volume of a real fringe system creates a pulse of scattered light in which the intensity is modulated as the fringes are crossed. Although the frequency of modulation is not the result of a true Doppler shift, it is proportional to the component of velocity normal to the fringe system, and is generally referred to as the "Doppler frequency".

The light scattered from the measurement volume is gathered by receiving optics for signal processing. Note that the Doppler frequency depends only on the fringe geometry and particle motion, and does not depend on receiver location. For this reason, a real fringe system does not require any precise alignment between the illuminating optics and the receiving optics. Thus the system is not sensitive to vibration or distortion of structure

which may change the geometry of the overall system, provided the overlap of the illuminating beams can be maintained [24].

Component Separation. Two components of flow can be conveniently obtained by use of the distinct color lines of the laser output. The strongest lines for the argon ion system are at wavelengths of 514.5 nm, 488.0 nm and 476.5 nm. The laser output is separated using prisms or other separators, and the different colors are focused on the measuring volume as distinct beam pairs. Generally a single set of illuminating optics are used.

If the plane of one such beam pair is rotated 90 degrees by the optics with respect to the other pair, the two fringe patterns in the measuring volume will be perpendicular to each other. Since the two fringe patterns (of different colors) are mutually perpendicular, they will be sensitive to two mutually perpendicular velocity components lying in a plane perpendicular to the axis of illumination. The scattered light signal gathered by the receiving optics can then be separated by color into two channels prior to signal processing.

In order to resolve the third component of motion, a third beam pair must be focused upon the measuring volume, and this pair must have an axis of illumination at a substantial angle to the axis of the other two beam pairs. The third fringe system (or the second, for that matter) need not be perpendicular to the other two, since the orthogonal components can be computed trigonometrically. However, where the angle is small, the precision of measurement of the third component suffers [26, 27]. In an orthogonal 3-D system, the third beam pair is normal to the other two pairs.

The third component may be distinguished by use of a third distinct frequency line. Alternatively, in the case of an orthogonal system, the difference in scattering intensity may be exploited, where separate receiving optics are used for the third channel. For particle size comparable to the wave length of the light, most of the scattering intensity is due to Mie scattering [24]. The most intense scattering is in a forward directed lobe, and a less

intense backscatter lobe. Scattering in the normal direction is weaker than either the forward or backward scattering [23,24]. Thus, where the receiving optics for the third component is located at a normal angle to the illumination axis of the two other pairs, the signals can be distinguished by intensity, if the signal-to-noise ratio of the third component is sufficient.

Velocity Bias. The use of Doppler frequency to determine velocity involves an inherent directional ambiguity, since the frequency proportional to the magnitude of the velocity component, and is insensitive to its sign. In order to distinguish between positive and negative direction of the component, a predetermined frequency bias in one beam of each beam pair is used to ensure that no sign reversal occurs in the measured data. In effect, the frequency offset in the beam pair causes the interference fringes to shift in position in the measuring volume at a fixed rate. This "motion" of the fringe system is detected in the measured data as a constant increase (or constant decrease) in the Doppler frequency. The frequency bias is then deducted to reflect the true velocity.

The most commonly used device to introduce a known frequency shift is the Bragg cell, which uses a radio frequency resonant cavity to alter light frequency. Other devices may be used, such as a rotating defraction grating. The output of the Bragg cell is generally shifted by too great an offset (about 40 MHz) for convenient signal processing. For this reason a signal generator and mixer is used to reduce the effective offset to a convenient magnitude prior to signal processing.

Signal Processing. The scattered light signal gathered by the receiving optics is either filtered (where individual receivers are used) or separated by color (where a combined receiver is used) prior to being fed to photomultipliers and amplifiers to convert the light signal to an electronic signal. Several different signal processing schemes may then be used to determine the Doppler frequency, such as frequency tracking, spectral analysis, and burst detection and counting [28, 29].

The scheme used in this test was time domain burst detection and counting. In this method the input signal-to-noise ratio is improved by high-pass and low-pass filtering of each component channel to eliminate frequencies outside the band of physically realistic Doppler signals. This also eliminates any dc component or "pedestal" to the signal. After filtering, the signal consists of discrete "bursts" of higher amplitude immersed in a continuum of noise. The bursts represent the filtered periodic component of the scattered light from individual particles passing through the measuring volume. Figure 5.5 shows diagramatically the superimposition of pedestal and signal.

The signal for each channel is next digitized by a zero-crossing voltage trigger of adjustable sensitivity threshold. The trigger produces a square wave signal by responding to each positive slope node point of the oscillating signal. To accurately define a Doppler burst, the digitizer trigger sensitivity threshold must be adjusted to be insensitive to the prevailing noise intensity. Thus the signal-to-noise-ratio is a critical limitation on the effectiveness of time domain burst detectors.

The burst counter is reset between bursts and is triggered by the first response of the digitizer. The counter determines the frequency of the burst by measuring the elapsed time for a measured number of oscillations.

Since the signal channels from different beam pairs are processed separately, the burst detectors may not detect a burst simultaneously in each channel. Non-simultaneous response is generally due to particles passing through the fringe systems of some, but not all, the beam pairs. The overlap region of each beam pair in which an individual component fringe system exists is a highly elongated ellipsoidal region. In a precisely aligned orthogonal 3-D LDV system, the region in which all three fringe systems coexist is a much smaller roughly spherical subregion of these individual fringe systems.

Non-simultaneous response of the burst detectors may also be due to differing signal strength and sensitivity in the component channels, or to particles passing parallel to the fringes of one component.

Autocorrelation between channels can be used to reject burst counts where each correlated channel does not detect a burst within a small specified time increment after initial burst triggering. This will assure that the measured Doppler frequencies for each channel represent the velocity components of a single particle. Non-simultaneous bursts do not affect steady state mean flow measurements averaged over a large number of burst counts, but will affect time accurate measurements, such as in the measurement of Reynolds stresses.

5.3 Layout of LDV System

The general layout of the LDV system is shown in Figure 5.6. The laser and all optics are mounted on a rigid aluminum optical frame which is suspended outside the test section over the test section roof on the three-axis traverse system. The entire traverse system and optical system are mounted on a truck which can be moved in the streamwise direction by a worm gear drive. The streamwise truck is supported on rails located on each side of the test section roof.

The laser power supply and the actuators and rails for both spanwise and vertical motion of the optical frame are located on the streamwise truck. Flexible cables, fiberoptics and hoses are connected to the movable truck to control and monitor motion, to supply power and cooling water to the laser, and to return the optical signal for processing.

The spanwise component of velocity is measured by a beam pair transmitted downward from the center of the frame through a window in the roof of the test section. The receiver for this beam pair is a 10 inch Schmidt type reflecting telescope modified to have a focal distance of about 7 feet. The receiver gathers backscattered light, and is mounted near the frame center slightly to the side of the transmitting lens.

The optical frame contains two rigid tubular extension arms descending on each side of the test section. The arms have sufficient clearance from the walls of the test section to permit a spanwise range of motion of the optical frame. The streamwise and vertical

components of velocity are measured by two beam pairs transmitted from a single transmitting lens on the left arm through a window in the left side of the test section.

The common receiver for both horizontal beam pairs is a telescope normally mounted on the right arm. This receiver gathers forwardscatter light through a window in the right side of the test section. The receiver is set slightly off the axis of illumination to avoid capturing the unscattered illumination beams. This receiver can alternatively be mounted on the left side to receive backscattered light if model geometry so requires.

The balance of the LDV hardware is located in cabinets on the assembly area floor to the left side of the test section. This equipment consists of traverse motor controllers, photomultipliers, signal processors, burst counters, data acquisition buffers, and a PC/386 computer for software control and data storage Although there is no direct link from the LDV system to the wind tunnel data system (SWTS), an intercom allows data to be acquired on both systems in a verbally coordinated fashion for subsequent processing.

5.4 Description of LDV optical system

The core of the optical system is a 4-watt Spectra Physics argon-ion laser. Both the laser and its power supply are water cooled. The optical frame provides a rigid foundation for the mounting of the laser, the beam optics, and the various steering mirrors required to control beam paths. Removable cover plates minimize dust contamination of the optics.

Due to potential eye hazards from this class IV laser, access to the test area is restricted during laser operation by several gates armed with safety switches. A guillotine type beam blocker is mounted on the laser to prevent light emission when safety switches are open. A solenoid holds the blocker open against spring tension when the safety switches are closed. The beam blocker also allows the beam to be stopped during adjustment work or between measurements, without having to shut power off to the laser. This is important, since the laser requires a considerable time to stabilize its operating tempurature and output beam characterisics.

The initial laser output beam is composed of a number of distinct frequency components, the three most powerful components being the 514.5 nm, 488 nm and 476.5 nm wavelengths. Only the 514.5 nm and 488 nm components are used in this LDV system. The third channel is distiguished by directional scattering rather than frequency separation, in the manner described in Section 5.3.

The laser output is split by a prism into its component frequencies and all but the 514.5 and 488.0 nm wavelengths are blocked. The 514.5 nm beam is then split by a partially reflective mirror to form an additional 514.5 nm beam. This third beam is the source of the vertical illuminating channel which measures the lateral component of velocity. As currently configured, an additional 488.0 nm beam is not formed, but the system can be used with an additional vertical illumination beam measuring the streamwise velocity component if needed. The remaining 514.5 nm beam and the 488 nm beam are the sources of the two horizontally illuminating channels which measure the streamwise and vertical components of velocity.

Following the initial separation of the beam into three channels, each beam channel passes through a prismatic beam separator which redivides each beam into a parallel pair of beams separated by about 3 inches. The 488 nm beam pair is also rotated 90° out of the plane of the optical frame, so that the two beam pairs of the horizontally illuminating channels lie in planes normal to each other.

One element of each beam pair then passes through a Bragg cell to induce a frequency shift of 40 Mhz in that element with respect to its companion element. This frequency shift provides for the velocity bias in the fringe system which removes the directional ambiguity of the Doppler signal. For adjustment purposes, the Bragg cell can be removed to allow a fixed fringe system to be visualized.

A system of steering mirrors and prisms then guide each beam pair to its focusing lens. The focusing lens of the horizontally illuminating channels is located in the optical frame extension arm on the south side of the test section. The focusing lens of the

vertically illuminating channel is located at the bottom center of the optical frame above the test sevtion. Adjustable wedges and screws in the steering optic supports allow the following adjustments: (a) The focal length of beam pair element can be adjusted so that a minimum beam diameter is obtained at the target measuring point. (b) The direction of transmission of each beam pair element can be adjusted so that the two beams of each pair converge to create an interference fringe pattern at the intended measuring point. (c) The convergence points of the beam pairs from each channel can be shifted to obtain an overlap region of the three fringe systems which constitutes the three dimensional measuring volume. The measurement volume has a diameter of about 300μm (.012 inches).

For adjustment purposes, the fringe systems can be visualized by removing the Bragg cells and placing a microscope objective lens on a stand or tripod in the test section. The measurement volume is brought to the focal point of the lens, and the image of the measurement volume is projected on a screen. When the alignment is correct, the fringe systems are apparent.

To avoid optical changes due to variations in the operating temperature of the laser, the laser is turned on at least 30 minutes prior to any measurement, and is kept on throughout the working day (with beam blocker). However, it is not possible to avoid changes in beam alignment due to local variations in the thickness and refractive index of the window glass. Such variations can cause the alignment to shift from point to point, and thus degrade signal quality.

The two receivers are identical 10 inch Schmidt type astronomical reflecting telescopes which have a modified mounting of the objective lens to permit focus in the near field. One receiver is mounted on the optical frame above the test section, and this receives the backscatter signal from the vertically illuminating channel, which measures the lateral velocity component. The other reveiver is located on the optical frame extension arm on the North side of the test section, and receives the forward-scatter signal from the two horizontally illuminating channels. The telescopes are focused so that the field of view is

limited to an area slightly larger than the measuring volume. In this way, the capture of stray light is minimized and the concentration of scattered light from the measurement volume is maximized.

In operation, the image of the measuring volume is projected onto the terminal fitting of a flexible fiberoptic cable. The cable then carries the optical signal to the photomultiplier housing where the combined signal from the horizontal beam pairs is separated by a dichroic mirror. Each separated signal channel then enters a cascade type photomultiplier tube which converts the optical signal to an electronic signal. The gain in the photomultiplier can be adjusted by controlling the power supply voltage.

5.5 Signal processing and display.

Figure 5.7 diagrams the signal processing and data acquisition system. Prior to processing, the outputs from the photomultipliers are boosted by individual 12 volt amplifiers located in the photomultiplier housing. The signal for each channel is then passed to an individual frequency mixer where it is mixed with a downmix signal generated by a Hewlett-Packard programmable frequency generator. The output from the mixer is a signal representing the difference between the two inputs. The effect of mixing is to reduce the effective frequency bias from 40 MHz (induced by the Bragg cells) to an adjustable known bias value (40 MHz minus generated frequency).

The frequency of this downmix signal is automatically stored as part of the computer generated data file for the measurement point, to be used in data reduction to convert measured frequency to velocity. The frequency generator was manually controlled in this test, but may be directly controlled by the data acquisition software in future.

The downmix frequency at each measurement point is adjusted, based on previous measurements, to yield a mean measured frequency near the center of the high and low pass filter band of the counterprocessor. This allows the pass band to be as narrow as feasible, and thus for signal to noise ratio to be maximized. The bandwidth of the Doppler

signal is due both to the velocity perturbations of turbulence and to signal broadening due to the precision of the signal processing system.

After downmixing, the signal for each channel is passed to an individual Macrodyne counter processor unit. The signal is first filtered by the unit using manually adjustable high and low pass filters. After filtering, the signal consists of discrete "bursts" of higher amplitude immersed in a continuum of noise. The bursts represent the filtered periodic component of the scattered light from individual particles passing through the measuring volume.

For monitoring purposes, the filtered signal from a selected channel may be displayed on an oscilloscope and an analog frequency analyzer. This allows the optics and photomultipliers to be adjusted for maximum signal-to-noise ratio.

The counter processor unit uses an adjustable threshold trigger to detect the onset of a burst and to digitize the signal. The counter then counts the first 8 fringe oscillations of the burst, and computes an oscillation period using the elapsed time for both the first 8 and the first 5 oscillation periods. The two periods are automatically compared by the processor, and the data from the burst is rejected if not consistent within an adjustable tolerance For each channel, the raw output from the counter/processor consists of an elapsed time for the current 8-fringe period measurement, and the inter-burst time since the previous measurement.

The raw data from the counter processor unit are then passed to the programmable autocorrelating data buffer. The autocorrelation function may be selected for any combination of channels. When this function is active, the data from a given channel are rejected if a burst is not detected in each correlated channel within an adjustable time window. For channels for which the autocorrelation function is selected, only data which passes the correlation test are stored in the buffer. The buffer continues to store data until a predetermined number of bursts are received (an adjustable time limit may also be used to terminate the measurement point).

Following data acquisition at each measurement point, the data buffer arrays are read through the interface board by the control software running on the 386 PC. The Doppler frequency for each burst is then calculated, along with the mean frequency and standard deviation of the cumulative bursts at the measurement point. Using the known downmix frequency and calibration values for each channel, the component mean velocity and standard deviation are calculated. The inter-burst time data are stored and may be used to reconstruct a time history of each measurement point, if desired.

5.6 Traverse System and Motion Control

The motion control system is based on stepping motors and controllers capable of programmed angular steps of 1/200 revolution. The optical frame and carriages for horizontal motion are supported on cylindrical steel rails by circular groove wheels. The motion of the optical frame and carriages is accomplished by means of fixed worm gears with recirculating ballbearing gear followers attached to the moving carriage The worm gear pitch is 5 revolutions/inch. Thus the frame motion is 1/1000 inch per step in each horizontal direction.

The rails for streamwise motion are mounted directly on the test section roof structure, while the rails for lateral motion are mounted on the streamwise carriage. Since the weight of the apparatus is normal to these rails, the torque required to move the carriage at modest speed is well within the motor capability.

For vertical motion, the optical frame is supported by a counterweighted steel cable pulley system to relieve the worm gear and follower of the majority of the apparatus weight. The optical frame is directly actuated by the same type of worm gear and gear follower used for horizontal motion, and thus the motion is also 1/1000 inches per step. However, due to the friction of the counterweight system and the residual unbalanced weight, translation speed in the vertical direction is much slower than in the horizontal plane.

The stepping motor angular motion for each translation direction is monitored by an angular encoder mounted on each worm gear axis. The motor controller function can be selected to seek as a goal either a specific position output of the encoder, or a specific position step count of the motor actuator. Since the encoder has a step resolution of only 1/100 revolution compared with the motor actuator resolution of 1/200 revolution, the motor actuator function was generally used for position control in operation. This results in greater precision, provided there is no drive motor stall due to torque overload.

Calibration of the traverse system showed that there is hysteresis in the frame motion of about .005 inches. However, the cyclic repeatability is about ±.001 inch or less. For that reason the experimental control program and procedure was modified so that the traverse approach to both the reference position and each measurement point was from the same direction in each traverse axis. Thus positional hysteresis was not a factor, and the positional repeatability of the measurement volume due to traverse motion is approximately ±.001 inch.

Prior to each measurement run in this experiment, the actual position of the beam pair convergence point/measurement volume was moved to a reference point and its location was confirmed visually. An adjustable iris stop was mounted on a short stand snugly fitted into the jet exit. This was used as a reference target. The plane of the iris stop was mounted at an angle of 45° to each axis of illumination. Thus, when all three beam pairs passed freely through the iris center, the measurement volume was demonstrated to be at the plane of the iris stop. After gross adjustment, the iris was reduced to its minimum size of 0.5mm, and the procedure was repeated. The motor controller counters were then reset to a step count corresponding to the known position of iris center, and all experimental positions determined relative to the reference point.

The limiting precision of the visual calibration was about ±0.5mm (±.020 inches). This was the primary source of uncertainty in the position of the measurement volume, rather than traverse precision. Optical distortions of the beam path due to variations in the

window glass are another source of positional uncertainty. The total uncertainty was not precisely determined, but is believed to be about ±.025 inches.

5.7 Particle Seeding System

Two different devices were used for introducing seed particles into the flowfield, both in combination and separately. Seed particles were introduced into the mean streamwise flow by means of a Rosco vapor condensation smoke generator located in the tunnel settling chamber upstream of the tunnel contraction section. The smoke was ducted to near the tunnel centerline by a flexible tube prior to release upstream of the test section.

The smoke generator was controlled remotely from the assembly area adjacent to the test section. In operation, the smoke was emitted in an approximately 10 to 20 second pulse, and allowed to circulate and mix for several tunnel circuits prior to taking measurements. The tunnel was operated with the air exchange doors closed during LDV measurements to minimize smoke loss. Additional smoke was emitted when the LDV data rate began to decline. The smoke generator produces a wide range of particle sizes, and the particle size and density tends to decrease with time as the particle fluid gradually evaporates.

During measurements in the jet core and wake region, seed particles were introduced into the jet flow by means of a seed generator vessel located upstream of the jet plenum chamber, as described in Chapter 2. The seed material was mineral oil. A small portion (< 10%) of the high pressure air flow was diverted through the seeder vessel to impinge as a low subsonic jet upon the surface of a mineral oil reservoir in the bottom of the vessel. Droplets produced by splashing at the surface were entrained in the general flow which exited the vessel at its top, and were re-mixed with the balance of the high pressure airflow before it entered the plenum chamber. Due to the large diameter of the seeder vessel relative to the supply lines, flow velocity in the seeder was low, and large drops settled back to the reservoir.

The vessel consisted of an 8 inch nominal diameter schedule 80 carbon steel pipe with welded bottom cap and flanged top plate. The vessel was designed and certified to ASME code as a pressure vessel for operation to 500 psi. A sight gage permitted mineral oil level to be monitored in operation. The mass flow of impingement air was not measured, but was adjustable by means of a bypass valve.

The jet seeder was adjusted to the minimal level of bypass air needed to give a reasonable data rate during LDV measurements in the jet exit region. The particle size distribution in the jet core flow is not known. It was visually apparent that mineral oil was deposited on the nozzle surface and macroscopic drops were emitted at the jet lip.

5.8 LDV Data Acquisition System

LDV experimental data acquisition was controlled by a mixed-language program written for this system in FORTRAN and QUICKBASIC. The program coordinated the operation of the traverse system, the Macrodyne counter/processor and autocorrelating data buffer, and the downmix frequency generator. A comprehensive interactive control program, including point-by-point statistics and graphics to monitor the performance of the LDV system, is important for efficient LDV data acquisition due to the many factors which can affect the quality of the data. It was determined to write such a program as a permanent part of the LDV system. Specification and coding for this program was begun prior to the preparations for this experiment. One goal of this experiment was to complete, test and debug the control program.

The mixed-language format was adopted for the control program because the control functions for the existing Macrodyne data buffer are only available as object code in Microsoft QUICKBASIC 4.5, and no manual operation option is available. However, QUICKBASIC is limited to relatively small programs using a single 64k memory segment. Therefore, QUICKBASIC was not a feasible choice for the primary control program. For this reason, it was decided to write the primary program in FORTRAN. At the time the

coding was begun, Microsoft claimed to support mixed-language operation using Microsoft FORTRAN 5.0 and QUICKBASIC 4.5 (due to various limitations, Microsoft has since retracted this claim).

Due to its distinctive dynamic memory management scheme, QUICKBASIC subroutines cannot run outside of an environment initiated by a QUICKBASIC main program. Thus the program was structured as a QUICKBASIC main program calling a FORTRAN primary routine, which in turn called a variety of QUICKBASIC and FORTRAN subroutines. This scheme has only been partly successful, and at the time of this experiment several program options were not functioning as part of the linked mixed-language executable program, even though all the subroutines were fully functional when run independently.

The experiment control program was designed to execute a predetermined measurement sequence to take a number of measurements along a specified linear axis. An initiation text file of a defined format specified the experimental parameters, and was edited prior to each run. This file was read by the program from disk storage prior to commencing data acquisition for each measurement run. The initiation file specified the beginning location, the increment and the end location of each experimental run. It also specified the number of burst samples for each measurement point, the channels to be used and the autocorrelation status of each active channel.

The program menu permitted the experimental points to be repeated as desired during the course of the run, based on the statistics of prior measurements. However, since the run-time graphics and histogram module was not functioning in the mixed-language environment, only gross signal failure could be assessed from program calculated statistics during a measurement run. In addition, the down-mix frequency generators were reset manually based on program calculated mean frequencies, since the frequency generator control subroutine was also not functioning in the mixed-language environment.

Following each measurement point, the control program calculates and displays both the measured mean Doppler frequencies, the standard deviation in frequency, and the new downmix frequency needed for each channel to center the measured frequency in the filter passband. The filters themselves are adjustable only manually, but do not ordinarily need to be changed during an experimental run. If it appears that a portion of the signal may have been truncated by the high or low pass filter, the point may be repeated with an adjusted downmix frequency.

5.9 LDV System Calibration

The fringe spacing determines the relationship between the particle velocity component normal to the fringe system and the detected Doppler frequency. The fringe spacing is a function of the laser wavelength and the convergence angle of the beam pair. Where Δx is the fringe spacing, ϕ is the half angle of convergence and λ is the wavelength, the relation is [23,24]:

$$\Delta x = \lambda/(2 \sin \phi) \qquad \text{(Equation 5.1)}$$

The laser line wavelengths are precisely known. However, since for practical LDV systems the beam pair convergence half-angle is quite small, the calculated fringe spacing is very sensitive to small measurement errors in the beam pair convergence angle. For this reason, it is very desirable to have a device which can produce a precisely known target velocity for calibration measurement.

The LDV system was calibrated by means of a spinning wheel calibrator developed at NASA/Ames [30]. The calibrator provides fine wire targets rotating at a precisely known tangential velocity near the rim of the wheel. The wire targets are approximately 50μ in diameter. With the wheel located so the the rim is moving perpendicular to the component fringe system, the Doppler frequency of the scattered light is measured. The calibration coefficient for the component channel is simply the ratio of the Doppler frequency to this tangential velocity.

The spinning wheel calibrator is mounted on a tripod or other stand in the test section and aligned normal to the axis of illumination of the beam pair. The target wheel itself is mounted on the shaft of a synchronous motor. It incorporates a 3 axis vernier traverse which allows the calibration wheel to be translated until the measurement volume is at the axis of rotation of the wheel.

The motor shaft has a very narrow hole drilled along its centerline, and a photocell is mounted at the far end of the shaft. The alignment of the measurement volume with the centerline can be determined by maximizing the photocell output voltage caused by laser light transmitted through the hole. The intensity of this light reduces rapidly as the measurement volume moves off center.

Once the measurement volume is at the centerline of the shaft, the vernier traverse can be used to move it to a measured radial distance (near 2 inches) adjacent to the fine target wires mounted near the wheel rim. Since the synchronous motor is slaved to rotate at an exact ratio of the 60 Hz line frequency, both the angular velocity (1800 rpm) and radius (measured) are thus determined. From these, the tangential velocity is calculated.

The Macrodyne counter processor has a remote enabling feature that can be used to suppress burst detector function when the wire support spokes of the spinning wheel intersect the beam pair. Magnets located on the wheel generate a synchronizing signal which enables the detector for a time window sufficient to measure light scattered by each wire as it passes. The calibration procedure was repeated for each of the three beam pairs.

Calibration measurements were made using a sample size of 1000 bursts acquired over about 6 seconds. Thus any instantaneous variations in target velocity due to mounting vibration or motor torque oscillation were averaged out. The line current frequency is very stable. The precision of the vernier traverse is about $\pm$ .001 inch.

The largest source of uncertainty is the precision of determination of the alignment of the measurement volume with the shaft centerline, since this is done by visually seeking the maximum photocell voltage on an analog voltmeter. However, this uncertainty appears

to be no more than a few thousandths of an inch. For this reason, the calibration accuracy is believed to be about $\pm 0.1\%$.

5.10 Experimental Procedure

Prior to experimental use, the laser was warmed up, and overlap alignment of the beam pairs was confirmed visually by projecting the measurement volume on a transparent plastic ruler. The signal quality was then determined without tunnel flow by means of a portable seed generator. This generator produced a fine mineral oil mist by the same principle as the jet seeder, using shop compressed air supply. The outflow from the seed generator was ducted through a 1/2 inch vinyl tube and exhausted into the measurement volume. This formed a small laminar jet of a velocity of a few feet per second.

For each channel in turn, the filtered analog signal output from counter/processor was displayed on the frequency analyzer. When the optics and photomultipliers were properly adjusted, a distinct narrow Doppler frequency line very near the value of the effective bias frequency was observed above the general system noise. A trial data point was then acquired to demonstrate the functioning of the burst detector and data acquisition system. Generally a signal-to-noise ratio of greater than 10 decibels was needed for reliable measurement.

In order to avoid direct impingement of the jet upon the upper window of the test section, the tunnel velocity was brought up to speed prior to opening the high pressure air valves for jet flow. The flow conditions were allowed to stabilize for several minutes prior to measurements. This allowed the tunnel drive motors and power supply to reach a stable operating temperature, with improved velocity stability. The high pressure air system and heater also needed several minutes to reach a stable air temperature, due to the high thermal mass of that system.

The clock of the 386 PC used to acquire LDV data was synchronized with the clock of the VAX computer of the SWTS system used to acquire tunnel and jet flow data. The

time of each measurement was stored as part of the permanent data file. In post-test processing, the FORTRAN data reduction program read both the LDV and the SWTS data files in order to correlate the LDV data with the corresponding flow data, as is discussed in Section 5.12.

The general practice was to begin each sequence of LDV measurements in a region in which the velocity was expected to be near freestream value. The measurements would then follow a prescribed sequence of constant distance increments under the control of the data acquisition program into the target flow region. The initial dowmmix frequency was estimated so as to give a detected mean Doppler frequency near the center of the counter/processor filter passband. The width of the filter passband was generally maintained at 6.0 MHz, while the standard deviation in detected frequency rarely exceeded 0.6 to 0.7 MHz in the most turbulent regions, and was more typically about 0.1 to 0.2 MHz. Thus, allowing for $\pm$ 3 standard deviations as the effective signal bandwidth, there was generally a comfortable margin for error in the downmix setting without hazard of truncating the signal.

All traverse motion during a run was controlled automatically by the data acquisition program using the initiation file prescription for the run. However, the position was monitored visually and by reference to the motor controller front panel display.

As the data acquisition sequence progressed from point to point, the required change in downmix, if any, was calculated and displayed based on the prior point. The signal generators were then reset prior to the next point. Only in regions of very high velocity gradients, such as entering the jet shear layer, was it necessary to repeat a measurement point to avoid a truncated signal.

During a measurement run, the signal quality was monitored periodically by means of the frequency analyzer. The trigger threshold of the counter/processor digitizer and the seeder output were adjusted to give a data rate of about 5 to 10 detected bursts a second. This was done both to obtain a sample averaged over a time of about one minute, and to

reduce spurious counts due to system noise. Generally, when the standard deviation in Doppler frequency of a measurement point substantially exceeded that of the immediately previous measurements without an apparent physical basis (such as a high turbulence intensity shear region), the measurement was repeated.

The majority of the LDV data was taken with the autocorrelation coincidence fuction selected for the streamwise and vertical components. These were both forward scatter signals, and had generally high signal-to-noise ratios. Attempts to use all three channels in the coincidence mode were unsuccessful, due to the marginal signal strength of the backscatter channel measuring the lateral component of velocity. The 3 channel coincidence mode would have been advantageous to reduce the likelyhood of spurious burst data, and to reduce the positional uncertainty by eliminating measurements from particles outside the small 3-D fringe overlap region

For measurements taken within 1/2 inch of the surface of the groundplane, the lateral velocity component channel using the vertical beam pair was not active. Even with a clean mirror surface on the groundplane, the reflected specular light so close to the measuring volume would swamp the diffuse signal being received. This would risk damaging the photomultiplier tube and would render the signal useless. For this reason measurements near the boundary layer were limited to the plane of symmetry where the mean lateral component was expected to be near zero.

5.11 Test Conditions

The LDV measurements of jet-in-cross-flow features were in three different regions: (a) The first consisted of velocity measurements in a cross-sectional plane in the developed jet plume. The plane was perpendicular to the predicted vortex path of the plume. (b) The second consisted of velocity measurements in the plane of symmetry of the model in the inflow region upstream of the jet, near the surface of the groundplane. (c) The

third consisted of measurements in the plane of symmetry of the model in the jet wake region upstream of the jet, near the surface of the groundplane.

In addition to measurements of cross-flow features, measurements were taken of the isolated jet and mean flow in two regions. Measurements were taken in a traverse across the jet core near the exit plane, and measurements were taken of the flow at a distance above the ground plane with the jet flow stopped.

All measurements were made with a jet Mach number of 0.5, and the tunnel velocity was adjusted to yield the desired effective velocity ratio. Due to the length of time required to make LDV measurements, it was not possible to acquire a matrix of data over the range of effective velocity ratios and jet Mach numbers for which pressure data was obtained. The majority of measurements were made at a effective velocity ratio of 8, with limited measurements at an effective velocity ratio of 6.

5.12 Data Reduction and Analysis

The Doppler frequency data for each measurement point were stored on the hard disk of the 386 PC. Separated data files were maintained for each data point of a traverse position sequence. A separated file was also created for any repeated measurement at a position, where failure of the data acquisition system or signal was suspected. As the computational subroutine of the data acquisition program had not yet been fully debugged, only the mean Doppler frequency and standard deviation of samples was available on a real time basis as measurements were being taken.

A separate FORTRAN program was written to reduce the data from the stored data files. The data reduction program read both the LDV and the SWTS data files in order to correlate the LDV data with the corresponding flow data, calculated velocities and statistics, and produced a comprehensive point-by-point data spreadsheet file. The spreadsheet file was directly loadable into the personal computer applications used to produce graphic displays and data tables. A copy of this program is included in the

Appendix. In addition, the non-functioning graphics subroutine of the data acquisition program was revised as a stand-alone program which allowed the Doppler frequency data files to be viewed as frequency histograms.

The instantaneous velocity of each burst sample was computed for each component, and the standard deviation of the cumulative samples determined. The samples were then resorted to exclude spurious burst samples resulting from data acquisition failures in which a zero value of the Doppler frequency was returned. The number of such null samples was recorded, and the point statistics were then recomputed. For the great majority of measurement points such null samples were rare or absent. In most instances where many null samples were present in the data file, the measurement quality had been recognized during the test run, and the measurement had been repeated.

Based on the standard deviation determined after removal of null samples, the samples were resorted to remove samples where the velocity was more than three standard deviations from the mean value. The mean value and statistics were then recomputed. This was done to reduce the effect of spurious burst detection due to high signal noise on the mean velocity determination.

5.13 Results and discussion.

Measurement Fields. Figure 5.8 gives a lateral view of the areas of the jet flowfield in which LDV measurements were made. Measurements were made in the plane of symmetry both in front and behind the jet near the surface. Due to the close proximity of the measurement volume to the groundplane surface, the backscatter channel was turned off for measurements at the leading edge of the jet, and thus no values of the v component were measured. Intense reflection swamped the signal in this channel. For measurements in the wake region, the distance from the groundplane was sufficient for the lateral component to be resolved.

Cross-sectional measurements were made in two locations in the developed jet plume at values of R of 6 and 8. The choice of location was estimated to intersect the vortex curve path of the plume at an approximately normal angle to the plume path. The coordinates were chosen to correspond to those used in Reference 12 to allow direct comparison with total pressure rake survey data. The vectors depicted in Figure 5.7 are the resultant of the values measured in the symmetry plane. Measurements were also made at lateral offsets of 2 and 4 jet diameters to intersect the plume vortex pair.

Leading Edge of Jet. Figure 5.9 shows in vector form the measurements made at a value of R = 8, near the jet leading edge. The magnitudes are normalized by the test section mean velocity, shown as scale vectors. It can be seen that, except near the surface, the measured flow grades from near freestream values to about 60% of freestream velocity as the jet exit is approached. This deceleration of flow is expected from the positive surface pressures measured in this location, as described in Chapter 3.

The values measured in the jet core do not appear to be realistic, with the vertical component being only about 40% or less of the predicted jet velocity. This discrepancy was found in all measurements made in the jet core region. The reason for this discrepancy is not known, but may be related to the characteristics of the mineral oil seeding used in the jet flow. The particle size distribution is not known, but at least some large droplets could be seen in the jet flow near the lip.

Figure 5.10 show a CFD solution as particle traces near the jet exit, taken from Reference 14. The solution uses the Baldwin-Lomax turbulence model and grid 2, which had a fine grid pitch in the jet boundary region. Although this solution is at R = 6, it provides at least a qualitative comparison with the LDV measurements at R = 8. The down turn of the steamlines near the jet lip is shown to be quite similar to the measurements in Figure 5.9. In addition, the reverse flow measured at z = 0.0125 D at x values of -1.250 D

and -1.125 D may correspond to the reverse flow pattern shown in the particle traces in Figure 5.10.

Wake Region. Figure 5.11 shows the measurements made in the near-surface wake region. The vectors represent the resultant of symmetry plane components, and the contours represent the out-of-plane lateral component. The vectors indicate that there is a saddle point present at about 1.5 D aft of the jet centerline. Forward of this point the flow is being entrained into the jet. The contours show a limited region of strong lateral motion between 1 and 2 D aft of the jet.

Figure 5.12 shows an oil flow photograph from Reference 4, made at R = 5.5. The photograph shows a clear saddle point at approximately x = 2 D. Figure 5.13 shows measurements taken from Reference 3 for a 2 inch diameter jet. This data show lateral cross-sectional velocities in planes located at 0.98 and 1.97 D. A well defined vortex pattern is indicated at x = 1.97 D and z = 0.5 D. Such a lateral vortex pattern, with some asymmetry, may account for the lateral component shown in Figure 5.11.

Jet Plume Region. Figure 5.14 shows cross-section measurements made at R = 8, M_j = 0.50 compared with measurements from Reference 12 made at the same values of these parameters. Note that the lateral locations (y/D) are not exactly the same for the measured and reference data, but are close enough for general comparison. The data are shown for the half-plane only. In both cases, the vectors show the in-plane components, and the contours show the total magnitude of velocity.

In both sets of data in Figure 5.14 the lateral locus of maximum velocity magnitude is at about 2 D from the plane of symmetry. However the vertical locus (in cross-section coordinates) is about 1.125 D higher for the reference data, and there is a substantial difference in the direction of the in-plane vectors. This difference may be due to the effect of tunnel ceiling blockage. The reference data is made with a model located 39 jet diameters from the test section ceiling, and the model groundplane in this study was 26.5

diameters from the ceiling. Although the larger jet (4 inches) of the reference data also indicates a factor of 2 difference in Reynolds number, tunnel wall effect is a more plausible basis for this rather large difference in jet path (1.125 D difference at a height of 6.56 D).

Figure 5.15 show a comparison of plume path for various computational conditions from reference 14 compared with experimental data taken from Reference 12, both for R = 6. The computational boundary was set at z = 20 D, compared to 39 D for the experiment. The results showed the computational path was consistently lower than the experimental data. At R = 8, it would be expected that the wall influence would be even greater.

Figure 5.16 compares measured data with the same reference data as figure 5.14, but with the vertical position of the reference data lowered by 1.125 D. The contours in this case represent the out-of-plane component, rather than the total velocity. In addition, the data are reflected about the symmetry plane for ease of visualization (the centerline values are measured values). In the region in which the two sets of data overlap, the direction and magnitude of the in-plane vectors are in good agreement, and the figure as a whole shows a consistent vortex flow pattern. The alignment of the contours is also generally good. The locus of maximum velocity on the centerline is above of the measurement region.

Figure 5.17 shows in-plane vectors and out-of plane contours of velocity for R = 6. The pattern is generally similar to that of figure 5.16. As would be expected, the velocities are generally lower than those measured at R = 8.

CHAPTER 6

Conclusions and Recommendations

The goals of this investigation were to obtain improved data on the surface pressure distribution on the groundplane surrounding the jet exit, and complete the assembly and programming of the 3-D fixed-focus orthogonal laser Doppler velocimeter for the 7x10 foot wind tunnel, and to evaluate its performance in measuring the flowfield in a jet-in a crossflow.

The measured surface pressure data constitutes a useful extension of prior data. The relatively high precision of the PSI 8400 transducer system made this possible. Possible oil contamination of some ports during related LDV measurements caused measurement failures on a few of the ports, however, causing small discontinuities in the measurement pattern. This demonstrates the importance of planning the experiment to avoid such conflict.

The unsteady pressure measurements were not successful. As was noted, the experimental hardware was not intended for this purpose. However, small individual transducers are available which may be mounted directly on the groundplane, flush with the surface. This would eliminate any damping due to tubing. A high sampling rate would be necessary to resolve relevant frequencies. A rate of 1000 Hz or more is desirable.

The schlieren photographs taken are a valuable means of visualizing the jet plume structure. The optical system specifically designed for the 7x10 ft tunnel was effective in obtaining these large field photographs, due to the large mirror diameter. The equipment

proved relatively dependable in spite of the high vibration level present during tunnel operation.

The LDV system was demonstrated to be effective in the general flowfield, but was not successful in obtaining measurements in the high velocity jet core region. The reason for this limitation is not known, and further development of this capability is needed. The adaptation of the system to use time-domain processors would be highly beneficial. This would be especially useful in the weak backscatter channel.

Further developement of the LDV data acquisition system is needed to permit automated operation with near real-time graphical monitoring of the data received. One of the primary limitations in the use of the present system is the great amount of time required for each measurement.

REFERENCES

1. Margason, R. J., "Fifty Years of Jet in Cross Flow Research," 72nd AGARD Fluid Dynamics Panel Meeting, Winchester, U.K., April 1993.

2. Margason, R. J., "Analysis of the Flow Field of a Jet in a Subsonic Crosswind, in Analytic Methods in Aircraft Aerodynamics," NASA SP-228, 1969, PP. 683-702.

3. Snyder, P. and Orloff, K. L., "Three-Dimensional Laser Doppler Anemonmeter Measurements of a Jet in a Crossflow," NASA TM-85997, 1984.

4. Soullier, A., "Testing at S1.MA for Basic Investigations on Jet Interactions; Distributions of Pressures and Velocities in the Jet Using the Ideal Standard Nozzle (in the Unheated State)," NASA TT F-14072, 1972.

5. Williams, J. and Wood, M. N., "Aerodynamic Interference Effects with Jet Lift Schemes on VSTOL Aircraft at Forward Speeds," AGARDograph 103, Aerodynamics of Power Plant Installation, part 2, Oct. 1965, pp 625-651.

6. Margason, R. J., "The Path of a Jet Directed at Large Angles to a Subsonic Free Stream," NASA TN D-4919, 1968.

7. Smy, J. R. and Ransom, E. C. P., "The Structure of Single Jets at Large Angles to a Cross-Flow," Hawker-Siddeley Aviation LTD, HSA-KAD-R-GEN-2288, June 1976.

8. Bradbury, L. J. S. and Wood, M. N., "The Static Pressure Distribution Around a Circular Jet Exhausting Normally From a Plane Wall Into an Airstream," CP No. 822, British A.R.C., 1965

9. Fearn, R. L. and Weston, R. P., "Induced Pressure Distribution of a Jet in a Crossflow," NASA TN D-7916, July, 1975

10. Thompson, A. M., "The Flow Induced by Jets Exhausting Normally From a Plane Wall into an Airstream," Ph. D. Thesis, Univ. of London, 1971.

11. Fearn, R. L. and Weston, R. P., "Induced Velocity Field of a Jet in a Crossflow," NASA TP-1087, May 1978.

12. Fearn, R. L. and Weston, R. P., "Velocity Field of a Round Jet in a Cross Flow for Various Jet Injection Angles and Velocity Ratios," NASA TP-1506, Oct. 1979.

13. Aoyagi, K. and Snyder, P. K., "Experimental Investigation of a Jet Inclined to a Subsonic Crossflow," AIAA-81-2610, December, 1981

14. Chiu, S., Roth, K. R., Margason, R. J., and Tso, J., "A Numerical Investigation of a Subsonic Jet in a Crossflow," AIAA 93-0870, January, 1993.

15. Zucrow, M. J. and Hoffman, J. D.,Gas Dynamics, Vol. 1, John Wiley and Sons, New York, 1976

16. Kuethe, A. M. and Chow, C., Foundations of Aerodynamics: Bases of Aerodynamic Design, John Wiley & Sons, New York, 1976.

17. Schlichting, H., Boundary-Layer Theory, McGraw-Hill Book Co., New York, 1979.

18 Fearn, R., Doddington, H. and Westphal, R., "LDV Studies of a Jet In a Crossflow," Naval Air Development Center Report No. NADC-80238-60, 1981

19. Landenburg, R. W., et al, ed., High Speed Aerodynamics and Jet Propulsion, Vol. IX, Physical Measurements in Gas Dynamics and Combustion, Princeton University Press, Princeton, 1954, p27, 398.

20. Bradley, J. N., Shock Waves in Chemistry and Physics, Methuen & Co., London, 1962, p144-145

21. Jenkins, F. A., and White, H. E.,Fundamentals of Optics, 3rd ed., McGraw-Hill, New York, 1957, p258

22. Weinstein, L. M., "An Improved Large-Field Focusing Schlieren System," AIAA 91-0567, 1991.

23. Durrani,T. S. and Greated, C. A., "Laser Systems in Flow Measurement," Plenum Press, New York, 1977

24. Durst, F., Melling, A. and Whitelaw, J. H., Principles and Practice of Laser-Doppler Anemometry, Academic Press, London, 1976

25. Meyers, J. F. and Hepner, T. E., "Investigation of Particle Sampling Bias in the Shear Flow Field Downstream of a Backward Facing Step," Fifth Inter. Symposium on Applications of Laser Techniques to Fluid Mechanics, Lisbon, July 1990.

26. Orloff, K. L., Snyder, P. K. and Reinath, M. S., "Laser Velocimetry in the Low-Speed Wind Tunnels at Ames Research Center," NASA TM-85885, 1984

27. Snyder, P. K., Orloff, K. L. and Reinath, M. S., "Reduction of Flow-Measurement Uncertainties in Laser Velocimeters with Nonorthogonal Channels," AIAA-83-0051, 1983.

28. Kjelgaard, S. and Weston, R., "Advanced Data Acquisition and Display Techniques for Laser Velocimetry," AIAA-91-0272, 1991.

29. Meyers, J. F., "Laser Velocimeter Data Acquisition and Real Time Processing Using a Microcomputer," Fourth Inter. Symposium on Applications of Laser Anemometry to Fluid Mechanics, Lisbon, July 1988.

30. Snyder, P. K.,"Spinning Disk Calibration Device for Laser Doppler Anemometer," patent pending, 1983.

31. Benek, J. A., Bruning, P. G. and Steger, J. L., "A 3-D Chimera Grid Embedding Technique," AIAA-85-1523, 1985.

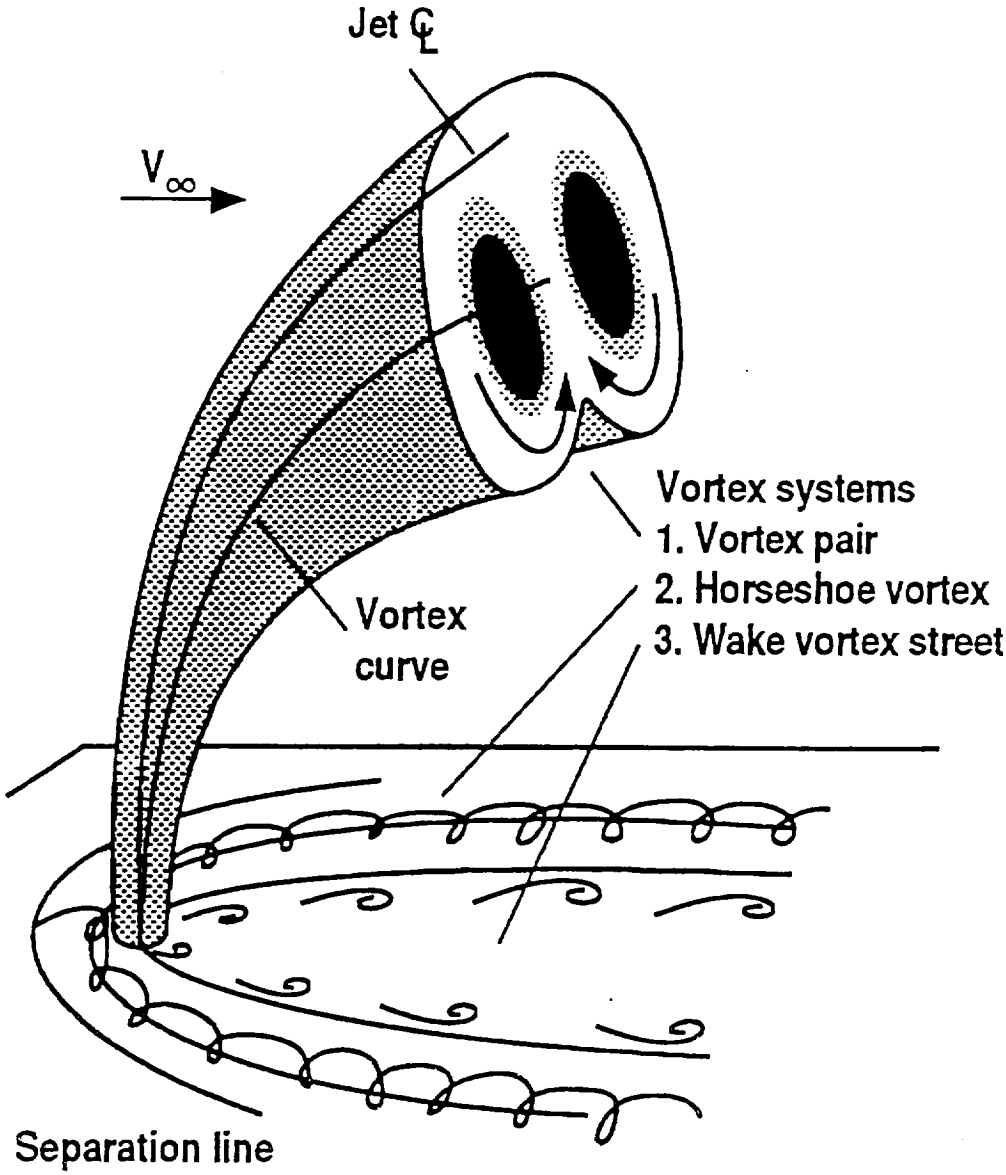

Figure 1.1. Components of flowfield of a jet in a crossflow.

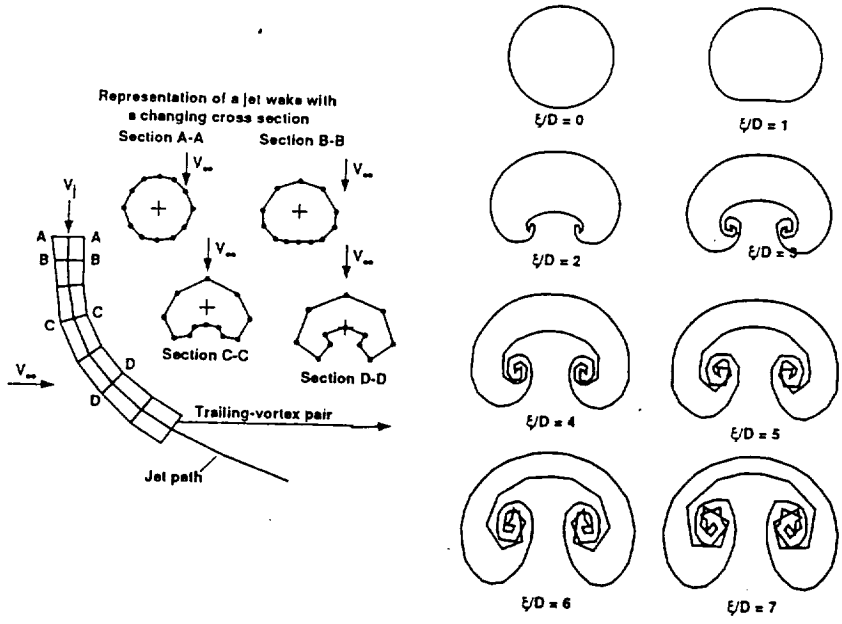

Figure 1.2. Calculated cross-sections of jet plume vortex pair.

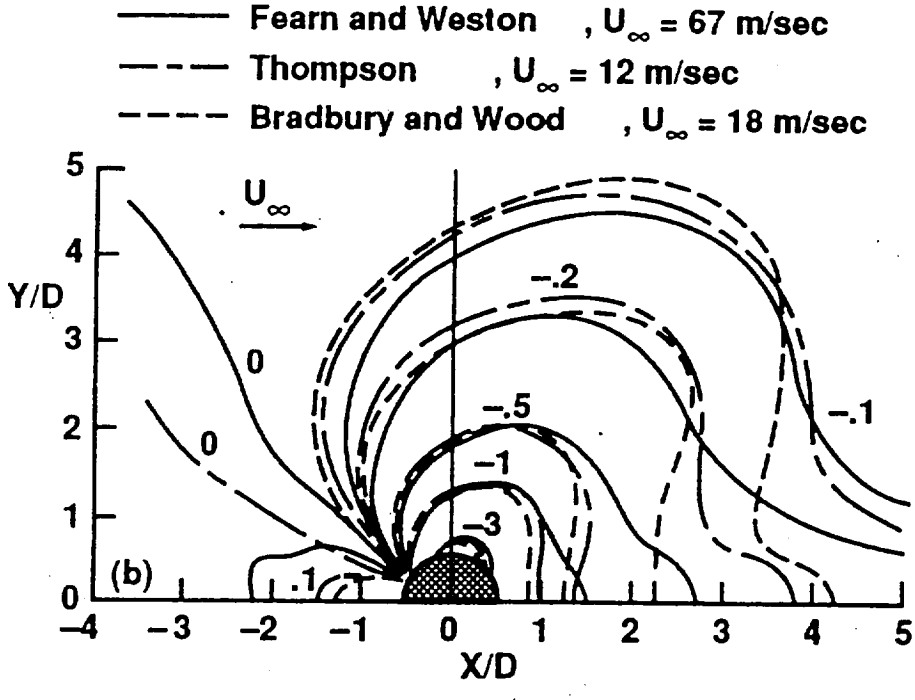

Figure 1.3. Comparison of experimental surface pressure data at R = 4.0.

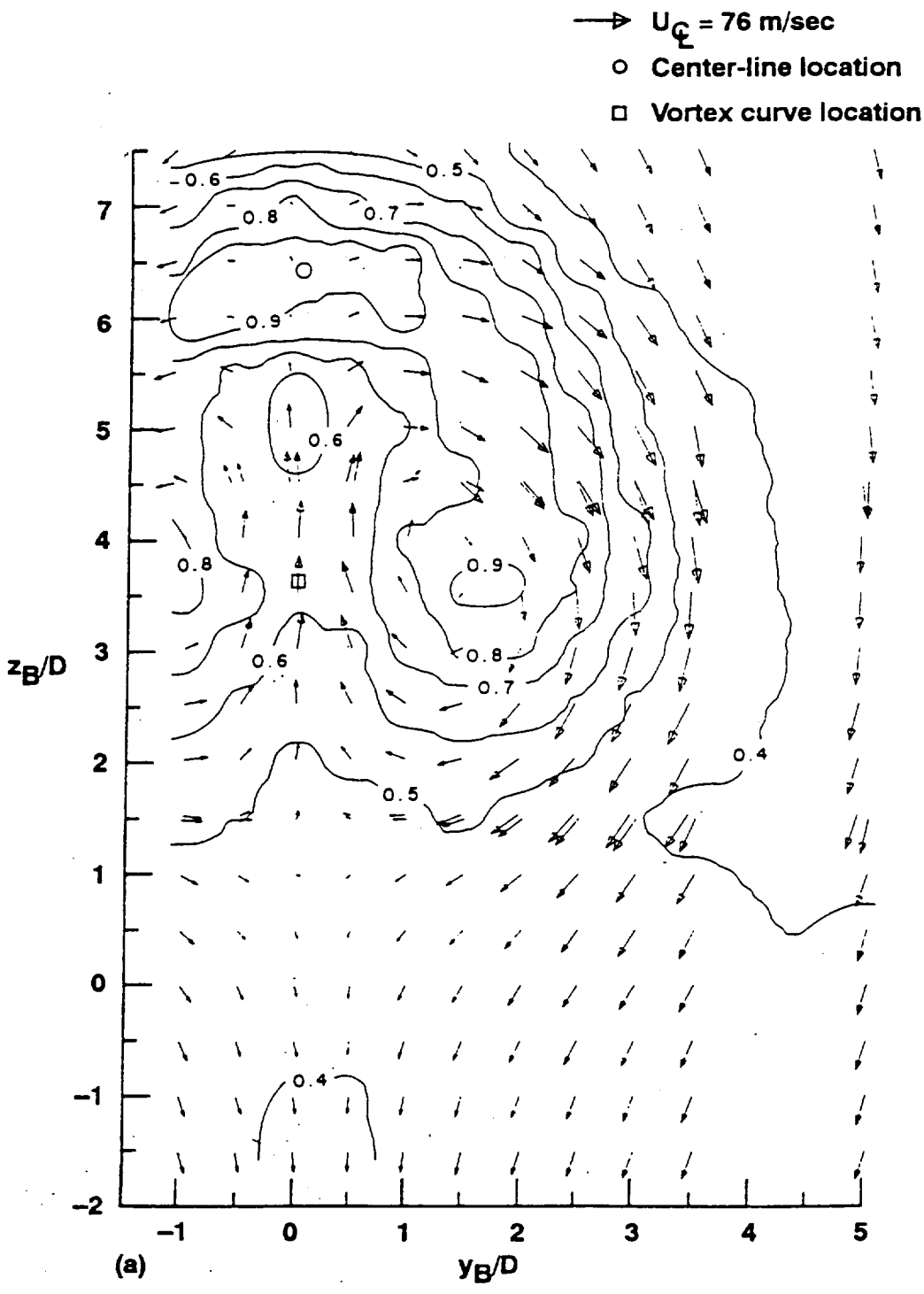

Figure 1.4. Measured in-plane velocity vectors and out-of-plane contours. R = 4.0; α = 42 deg.; x/D = 7.60; z/D = 4.81.

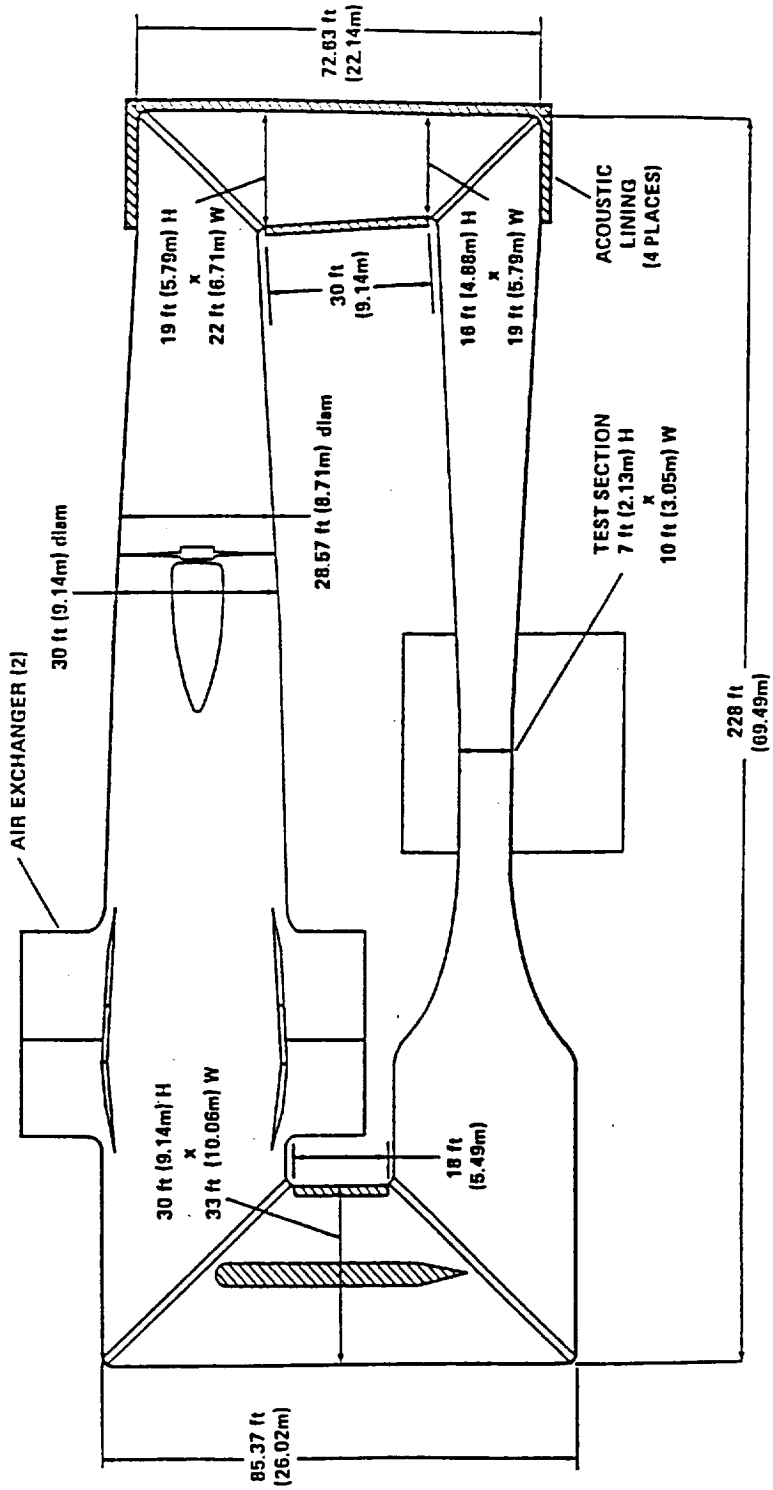

Figure 2.1. General layout of the NASA Ames 7x10 Foot Wind Tunnel No. 1.

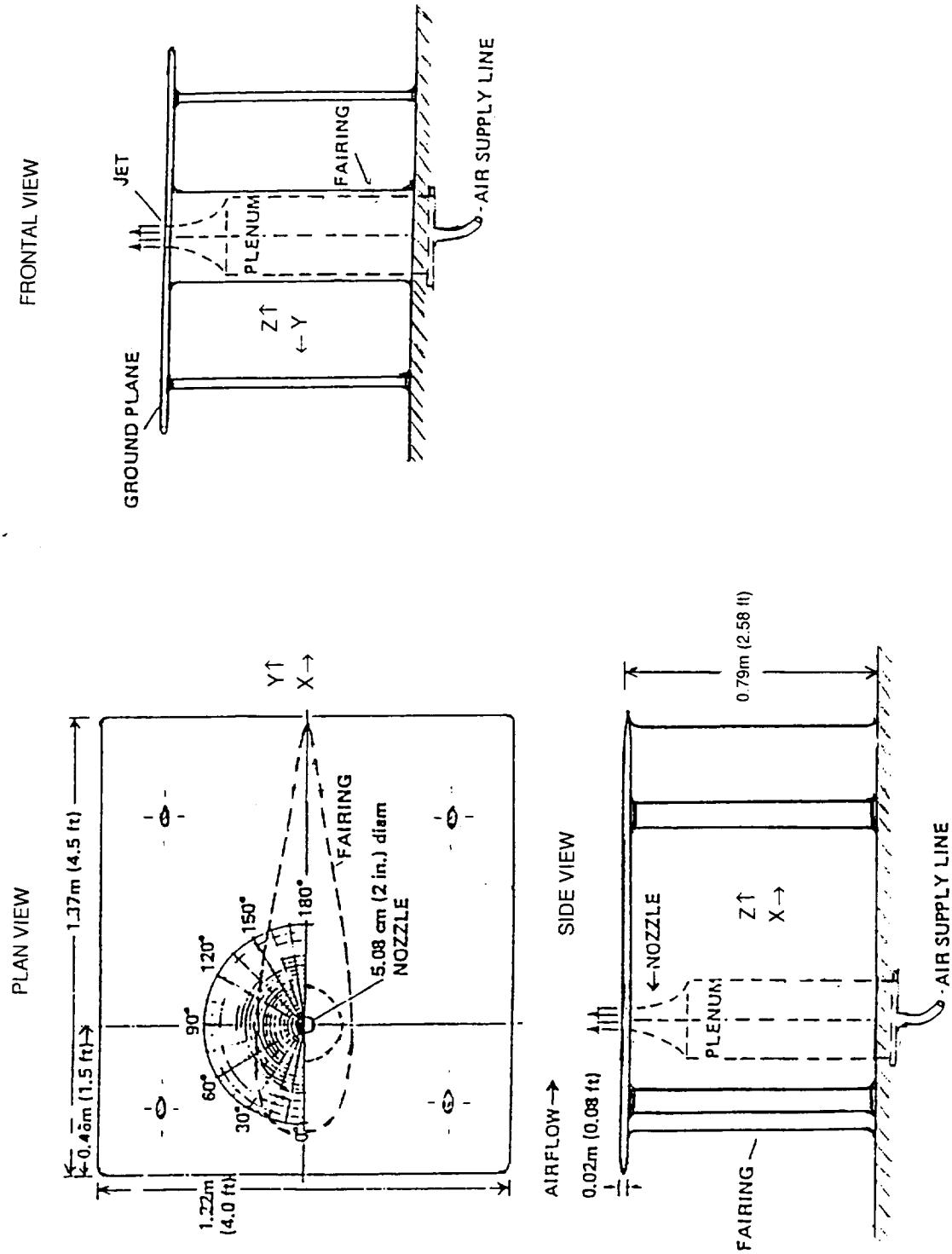

Figure 2.2. Diagram of the jet-in-a-crossflow model.

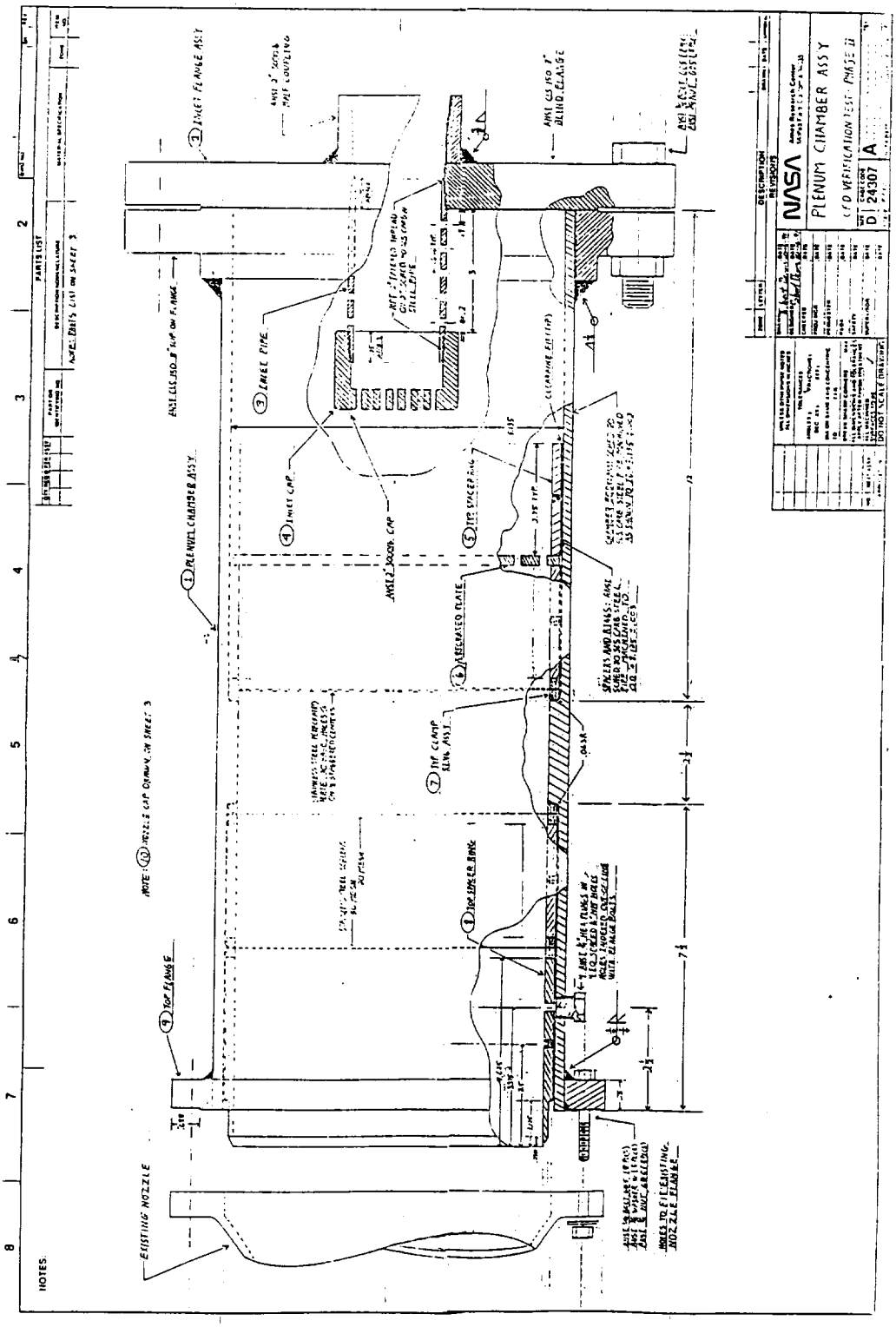

Figure 2.3. Diagram of the jet nozzle plenum chamber.

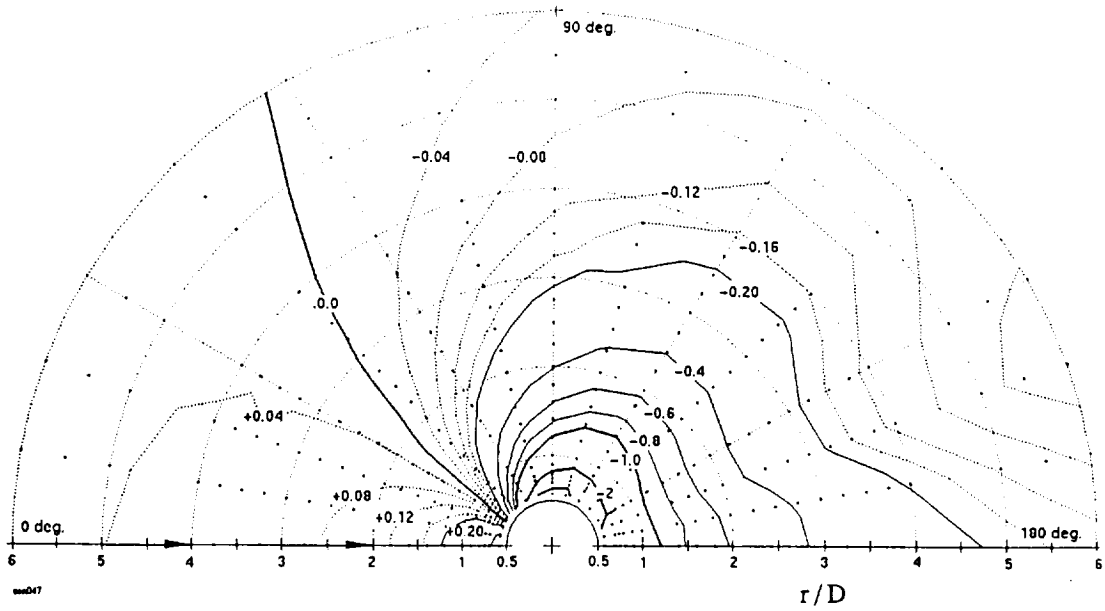

Figure 3.1. Contours of induced surface pressure coefficient at R = 4.0 and M_j = 0.74.

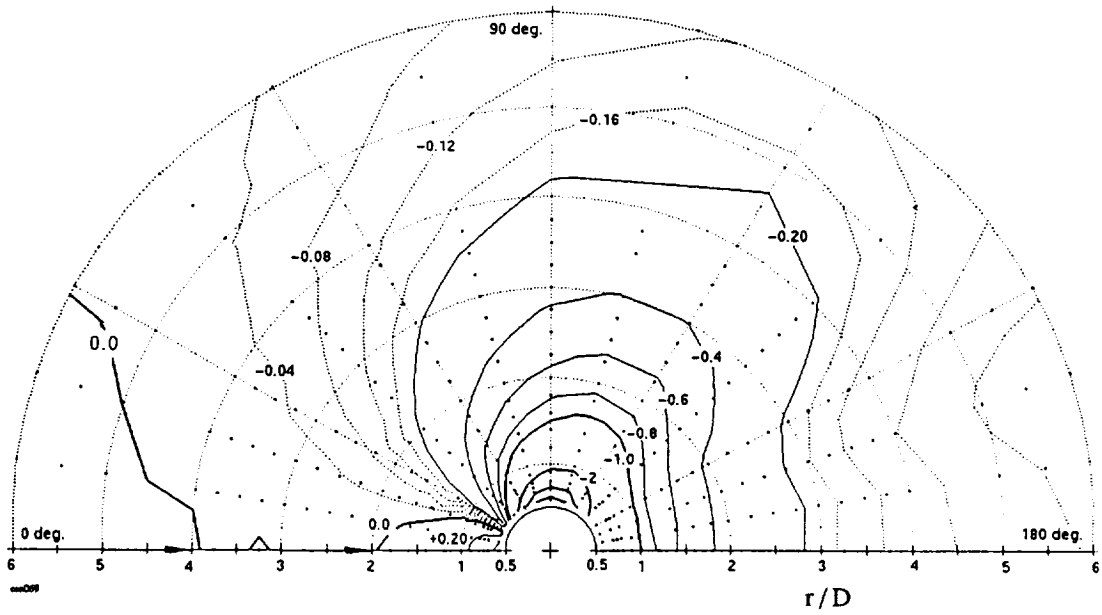

Figure 3.2. Contours of induced surface pressure coefficient at R = 6.0 and M_j = 0.91.

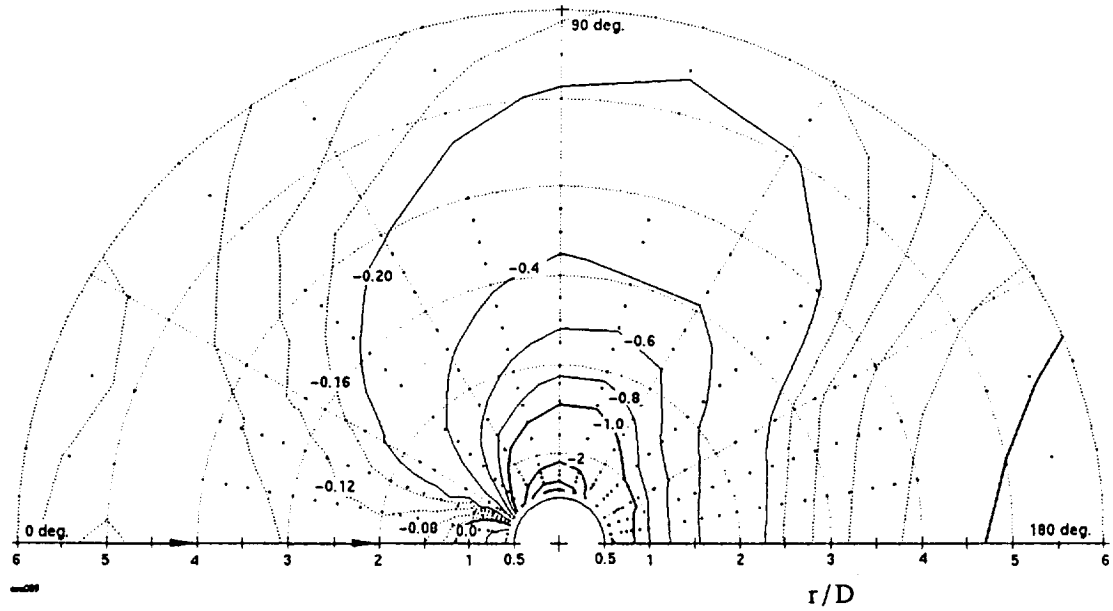

Figure 3.3. Contours of induced surface pressure coefficient at R = 8.0 and M_j = 0.91.

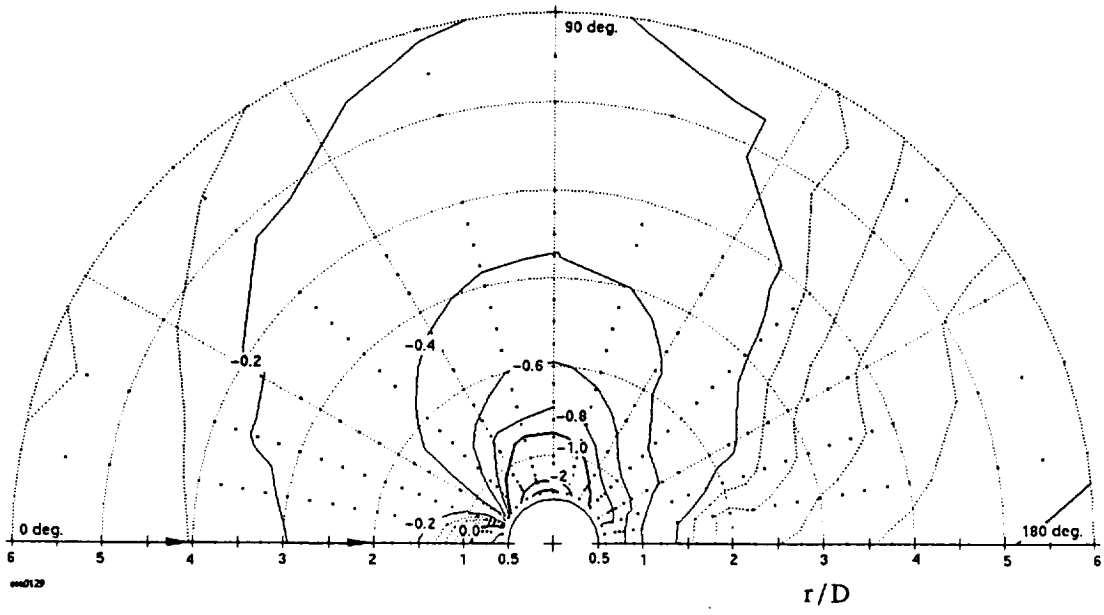

Figure 3.4. Contours of induced surface pressure coefficient at R = 12.1 and M_j = 0.91.

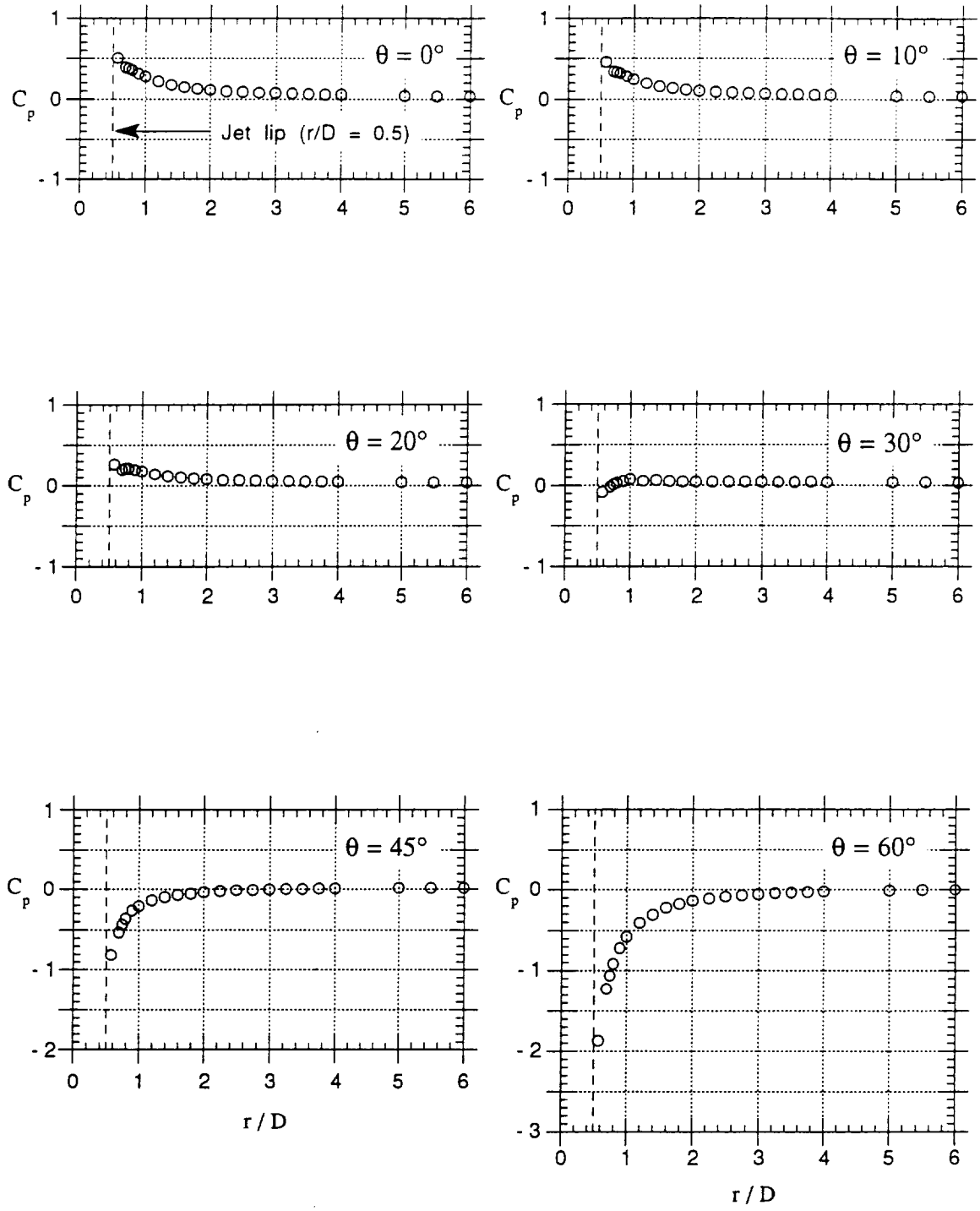

Figure 3.5. Radial induced pressure distribution by angle from leading edge at R = 4.0 and M_j = 0.74.

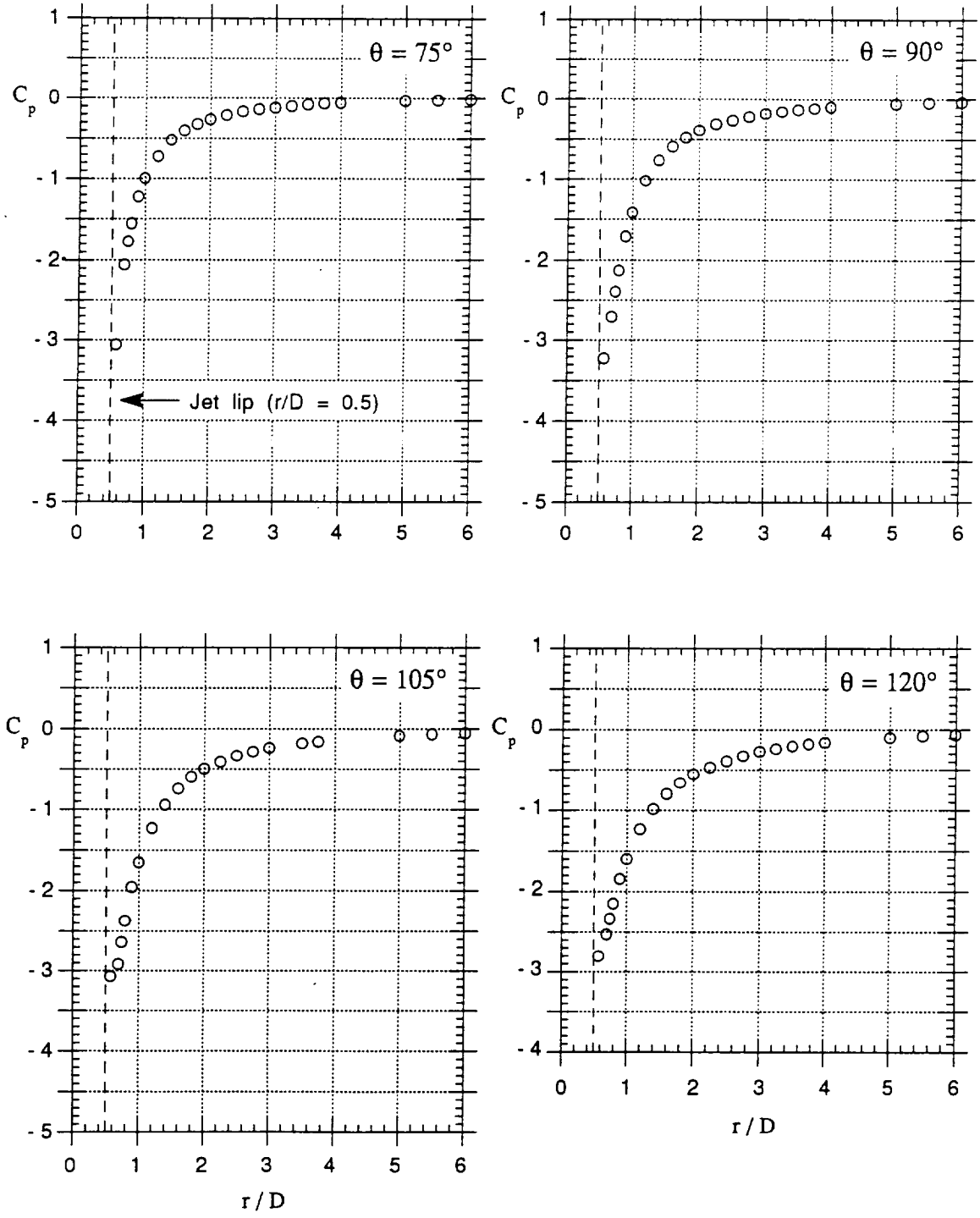

Figure 3.5. Continued.

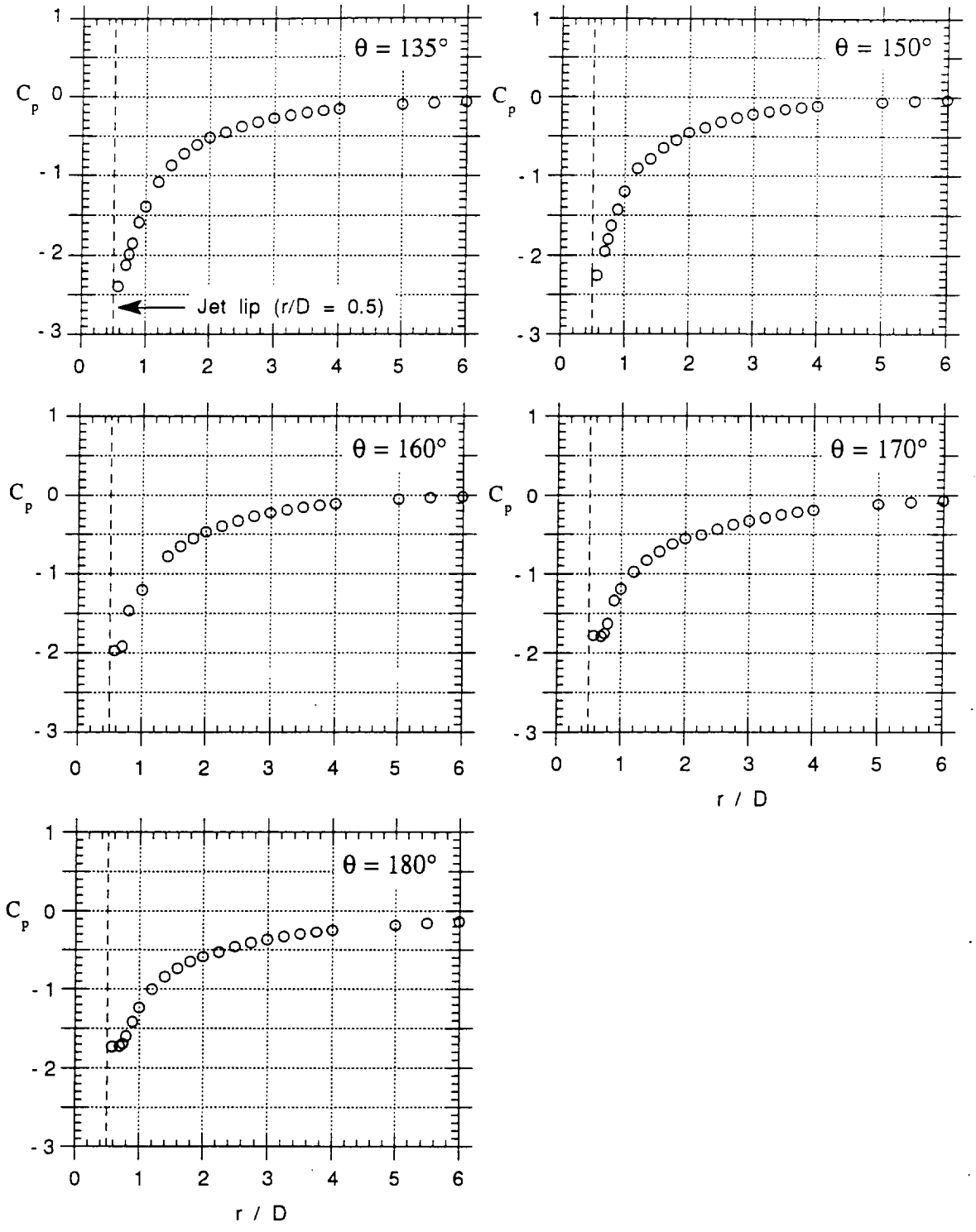

Figure 3.5. Continued.

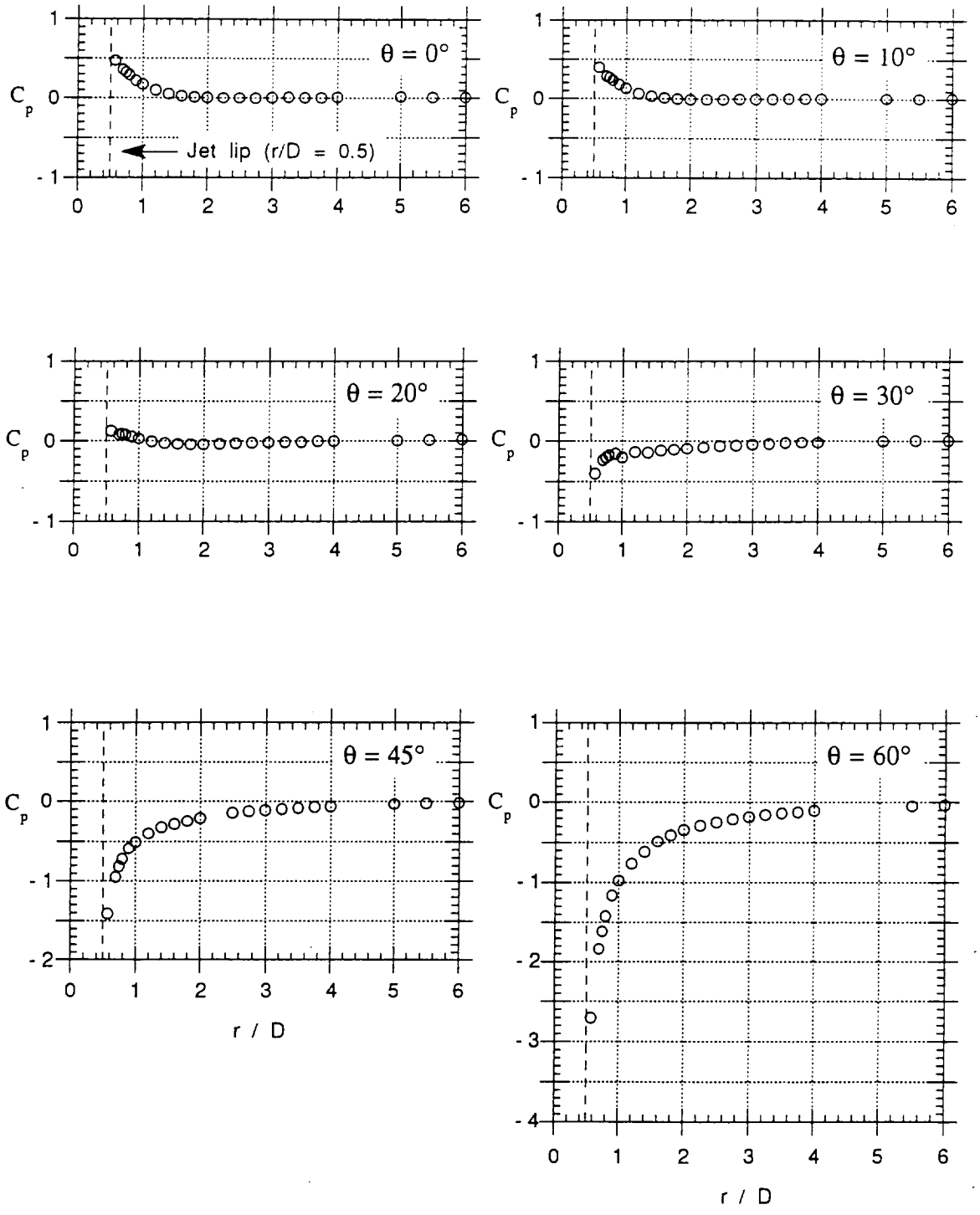

Figure 3.6. Radial induced pressure distribution by angle from leading edge at R = 6.0 and M_j = 0.91.

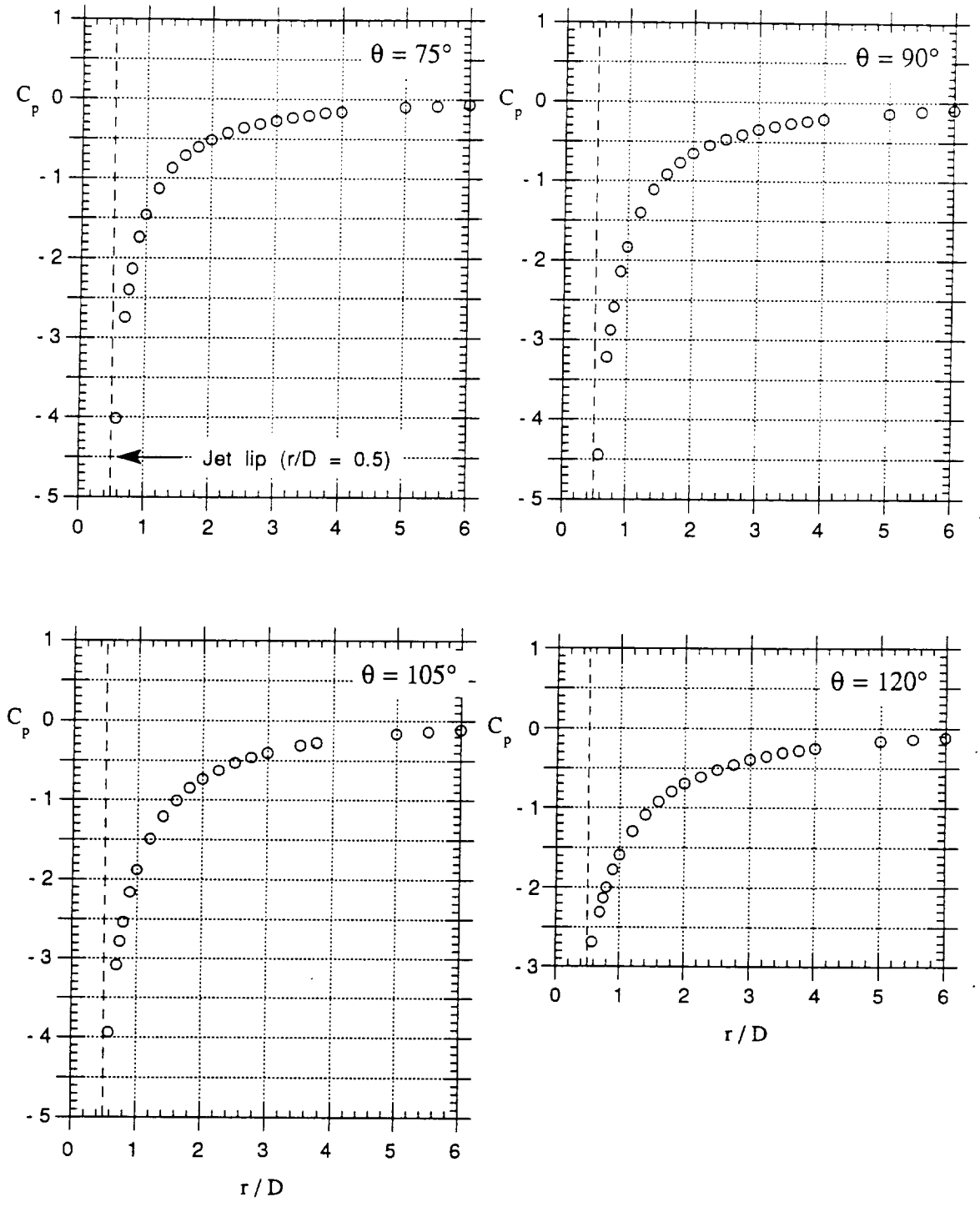

Figure 3.6. Continued.

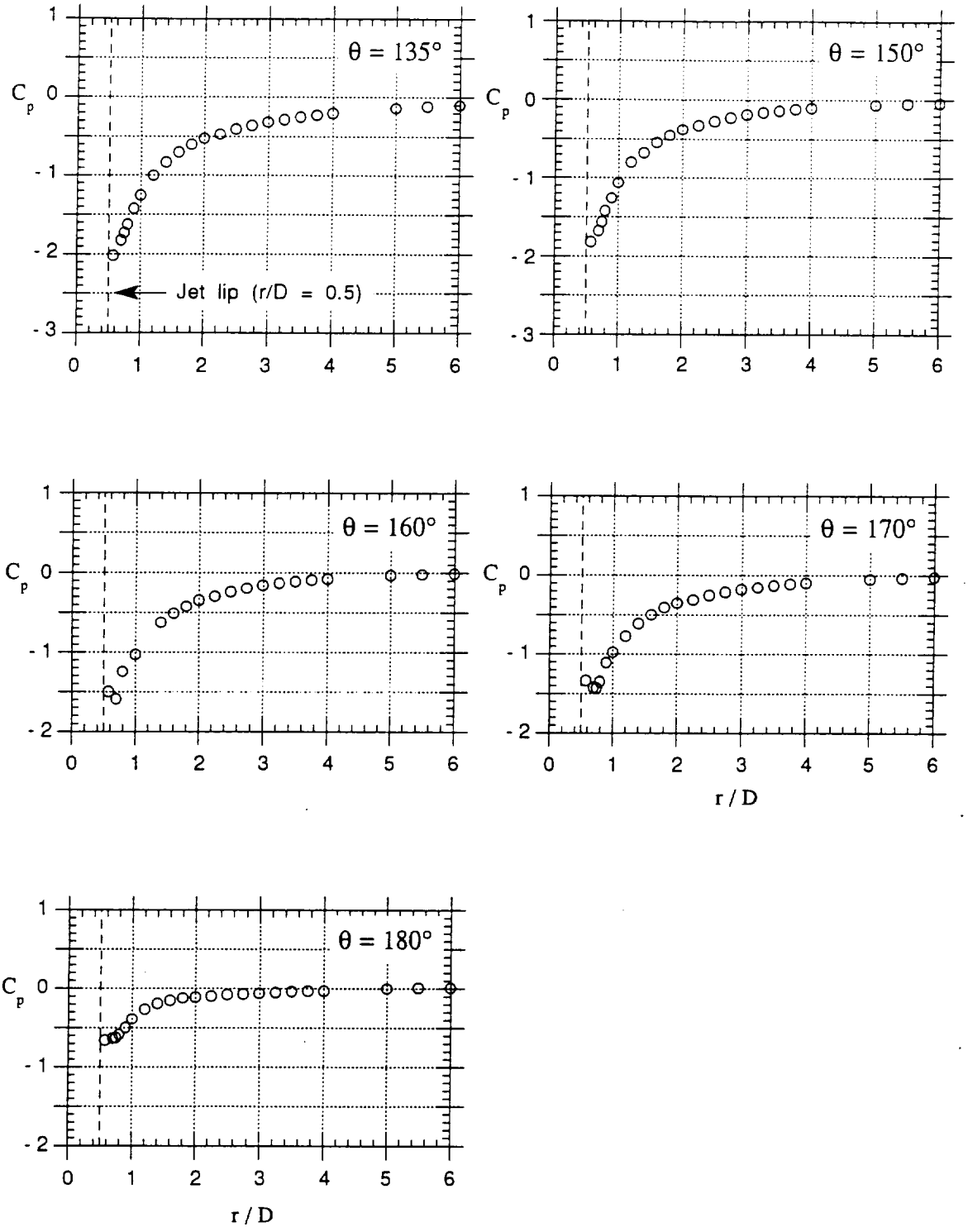

Figure 3.6. Continued.

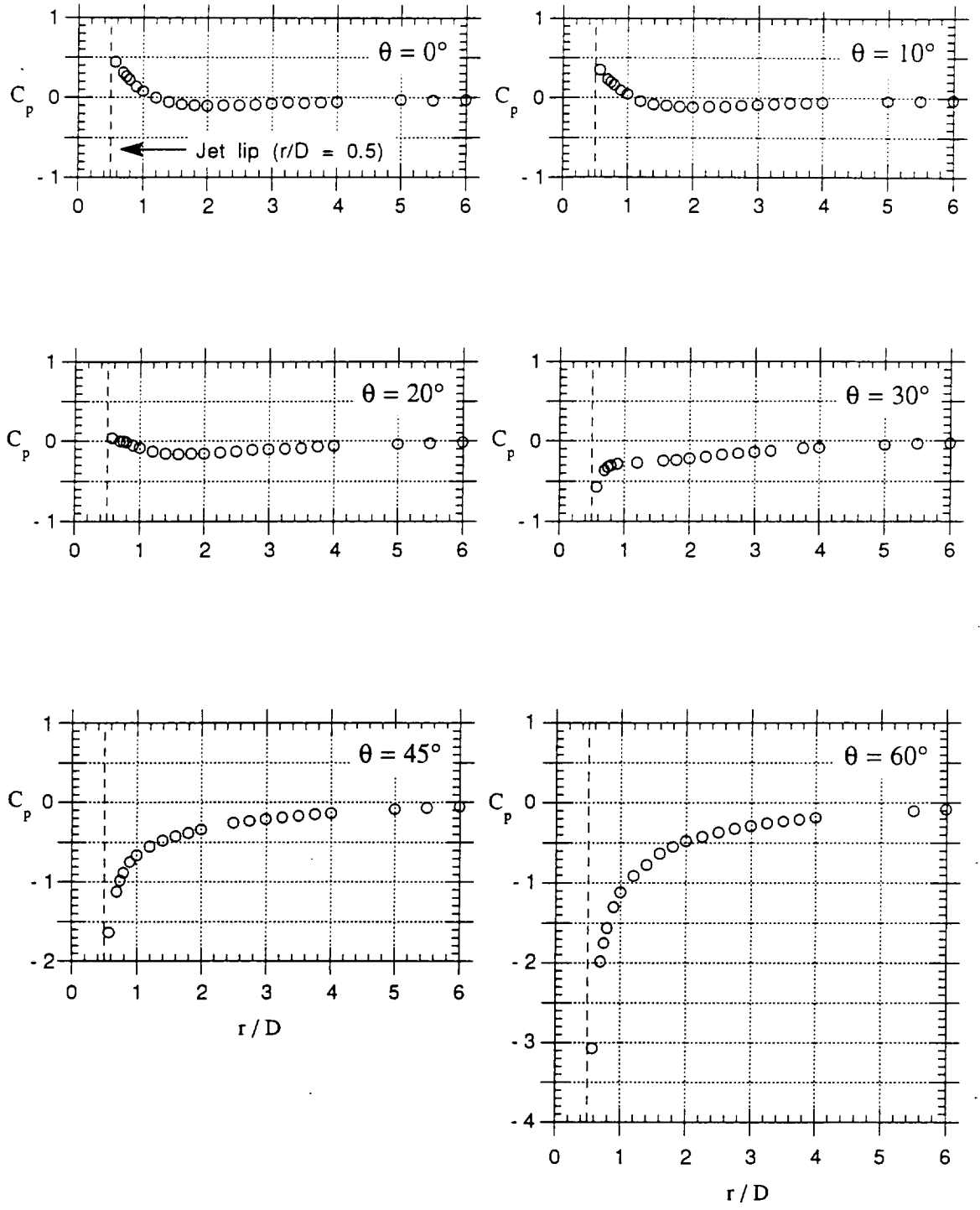

Figure 3.7. Radial induced pressure distribution by angle from leading edge at R = 8.0 and M_j = 0.91.

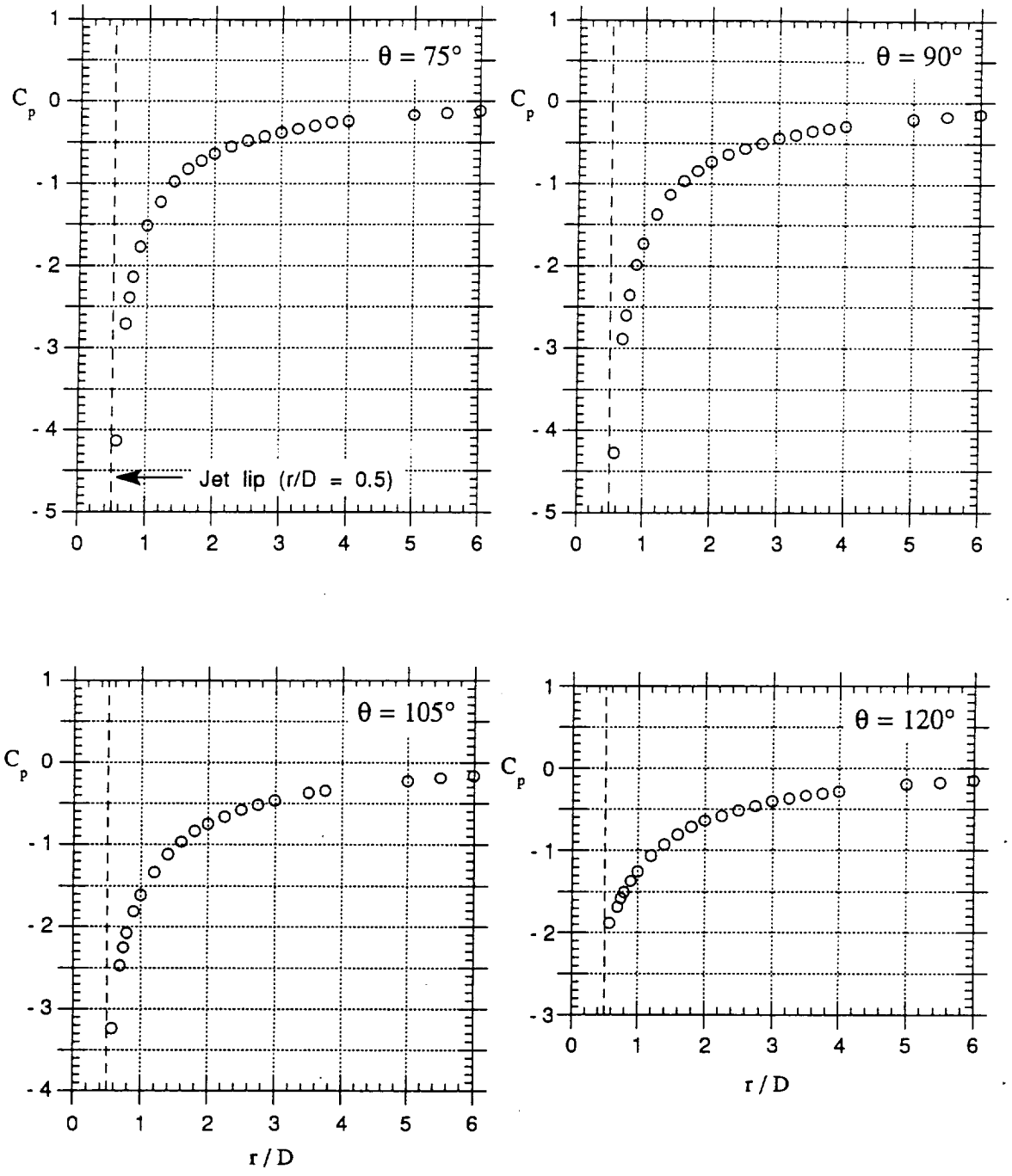

Figure 3.7. Continued.

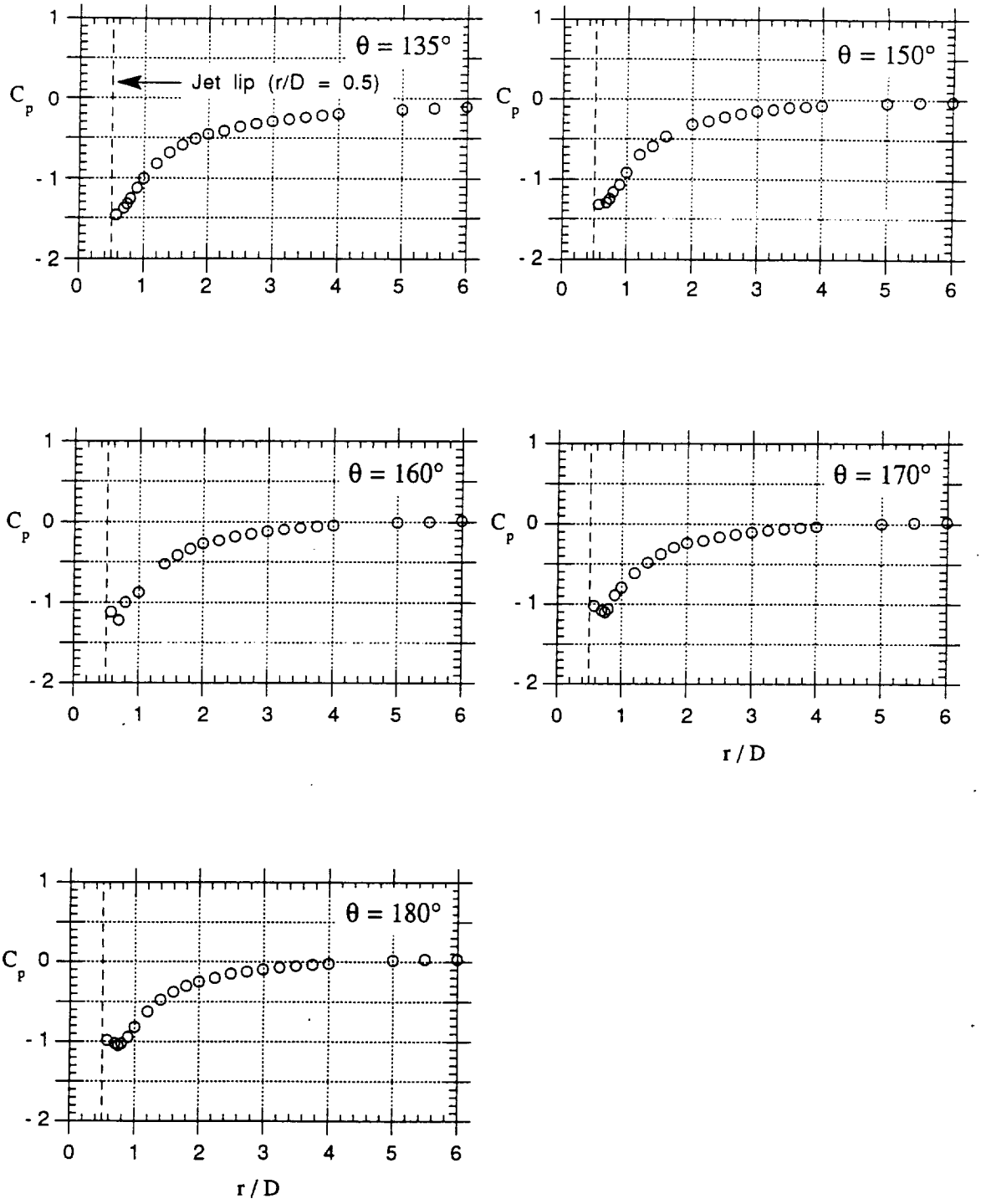

Figure 3.7. Continued.

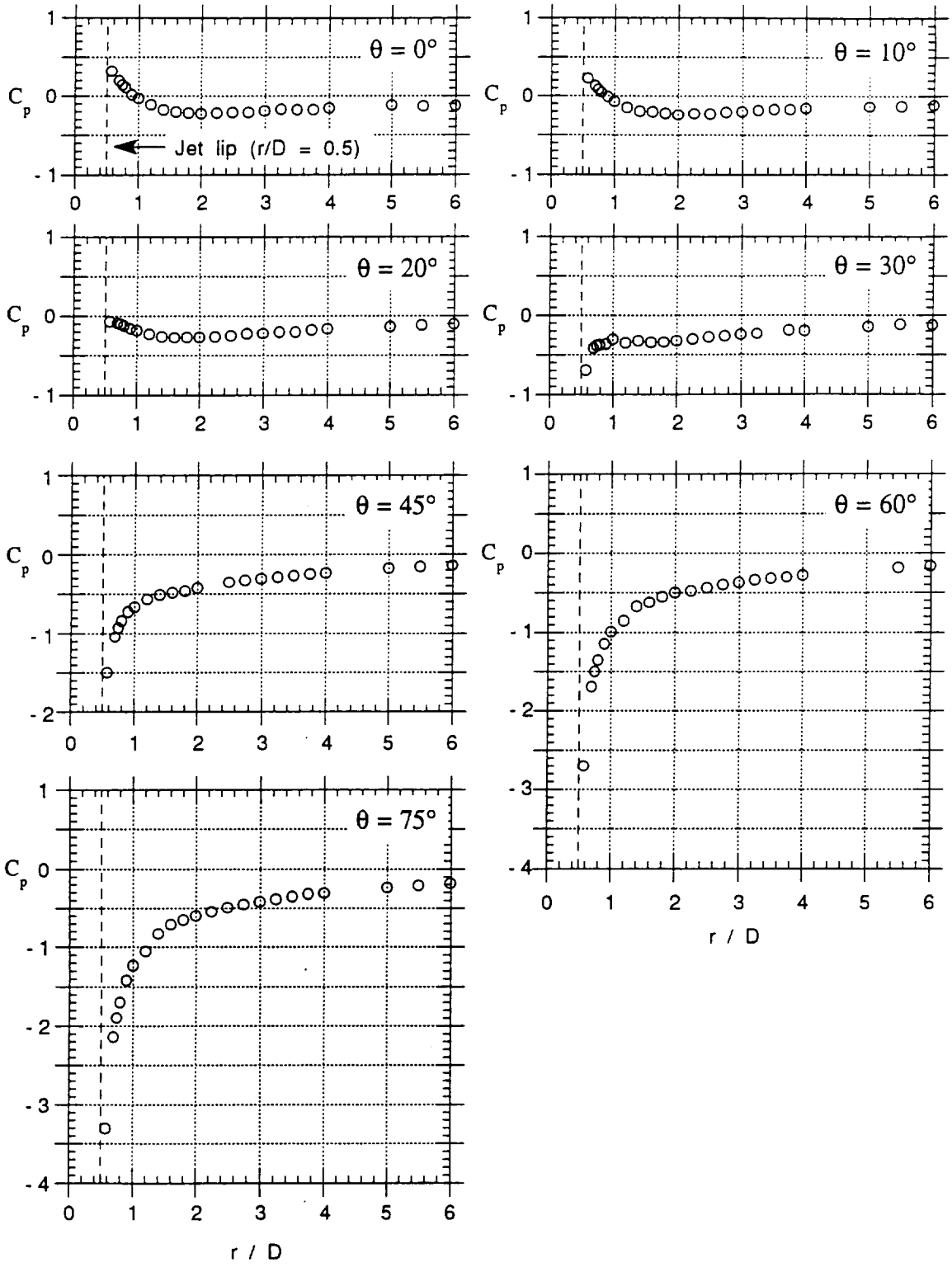

Figure 3.8. Radial induced pressure distribution by angle from leading edge at R = 12.1 and M_j = 0.91.

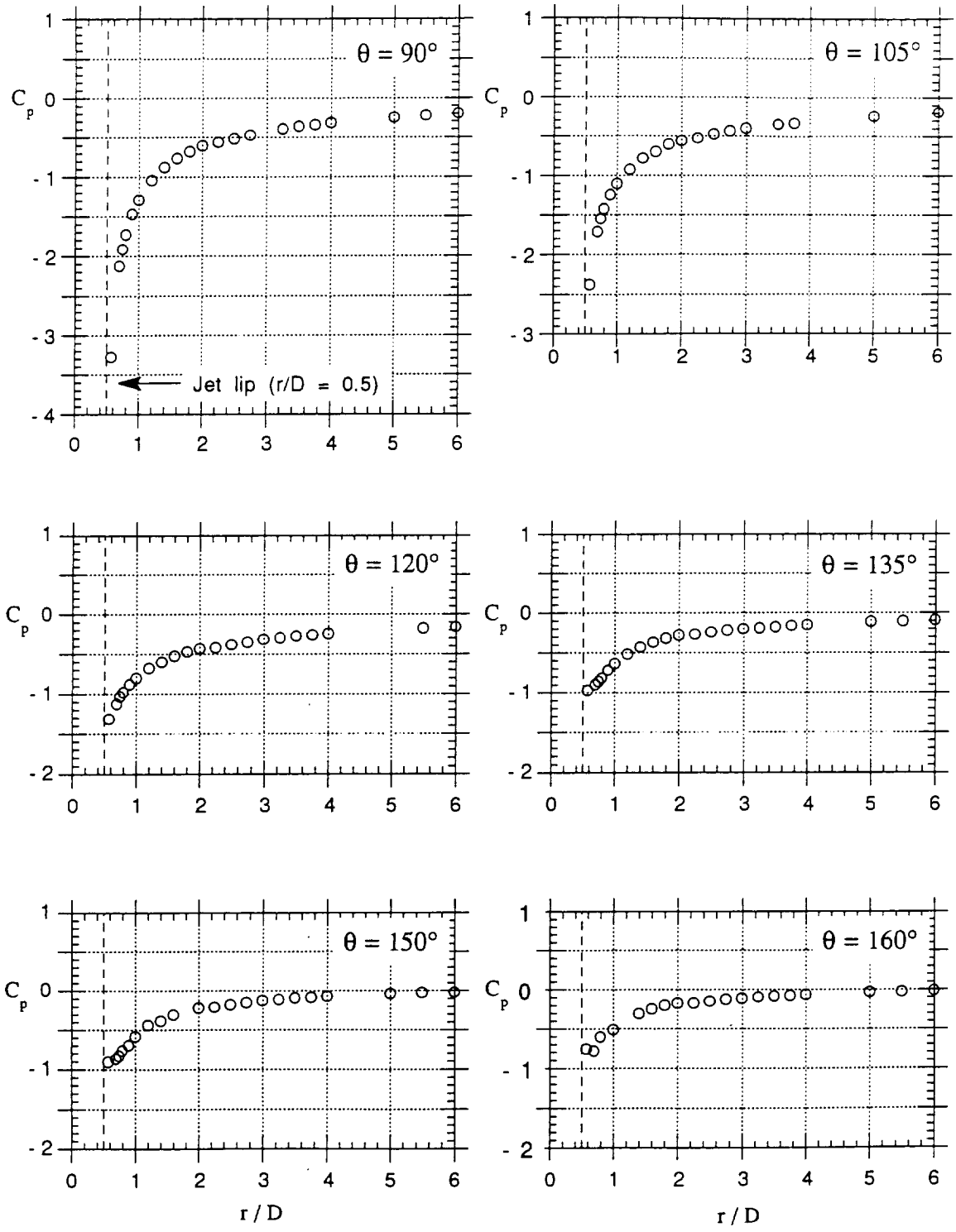

Figure 3.8. Continued.

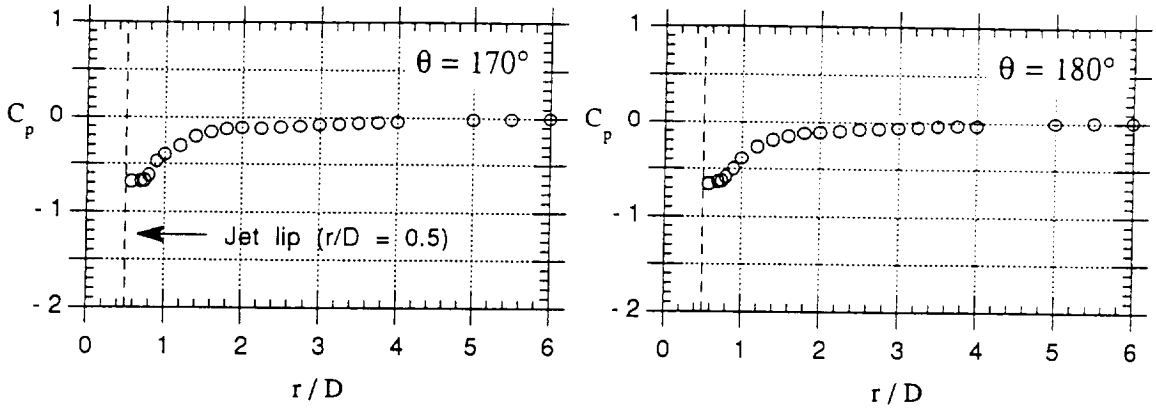

Figure 3.8. Continued.

C-2

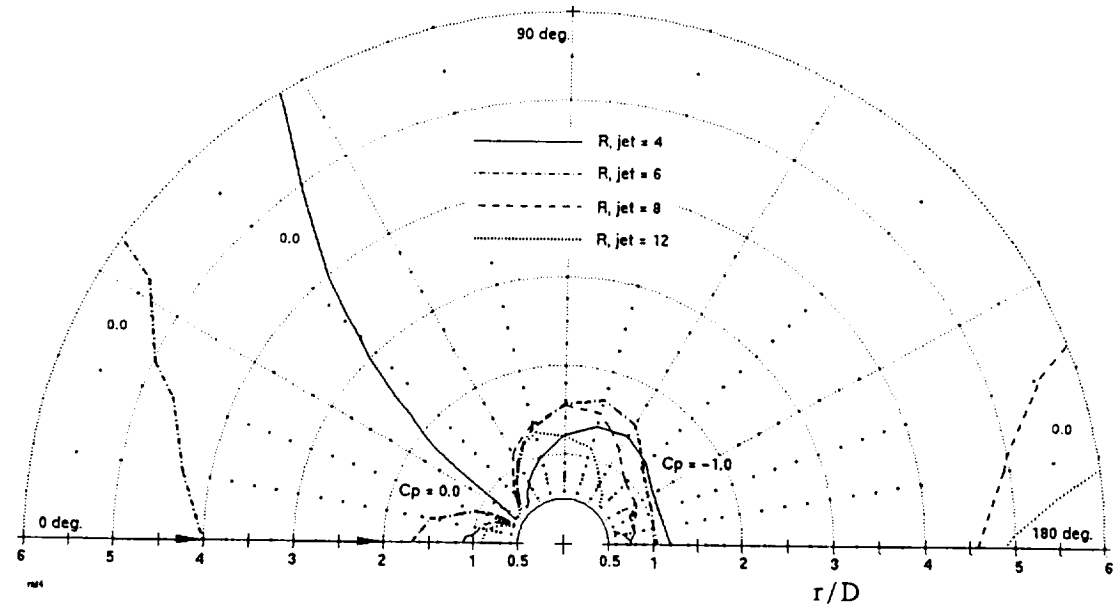

(a) Contours of C_p = 0.0 and -1.0

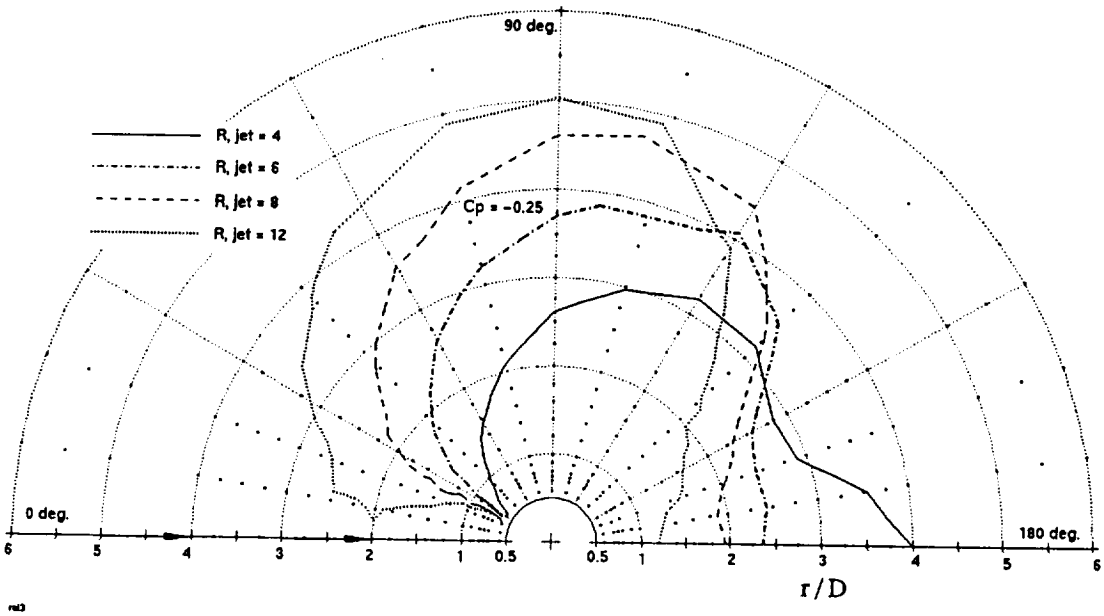

(b) Contours of C_p = -0.25

Figure 3.9. Effect of velocity ratio on pressure distribution at M_j = 0.74.

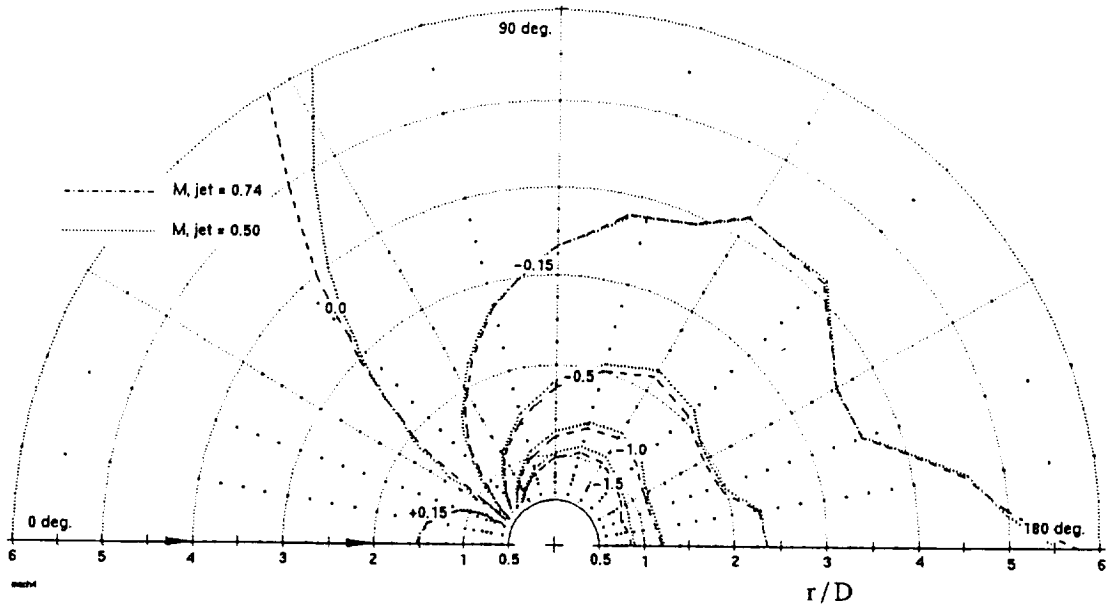

Figure 3.10. Effect of jet Mach number on pressure distribution at R = 4.0.

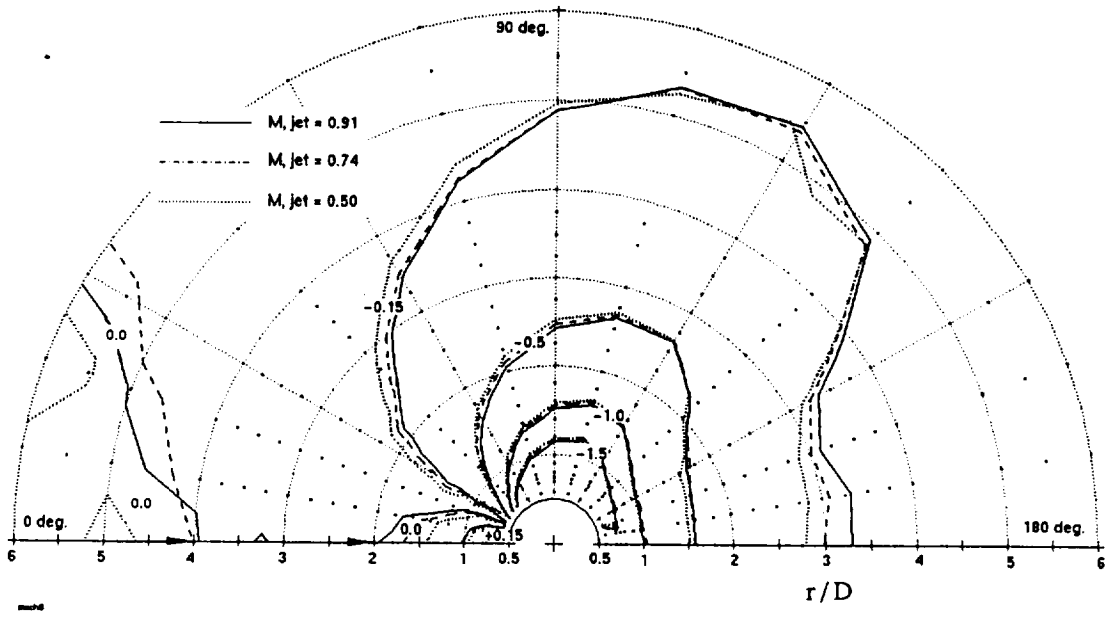

Figure 3.11. Effect of jet Mach number on pressure distribution at R = 6.0.

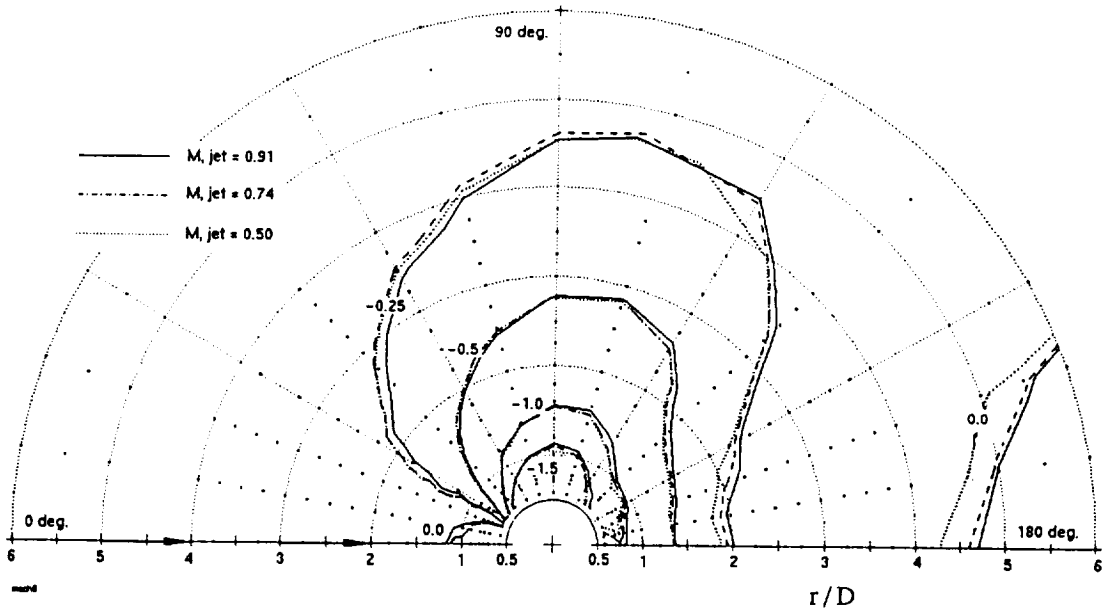

Figure 3.12. Effect of jet Mach number on pressure distribution at R = 8.0.

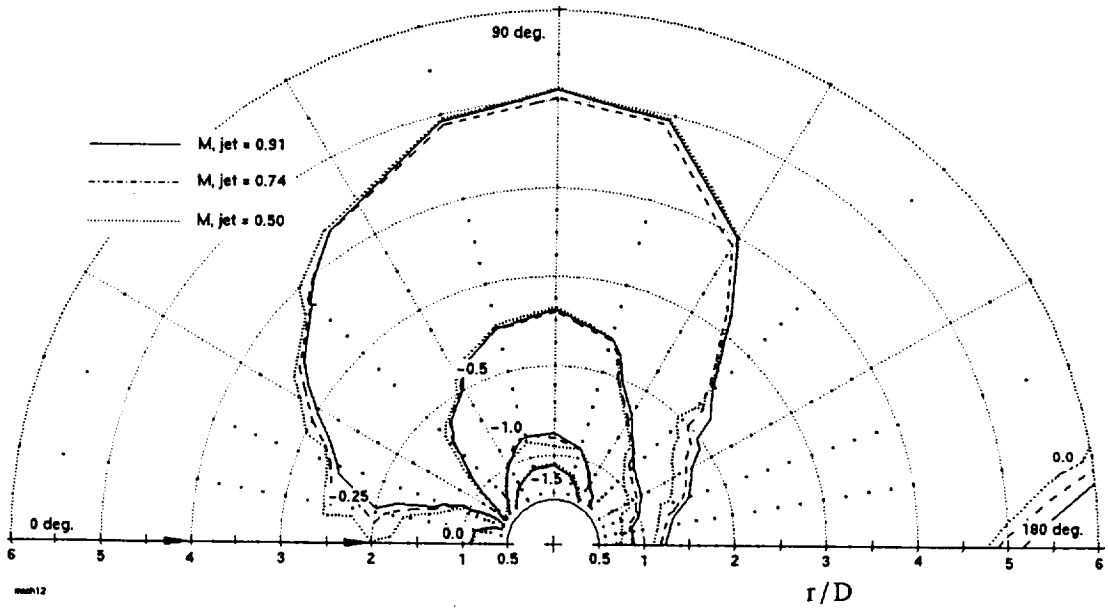

Figure 3.13. Effect of jet Mach number on pressure distribution at R = 12.1.

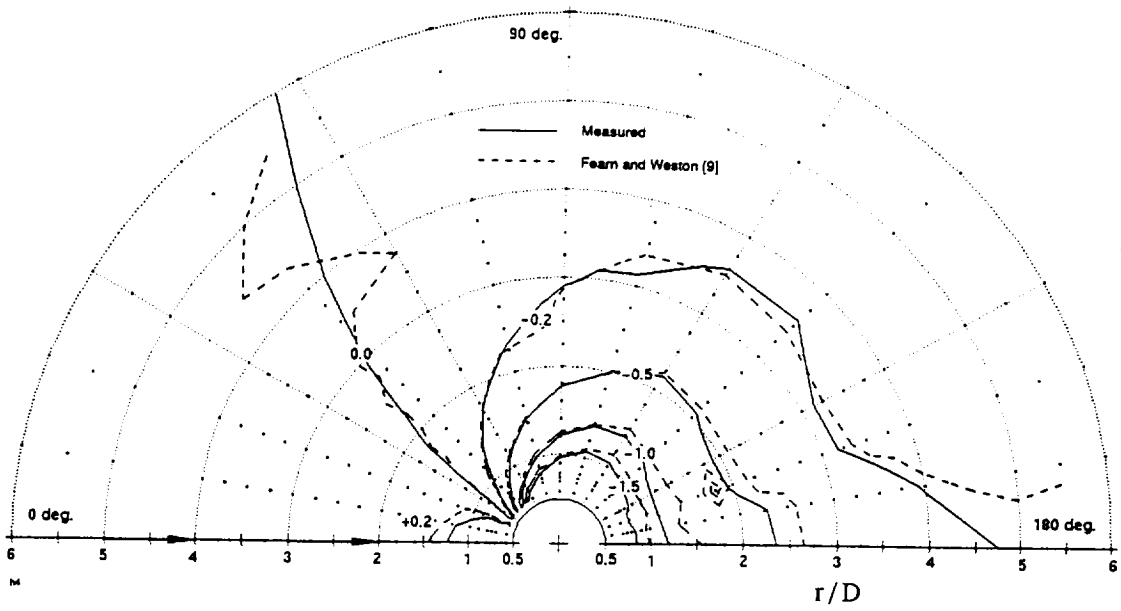

Figure 3.14. Comparison of measured induced pressure coefficient at R = 4.0 and M_j = 0.74 with prior experiment.

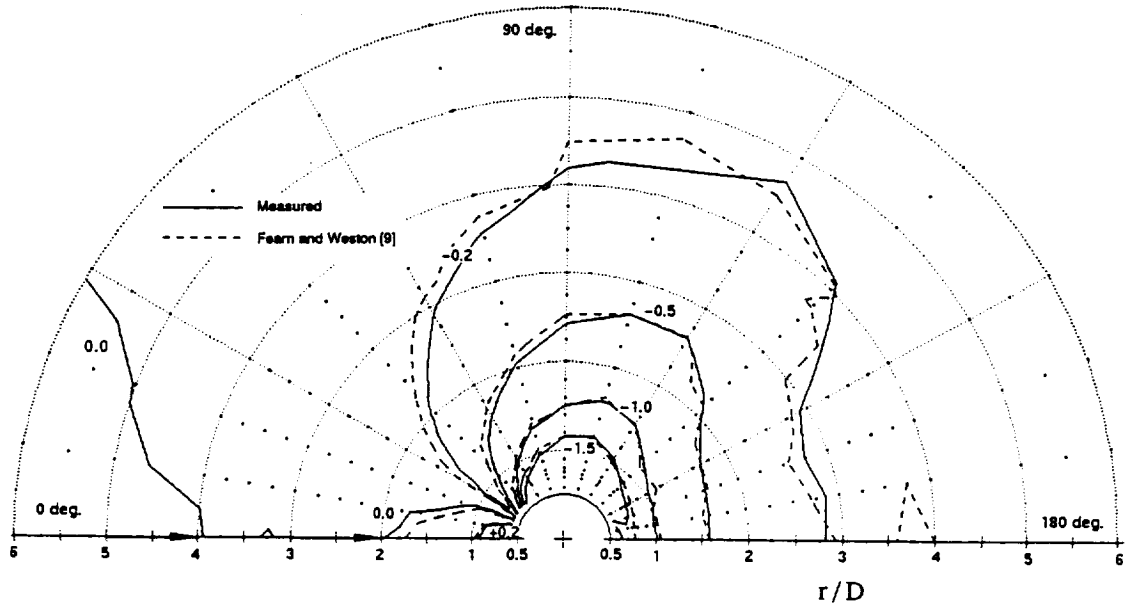

Figure 3.15. Comparison of measured induced pressure coefficient at R = 6.0 and M_j = 0.91 with prior experiment.

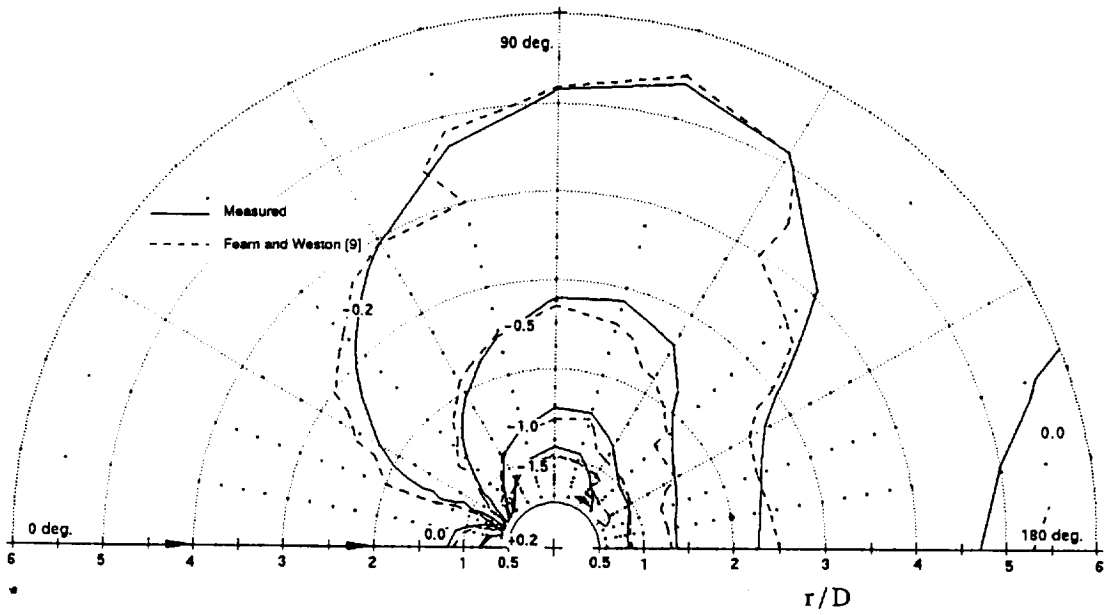

Figure 3.16. Comparison of measured induced pressure coefficient at R = 8.0 and $M_j = 0.91$ with prior experiment.

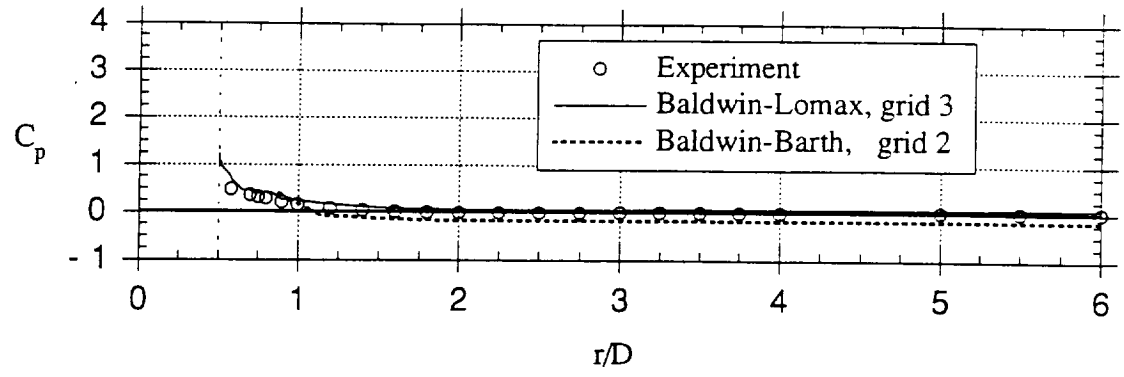

(a) 0° azimuth

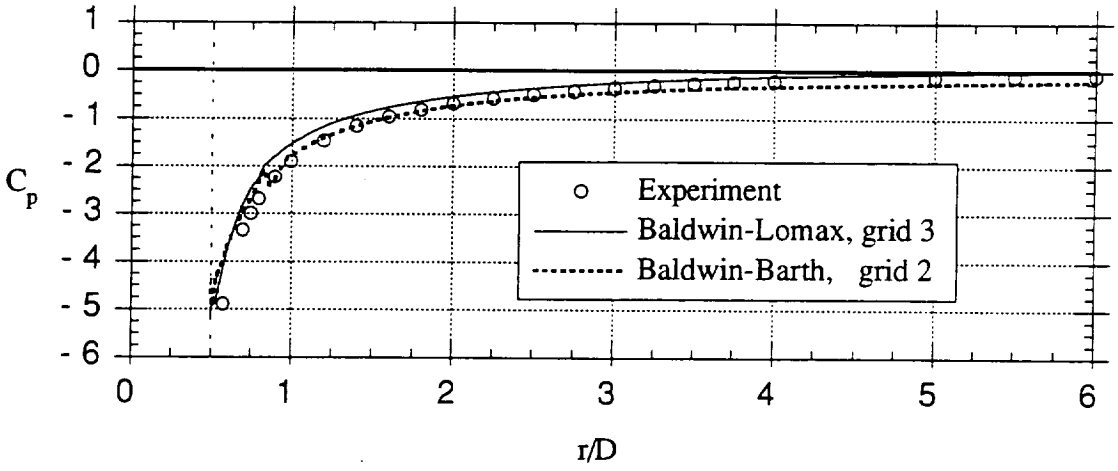

(b) 90° azimuth

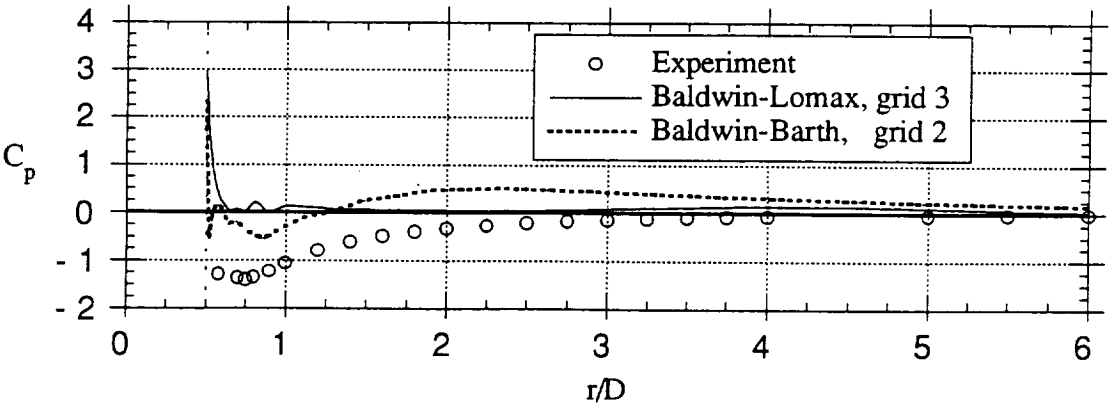

(c) 180° azimuth

Figure 3.17. Comparison of measured induced pressure coefficient at R = 6 and M_j = 0.91 with CFD solutions.

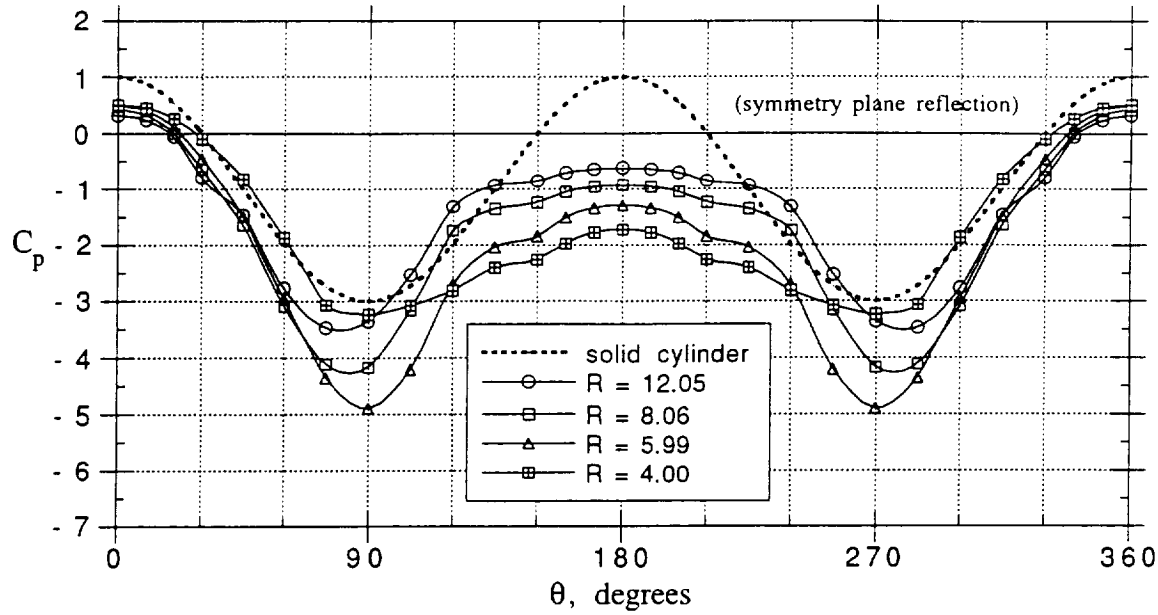

Figure 3.18. Induced pressure coefficientnear jet exit (r/D = 0.58) at various velocity ratios compared with inviscid flow theory for a 2-D solid cylinder.

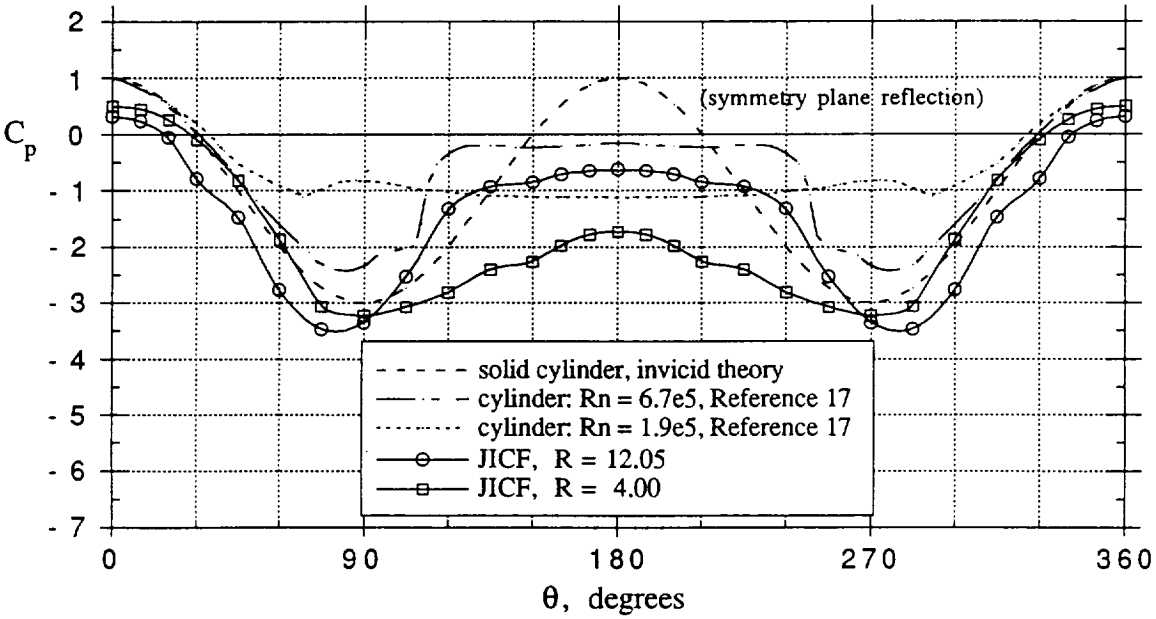

Figure 3.19. Induced pressure coefficient near jet exit (r/D = 0.58) at R = 12 and 4 compared with 2-D solid cylinder experiment.

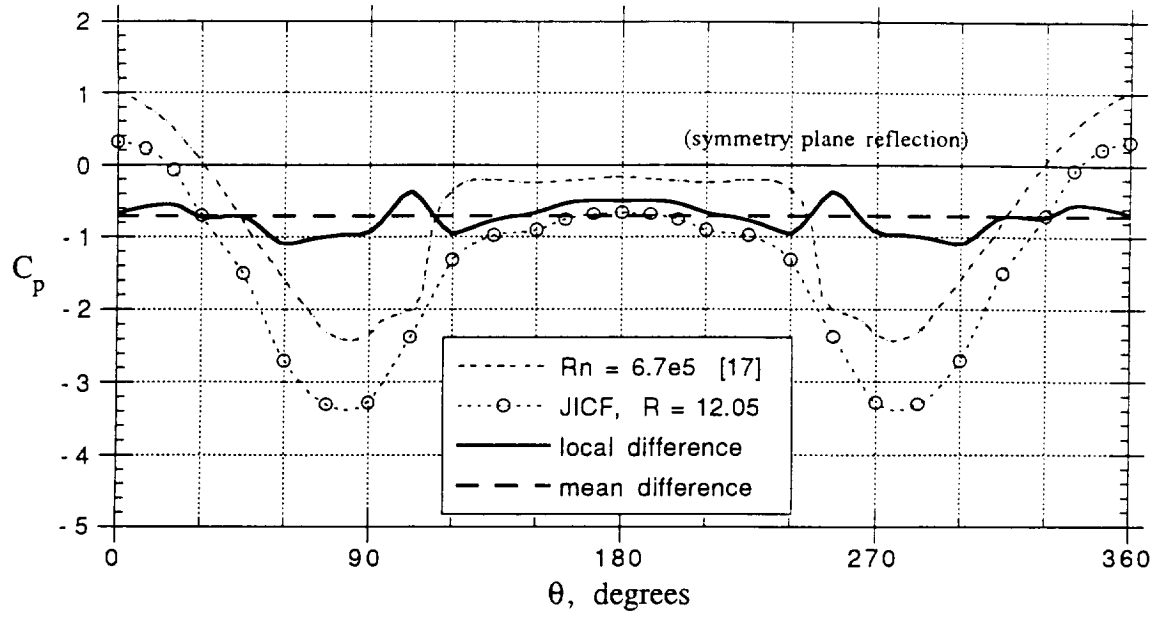

Figure 3.20. Difference between jet induced C_p near jet exit (r/D = 0.58) at R = 12 and experimental values for 2-D solid cylinder.

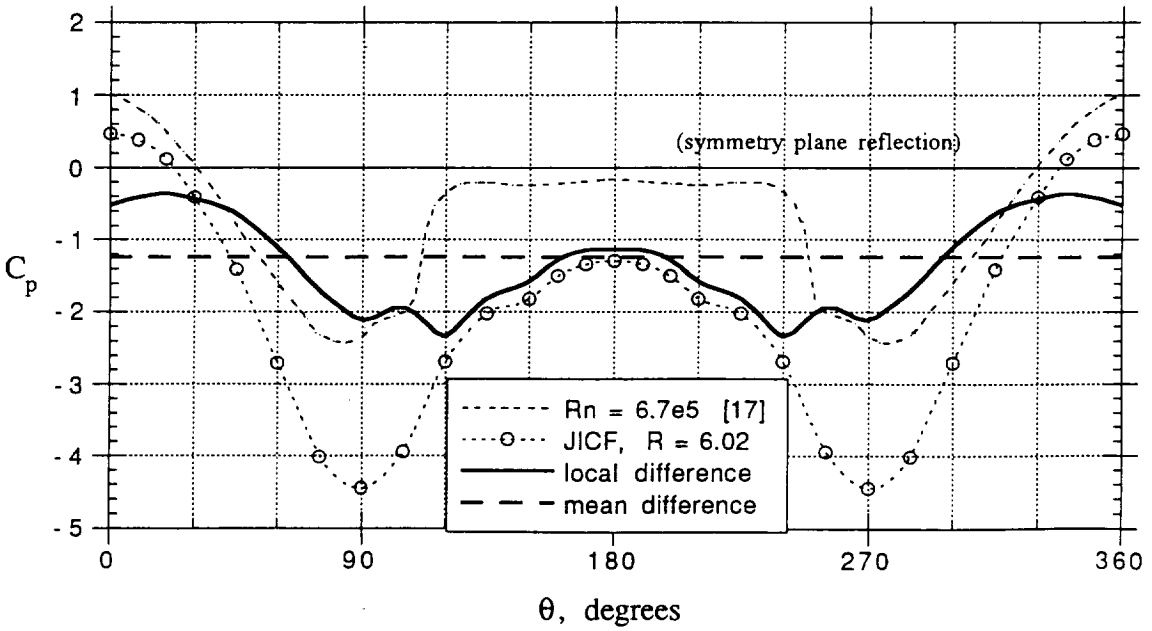

Figure 3.21. Difference between jet induced C_p near jet exit (r/D = 0.58) at R = 6 and experimental values for 2-D solid cylinder.

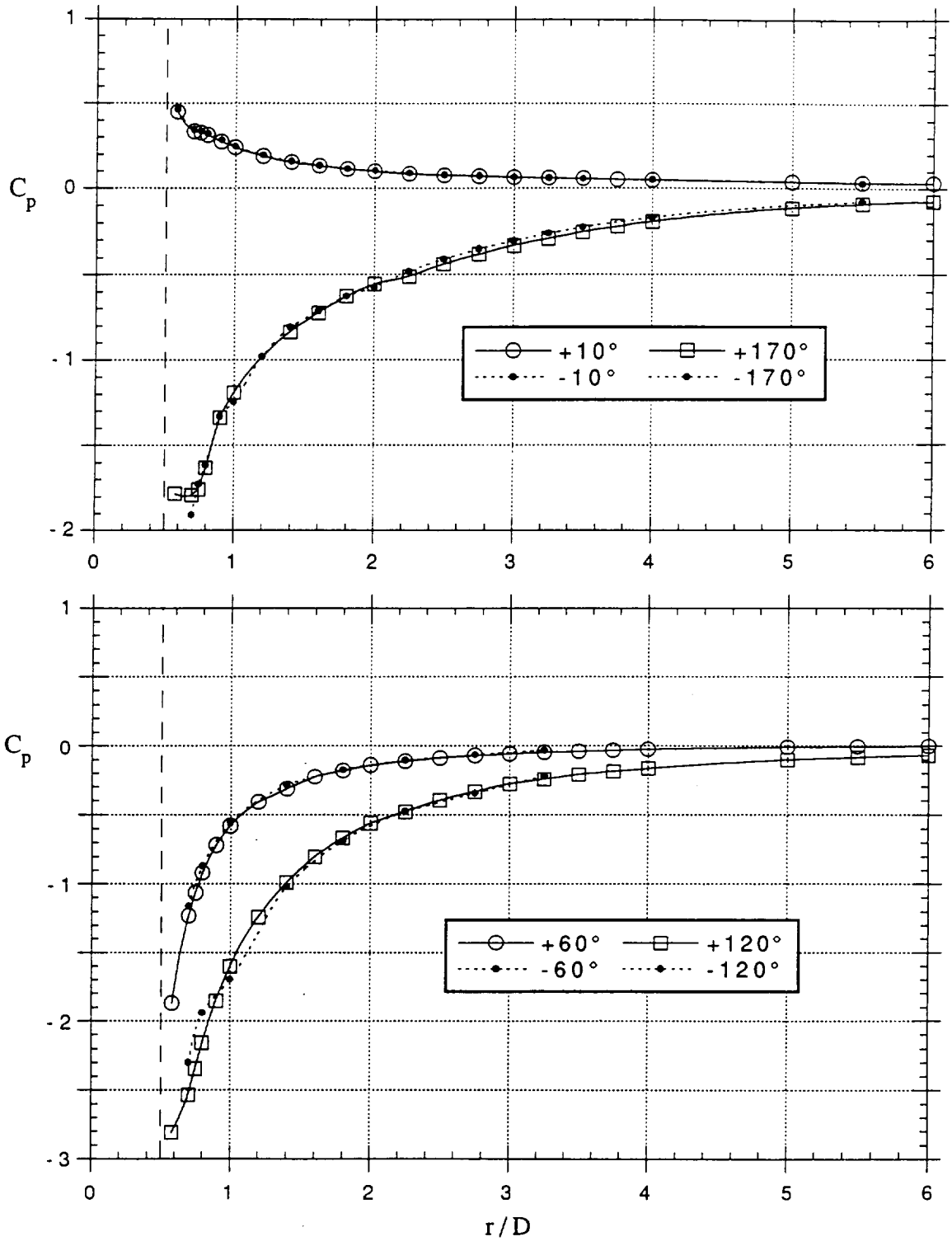

Figure 3.22. Symmetry plane comparison of induced pressure distribution from ± 10° to ± 170° at R = 4.0 and M_j = 0.74.

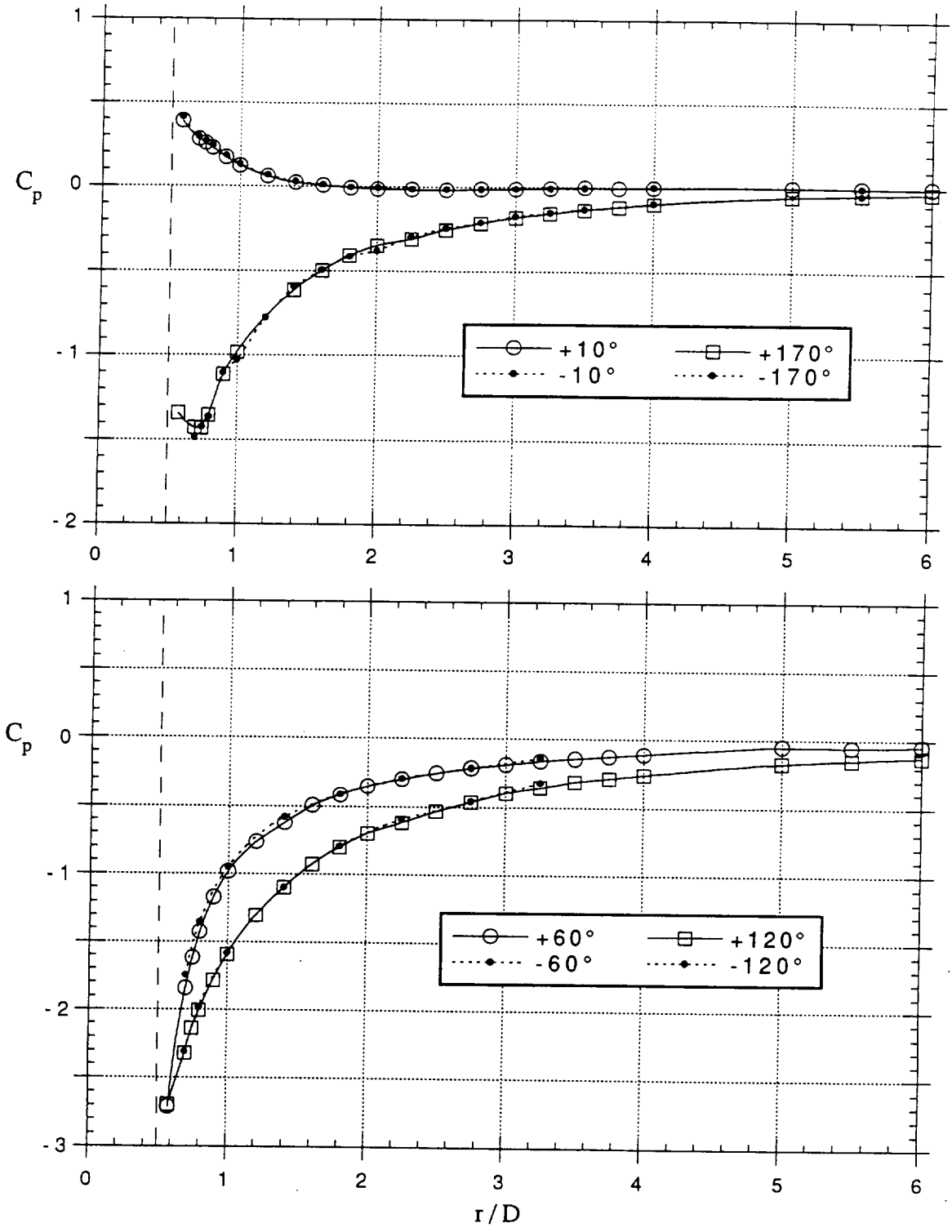

Figure 3.23. Symmetry plane comparison of induced pressure distribution from ± 10° to ± 170° at R = 6.0 and M_j = 0.91.

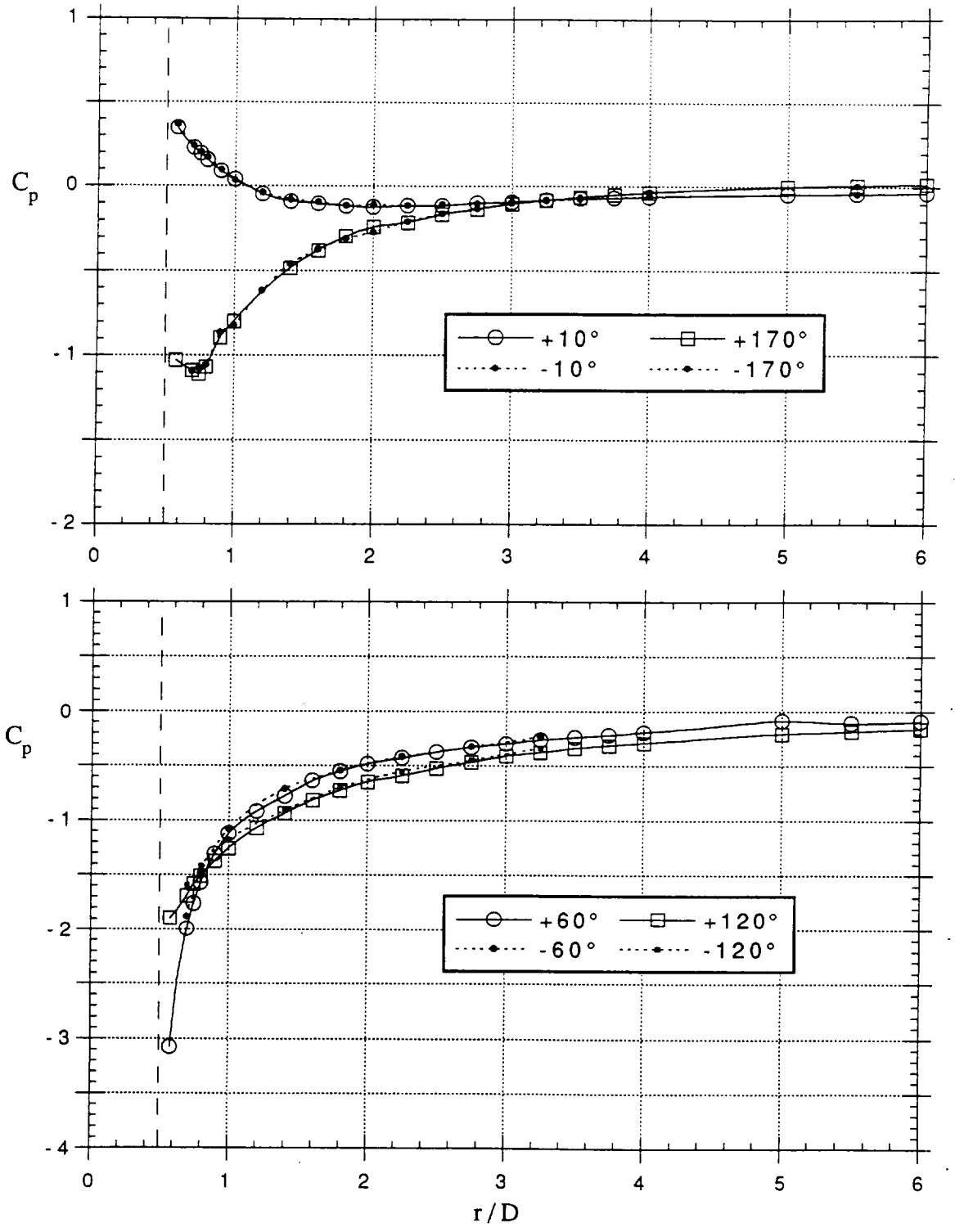

Figure 3.24. Symmetry plane comparison of induced pressure distribution from ± 10° to ± 170° at R = 8.0 and M_j = 0.91.

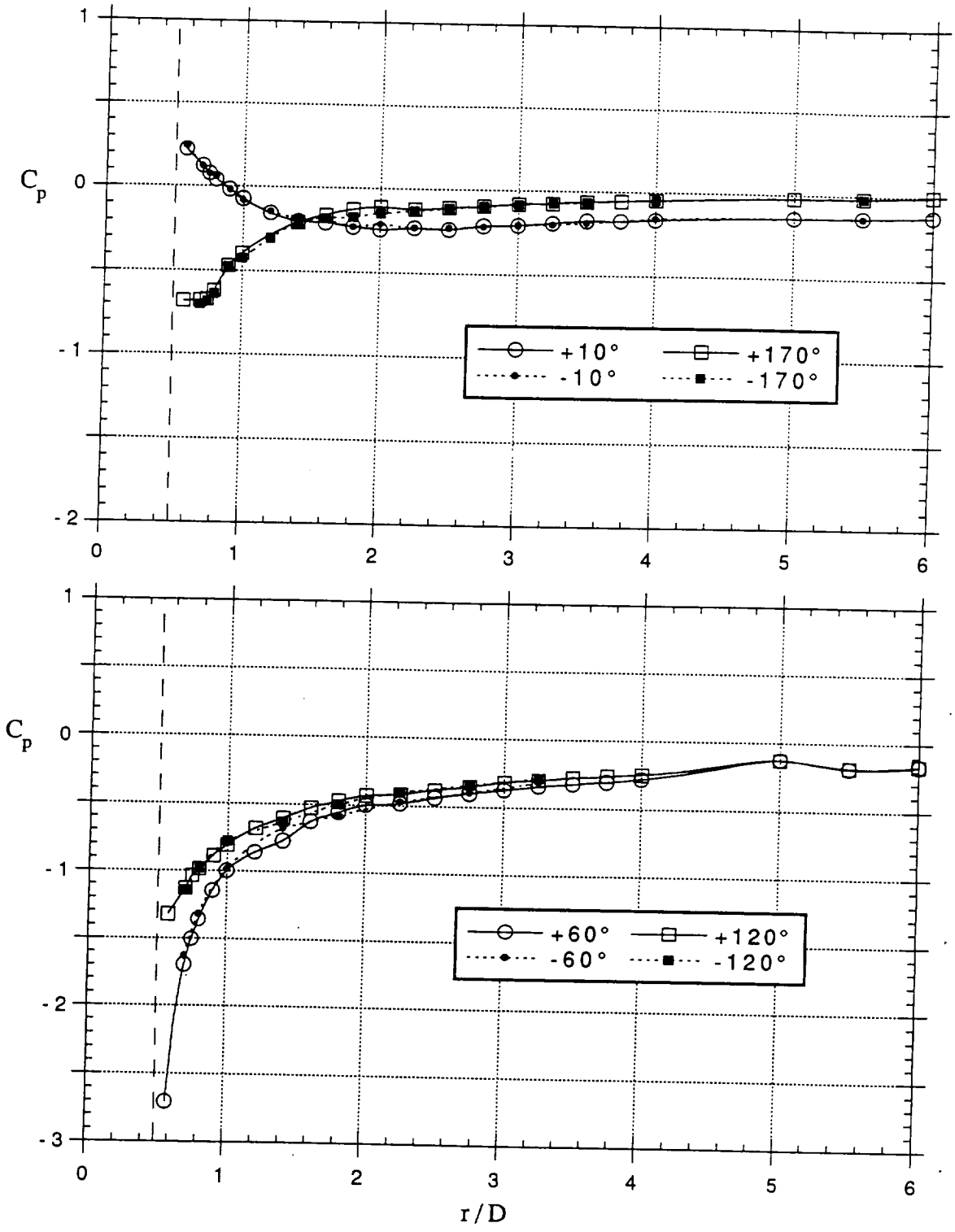

Figure 3.25. Symmetry plane comparison of induced pressure distribution from ± 10° to ± 170° at R = 12.1 and M_j = 0.91.

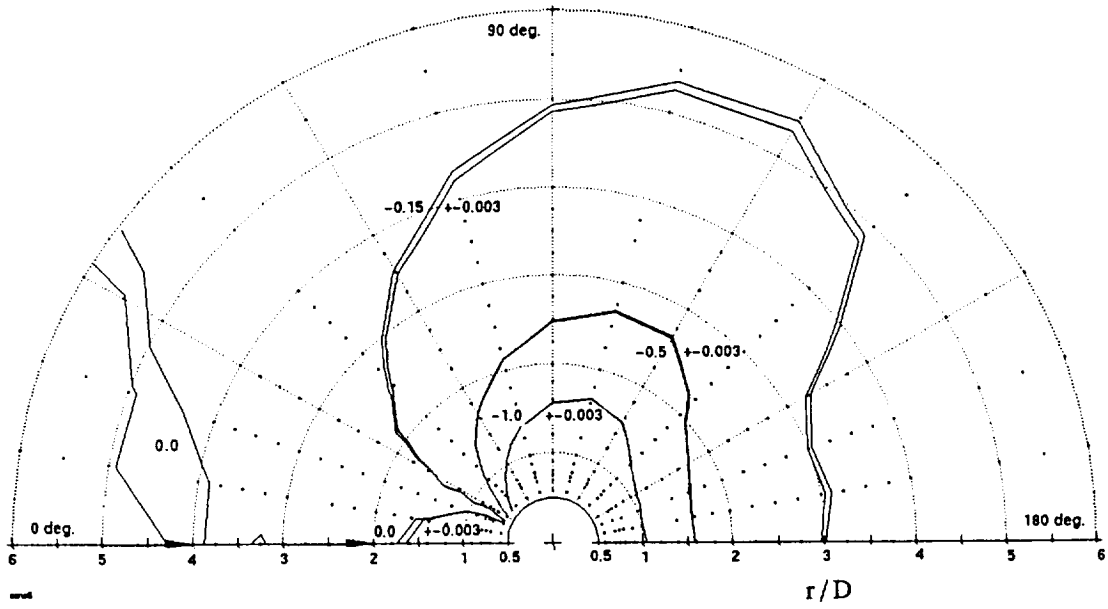

Figure 3.26. Pressure contour transducer error band ($\Delta Cp = \pm 0.003$) at R = 6.0 and $M_j = 0.91$.

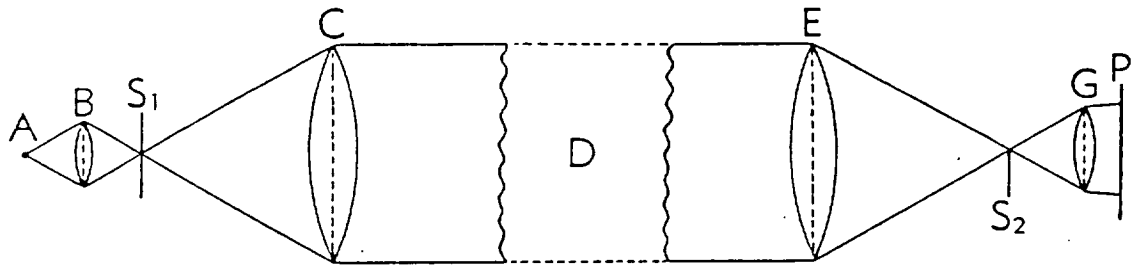

Figure 4.1. Diagram of simple schlieren system.

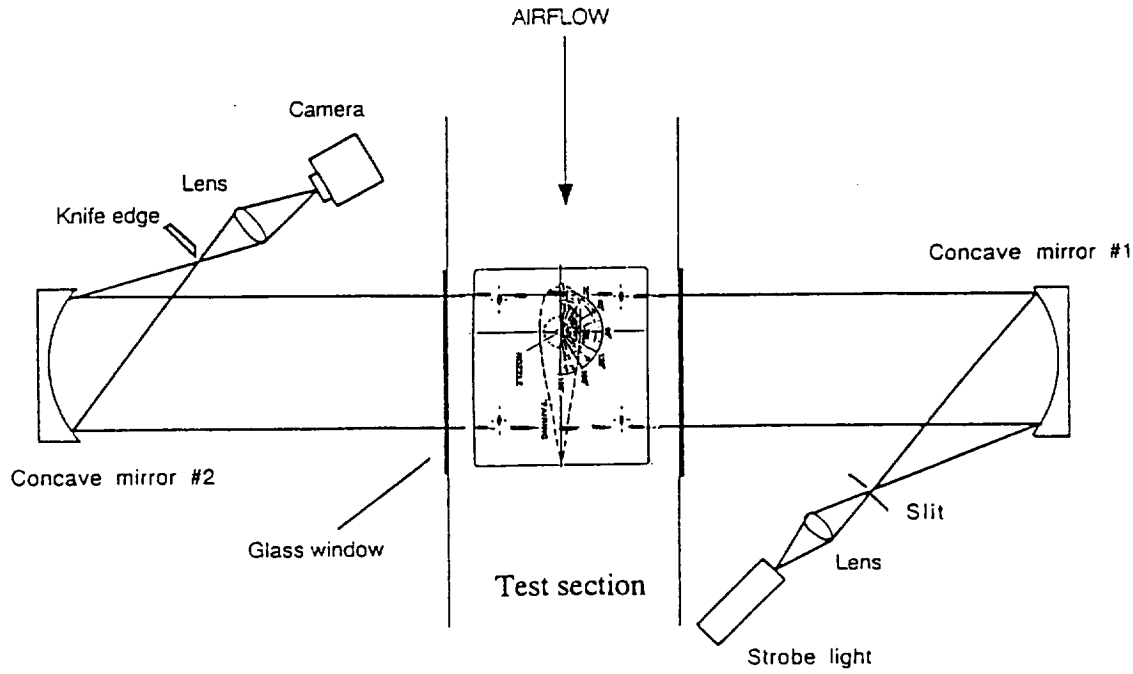

Figure 4.2. Diagram of schlieren system (not to scale)
for 7x10 ft Wind Tunnel No. 1.

Figure 4.3. Schlieren photograph of jet plume at R = 4.65 and M_j = 0.95.

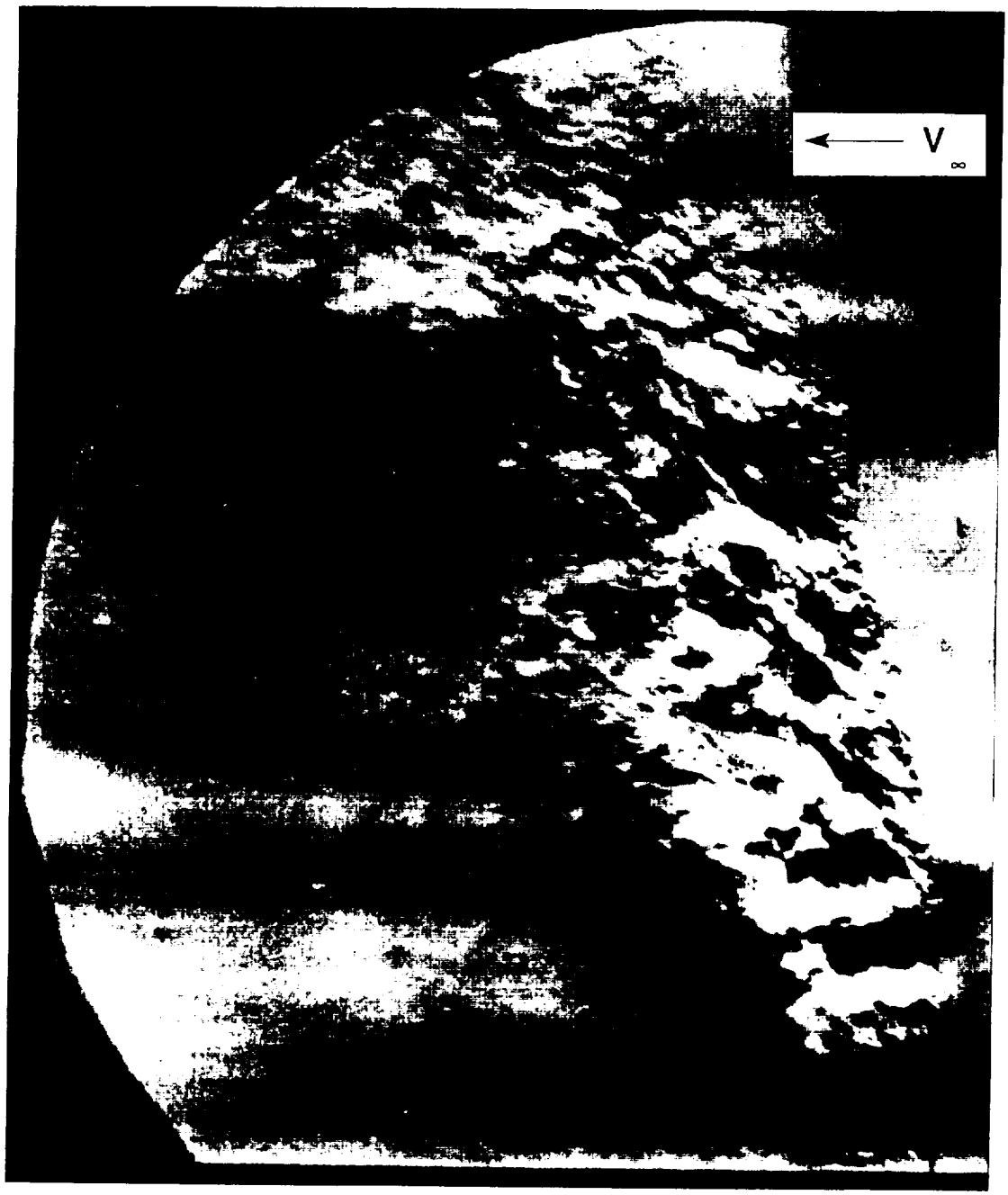

Figure 4.4. Schlieren photograph of jet plume at R = 6.49 and M_j = 0.94.

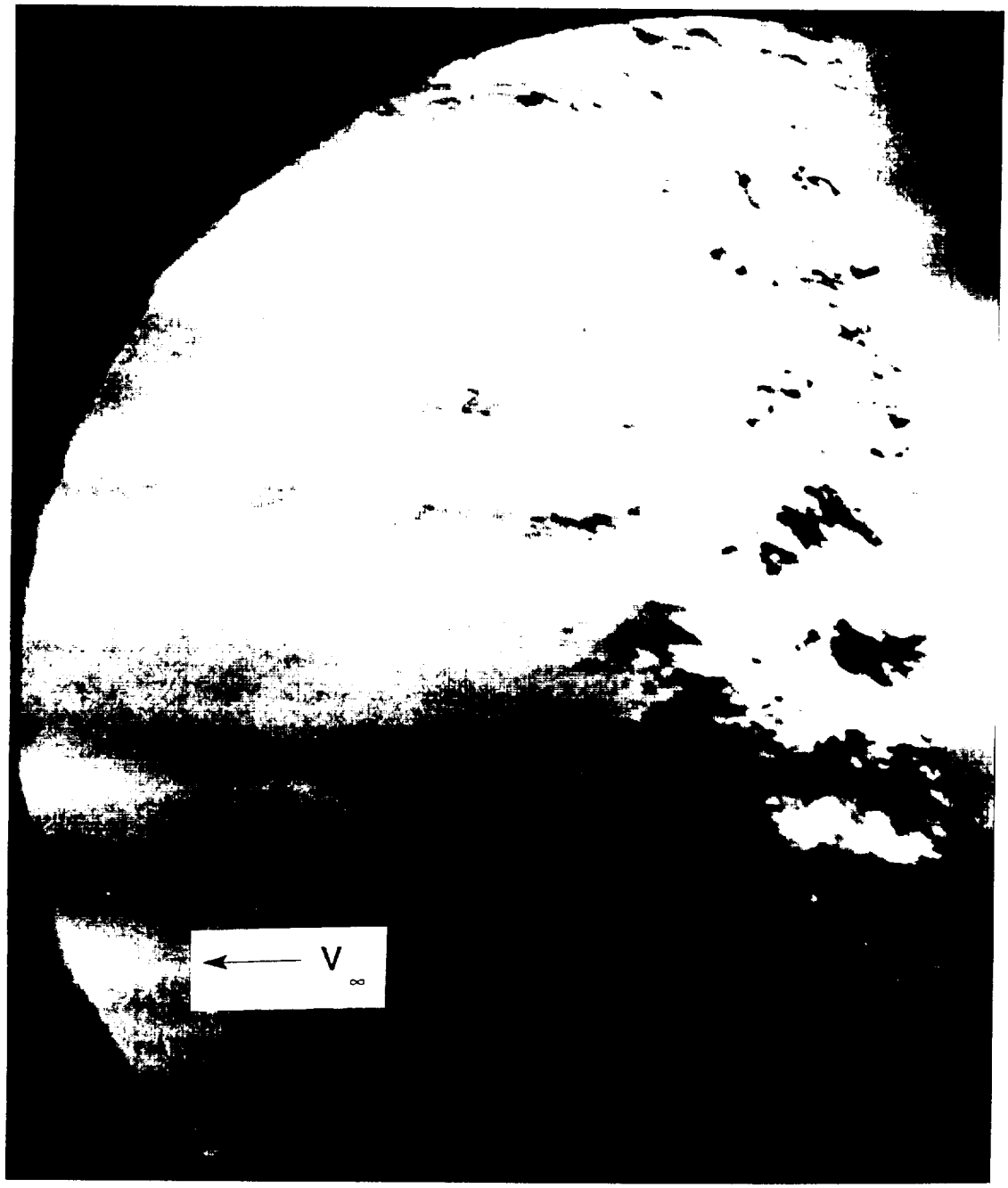

Figure 4.5. Schlieren photograph of jet plume at R = 12.82 and M_j = 0.93.

Figure 4.6. Schlieren photograph of jet plume without crossflow at $M_j = 0.94$.

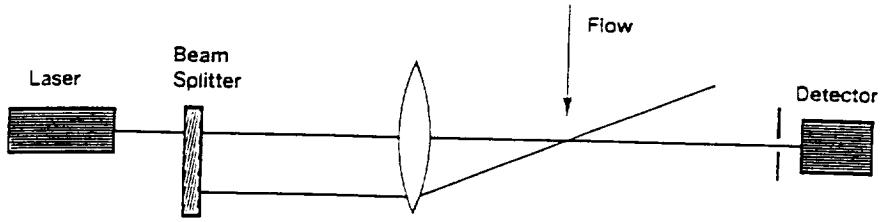

Figure 5.1. Reference beam or heterodyne LDV system.

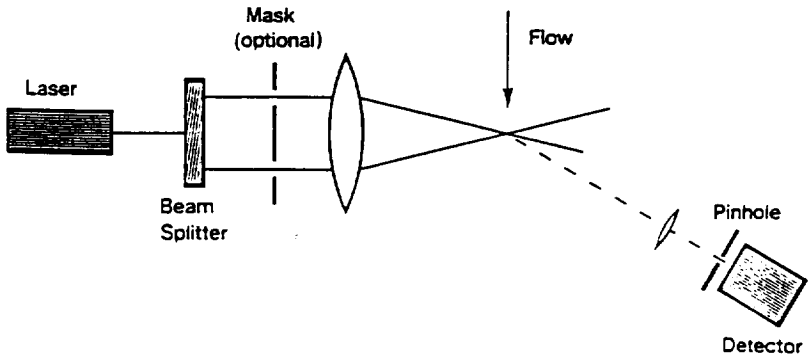

Figure 5.2. Real fringe LDV system (forward-scatter).

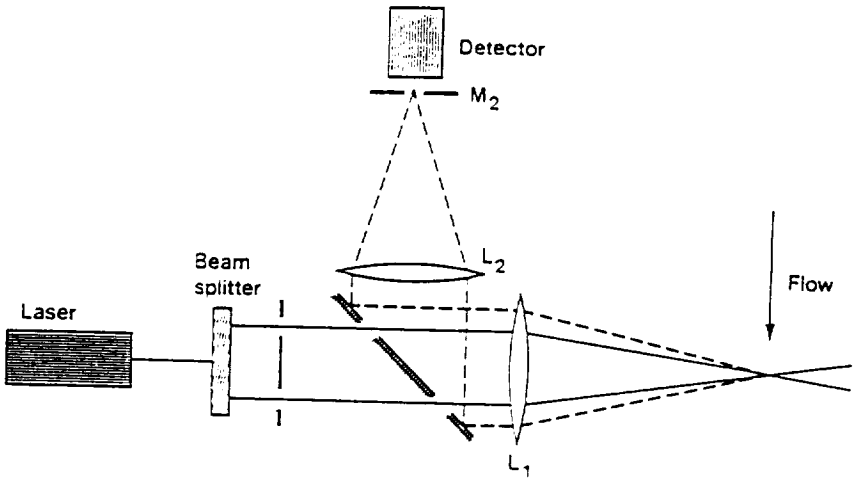

Figure 5.3. Real fringe LDV system (back-scatter).

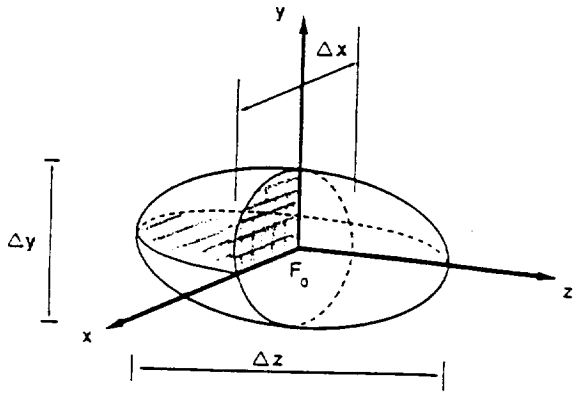

Figure 5.4. 3-D orthogonal measuring volume (not to scale).

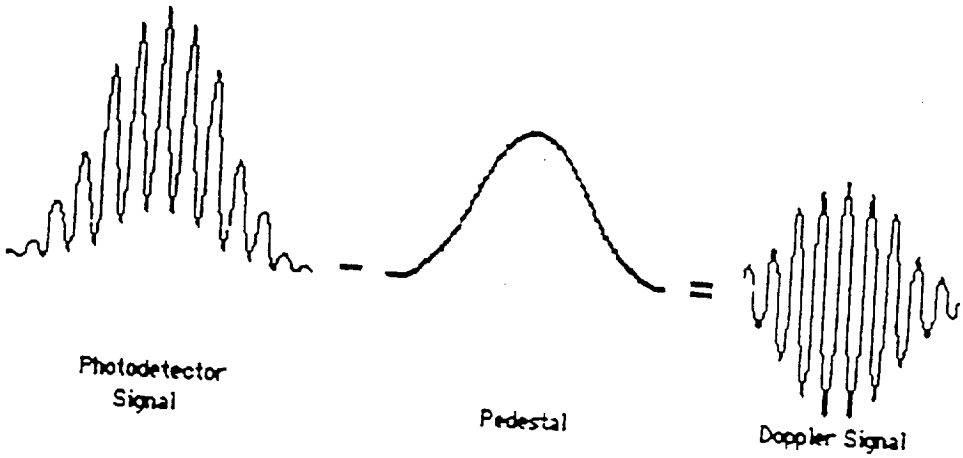

Figure 5.5. Doppler signal filtering.

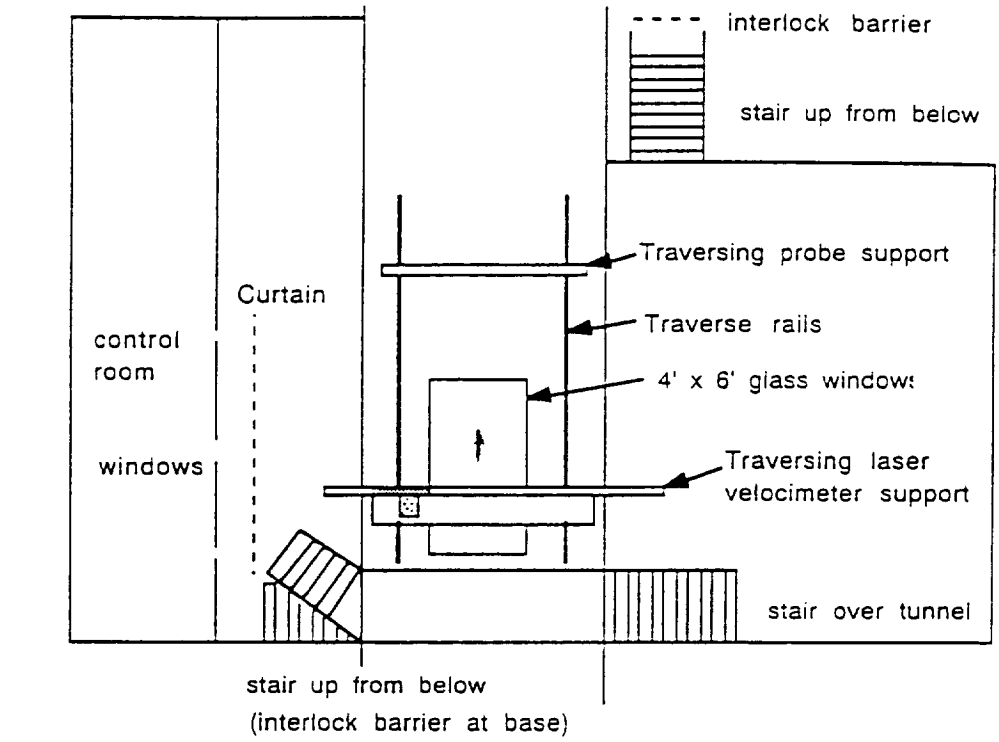

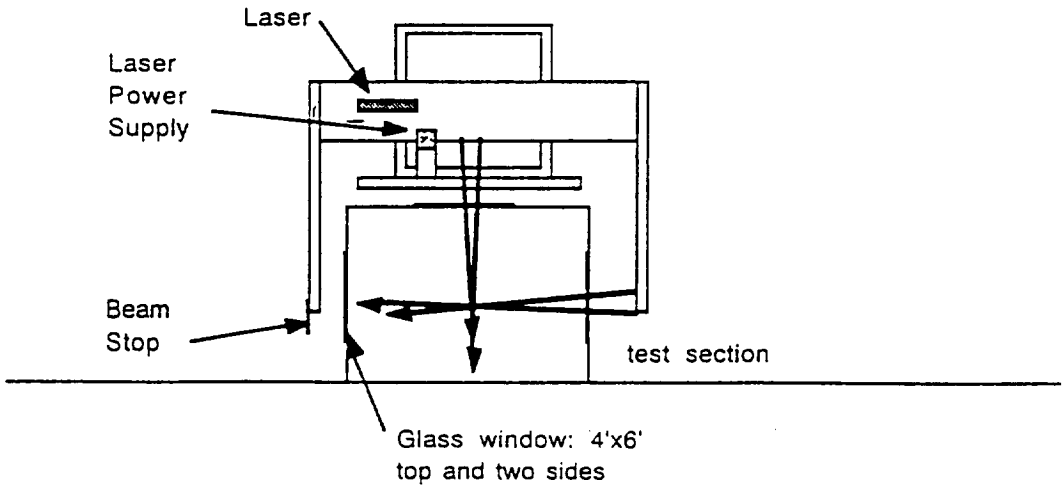

Figure 5.6. Layout of LDV system and test section.

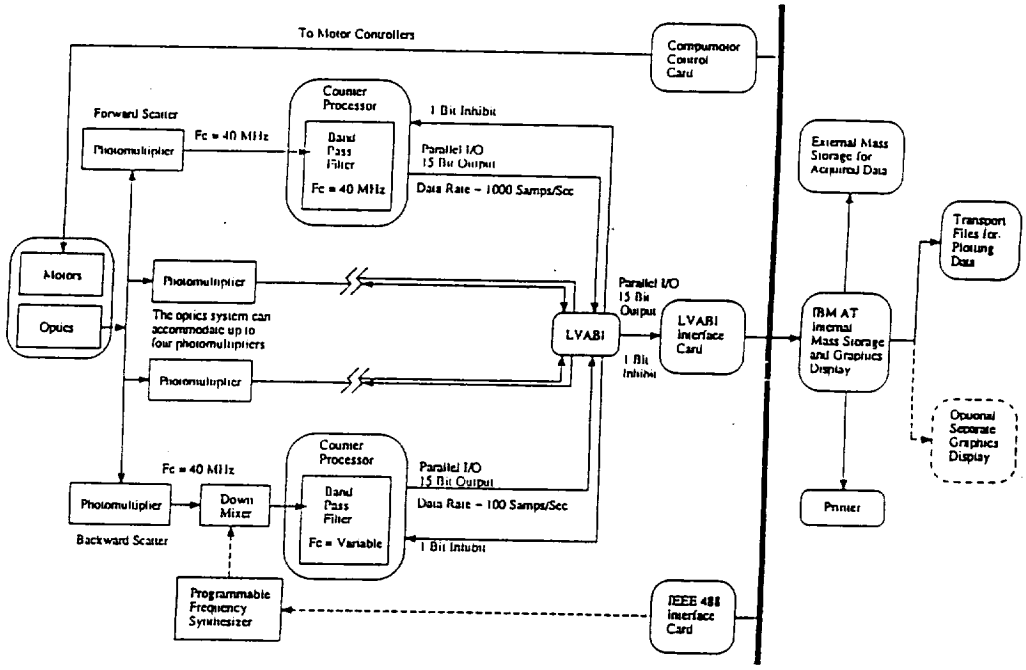

Figure 5.7. Signal processing and data acquisition system.

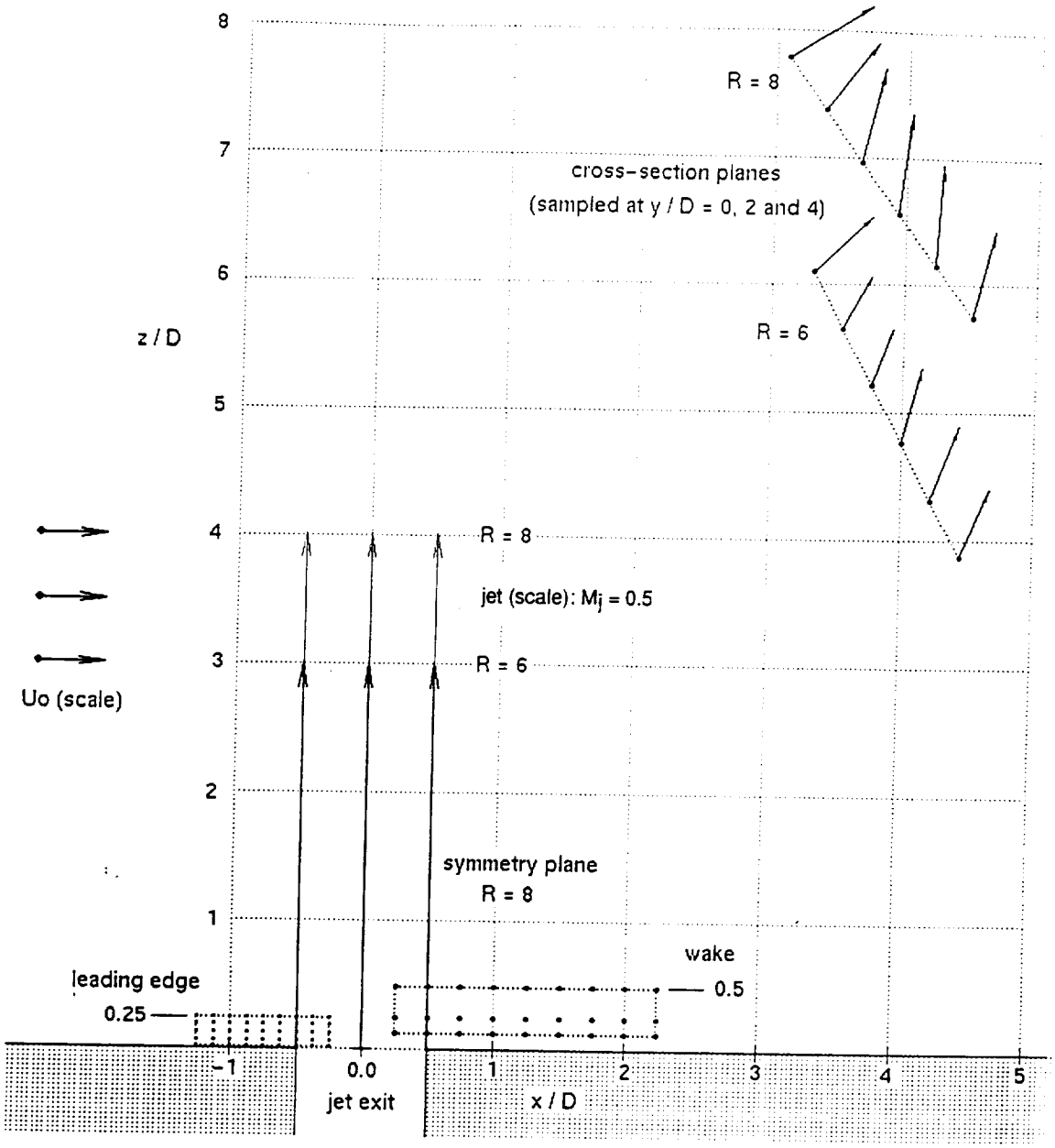

Figure 5.8. Jet flowfield regions for LDV measurements at R = 6 (V_∞ = 98 fps) and R = 8 (V_∞ = 73 fps).

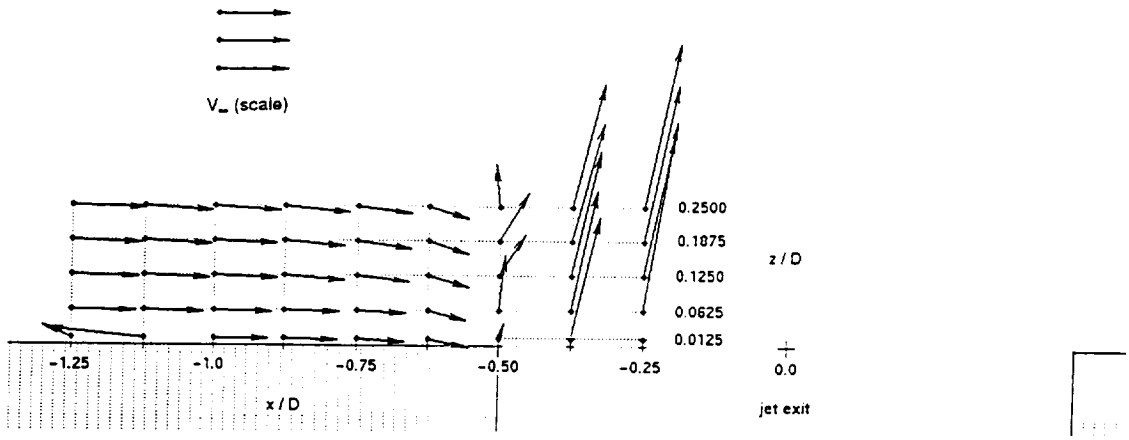

Figure 5.9. Velocity vectors in symmetry plane near jet leading edge at R = 8 and M_j = 0.5.

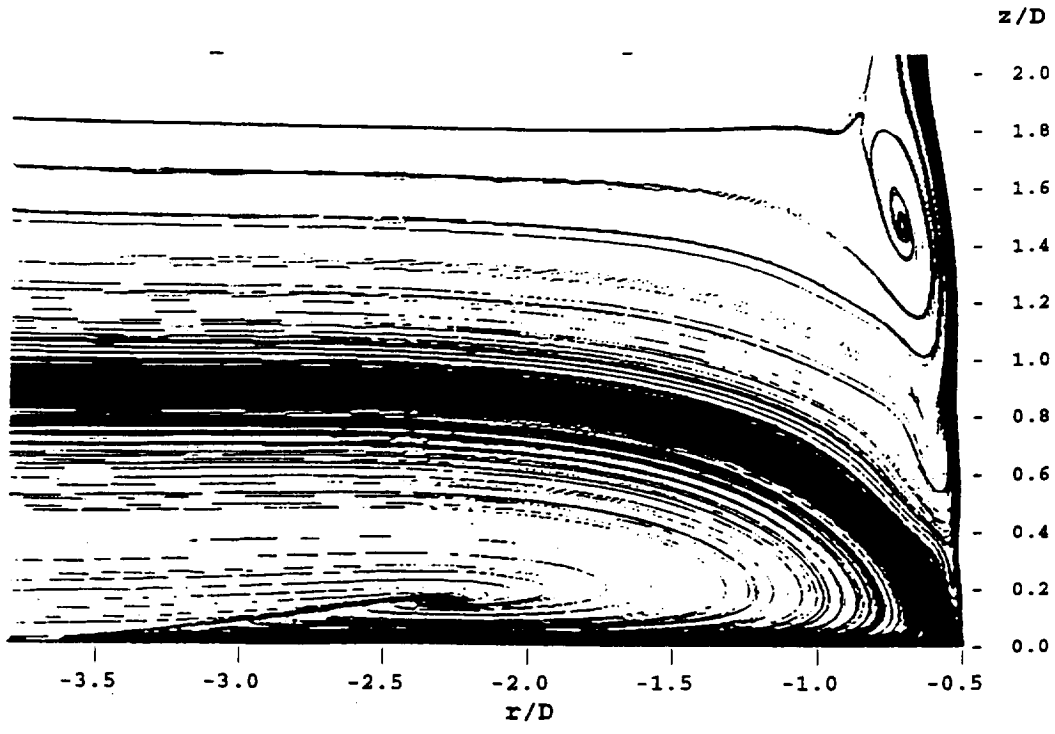

Figure 5.10. CFD solutions of flow in symmetry plane at jet leading edge.

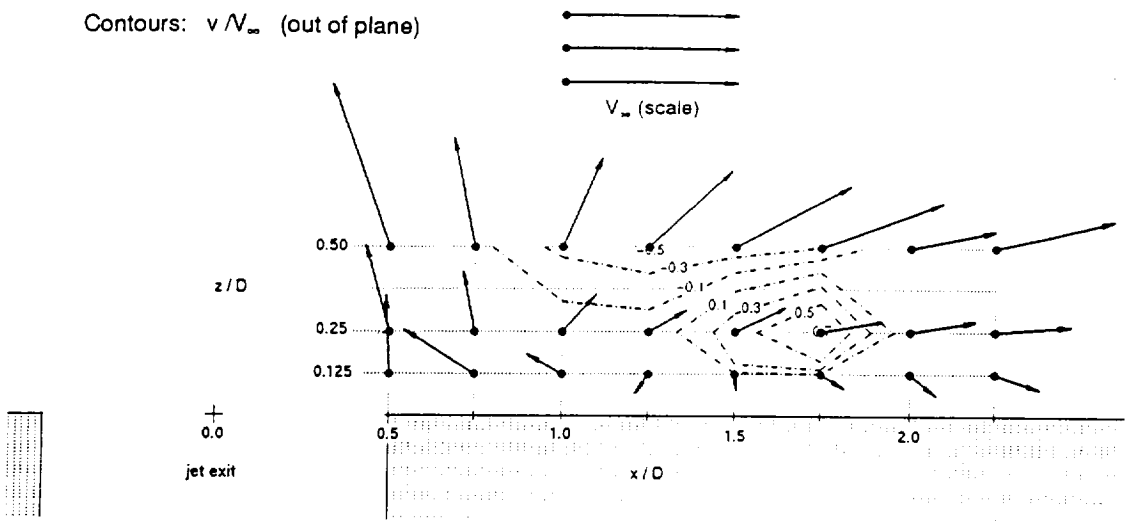

Figure 5.11. Velocity vectors and contours in symmetry plane in jet wake at R = 8 and M_j = 0.5.

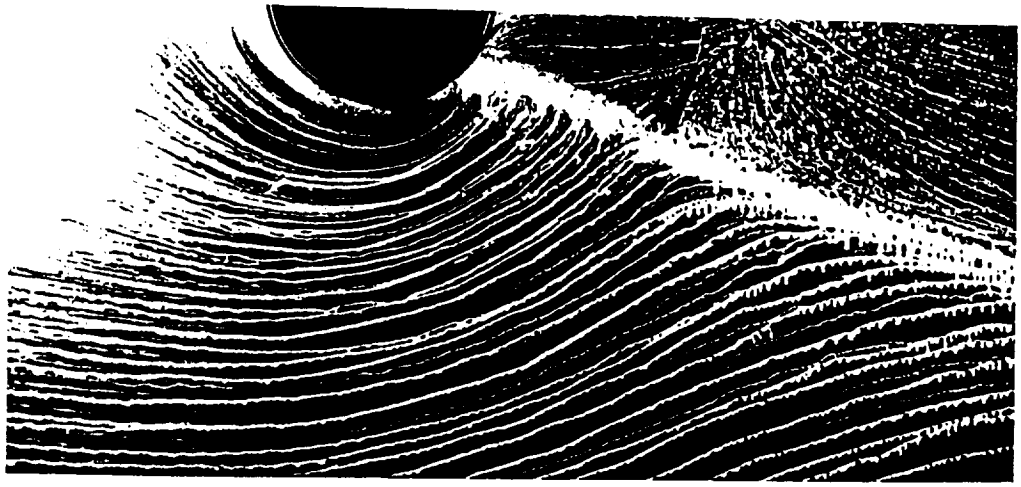

Figure 5.12. Oil flow photograph in jet wake from prior experiment at R = 5.5.

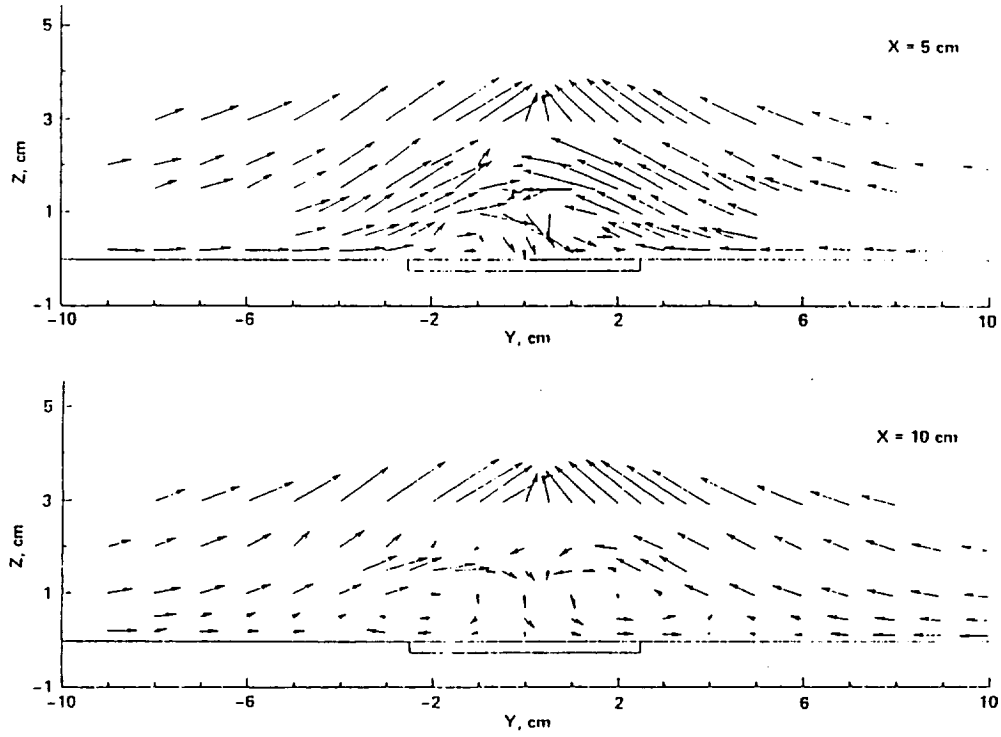

Figure 5.13. Cross sections in jet wake from prior experiment.

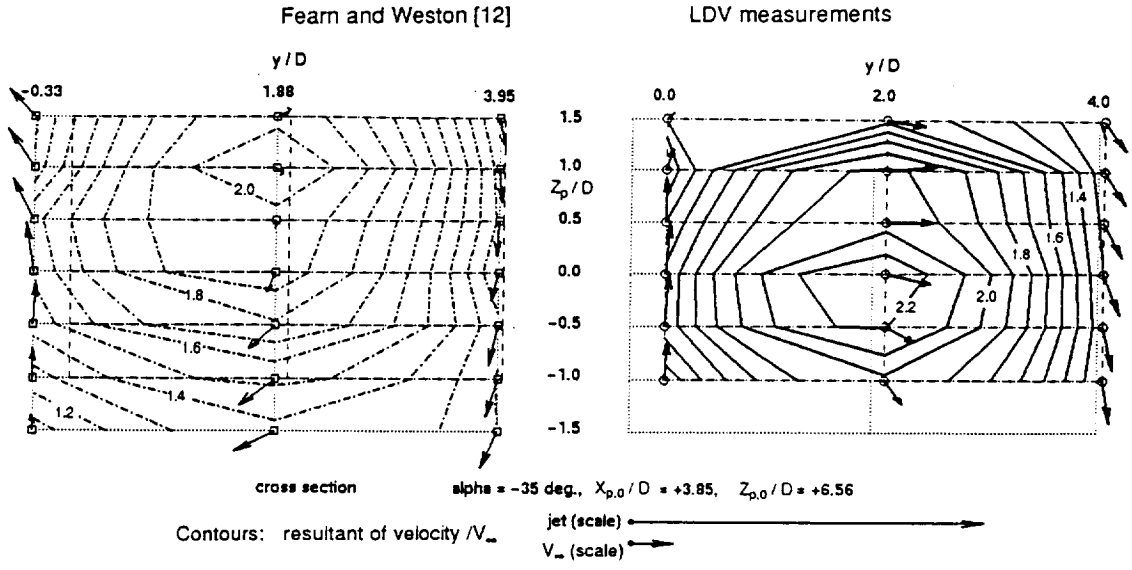

Figure 5.14. Comparison of measured jet plume cross sections at R = 8 and M_j = 0.5 with prior experiment.

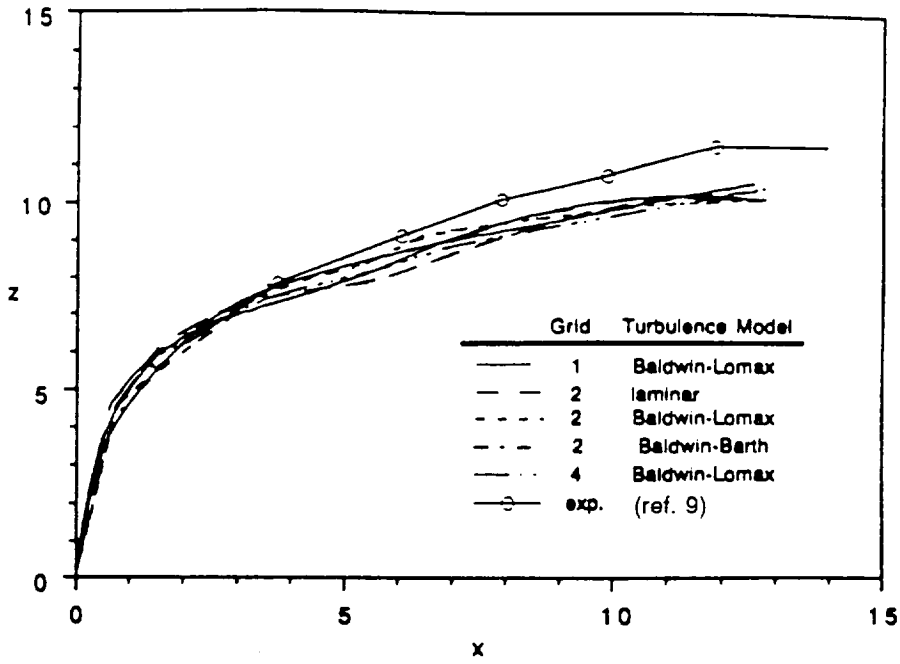

Figure 5.15. Comparison of CFD and experimental jet centerline paths.

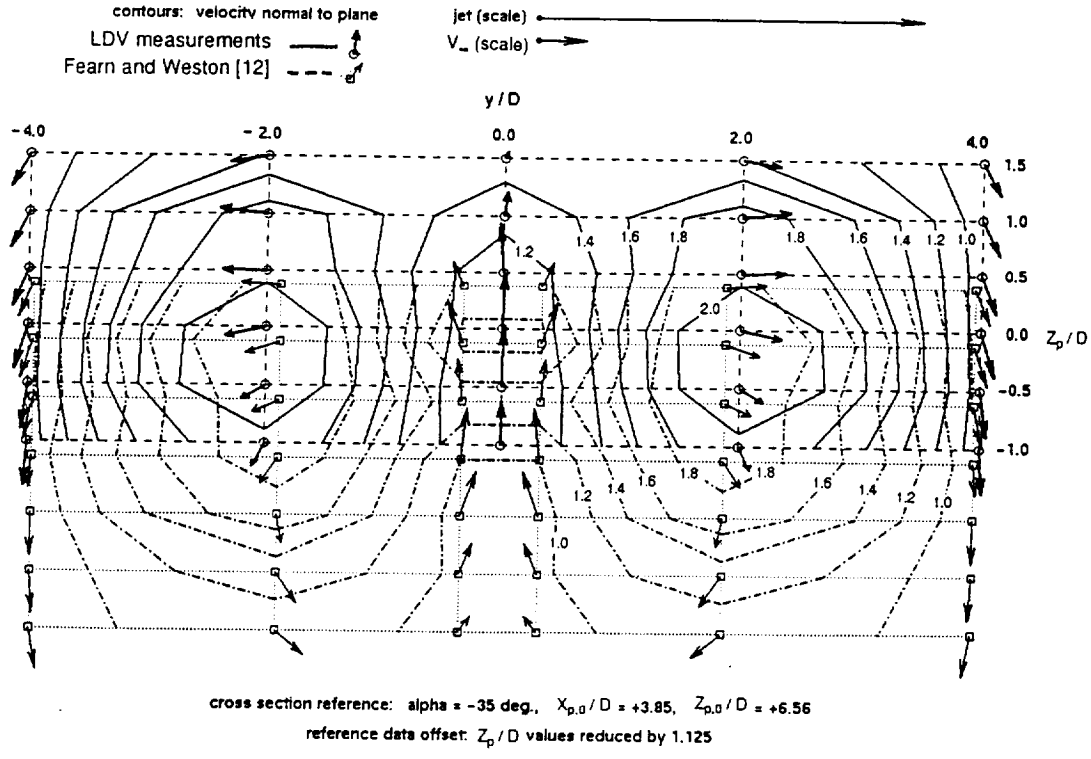

Figure 5.16. Comparison of offset prior experiment jet plume cross section with measured cross section at R = 8.

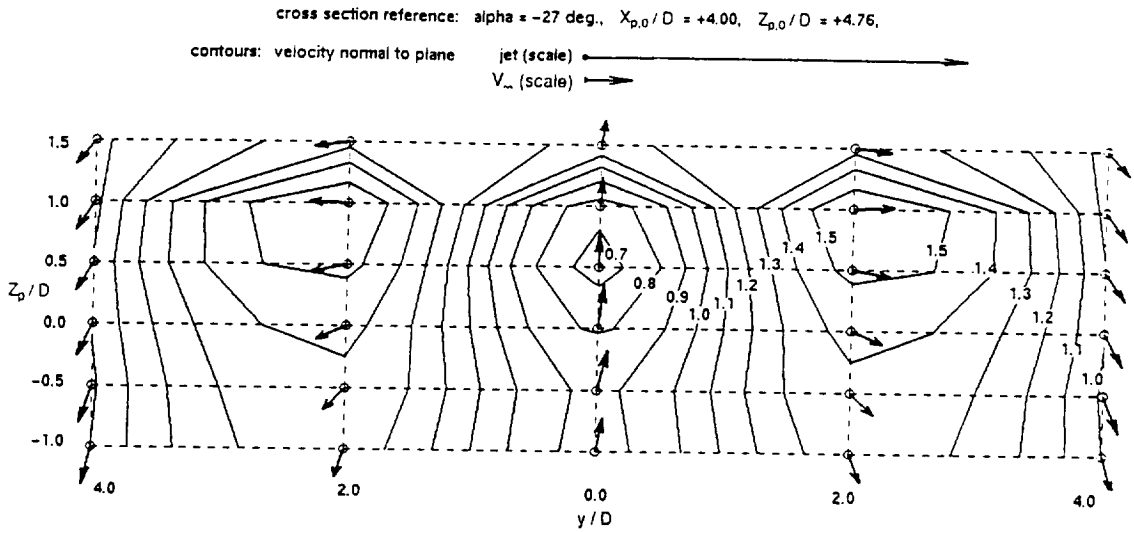

Figure 5.17. Measured jet plume cross sections at R = 6 and M_j = 0.5.

Table 3.1 Pressure port locations and transducer range limits

Angle \ r/D	0.58	0.70	0.75	0.80	0.90	1.00	1.20	1.40	1.60	1.80	2.00
0	20 inch	20 inch	20 inch	20 inch	20 inch	20 inch	20 inch	20 inch	20 inch	20 inch	20 inch
10	20 inch	20 inch	20 inch	20 inch	20 inch	20 inch	20 inch	20 inch	20 inch	20 inch	20 inch
20	20 inch	20 inch	20 inch	20 inch	20 inch	20 inch	20 inch	20 inch	20 inch	20 inch	20 inch
30	20 inch	20 inch	20 inch	20 inch	20 inch	20 inch	20 inch	20 inch	20 inch	20 inch	20 inch
45	20 inch	20 inch	20 inch	20 inch	20 inch	20 inch	20 inch	20 inch	20 inch	20 inch	20 inch
60	2.5 psi	20 inch	20 inch	20 inch	20 inch	20 inch	20 inch	20 inch	20 inch	20 inch	20 inch
75	2.5 psi	20 inch	20 inch	20 inch	20 inch	20 inch	20 inch	20 inch	20 inch	20 inch	20 inch
90	2.5 psi	20 inch	20 inch	20 inch	20 inch	20 inch	20 inch	20 inch	20 inch	20 inch	20 inch
105	2.5 psi	20 inch	20 inch	20 inch	20 inch	20 inch	20 inch	20 inch	20 inch	20 inch	20 inch
120	20 inch	20 inch	20 inch	20 inch	20 inch	20 inch	20 inch	20 inch	20 inch	20 inch	20 inch
135	20 inch	20 inch	20 inch	20 inch	20 inch	20 inch	20 inch	20 inch	20 inch	20 inch	20 inch
150	20 inch	20 inch	20 inch	20 inch	20 inch	20 inch	20 inch	20 inch	20 inch	20 inch	20 inch
160	20 inch	20 inch	20 inch	20 inch	20 inch	20 inch	20 inch	20 inch	20 inch	20 inch	20 inch
170	20 inch	20 inch	20 inch	20 inch	20 inch	20 inch	20 inch	20 inch	20 inch	20 inch	20 inch
180	20 inch	20 inch	20 inch	20 inch	20 inch	20 inch	20 inch	20 inch	20 inch	20 inch	20 inch
-170	20 inch	20 inch	20 inch	20 inch	20 inch	20 inch	20 inch	20 inch	20 inch	20 inch	20 inch
-120		20 inch		20 inch		20 inch		20 inch		20 inch	
-90		2.5 psi		20 inch		20 inch		20 inch		20 inch	
-60		2.5 psi		20 inch		20 inch		20 inch		20 inch	
-30		20 inch		20 inch		20 inch		20 inch		20 inch	
-10	20 inch	20 inch	20 inch	20 inch	20 inch	20 inch	20 inch	20 inch	20 inch	20 inch	20 inch

Angle \ r/D	2.25	2.50	2.75	3.00	3.25	3.50	3.75	4.00	5.00	5.50	6.00
0	10 inch	10 inch	10 inch	10 inch	10 inch	10 inch	10 inch	10 inch	10 inch	10 inch	10 inch
10	10 inch	10 inch	10 inch	10 inch	10 inch	10 inch	10 inch	10 inch	10 inch	10 inch	10 inch
20	10 inch	10 inch	10 inch	10 inch	10 inch	10 inch	10 inch	10 inch	10 inch	10 inch	10 inch
30	10 inch	10 inch	10 inch	10 inch	10 inch	10 inch	10 inch	10 inch	10 inch	10 inch	10 inch
45	10 inch	10 inch	10 inch	10 inch	10 inch	10 inch	10 inch	10 inch	10 inch	10 inch	10 inch
60	10 inch	10 inch	10 inch	10 inch	10 inch	10 inch	10 inch	10 inch	10 inch	10 inch	10 inch
75	10 inch	10 inch	10 inch	10 inch	10 inch	10 inch	10 inch	10 inch	10 inch	10 inch	10 inch
90	10 inch	10 inch	10 inch	10 inch	10 inch	10 inch	10 inch	10 inch	10 inch	10 inch	10 inch
105	10 inch	10 inch	10 inch	10 inch	10 inch	10 inch	10 inch	10 inch	10 inch	10 inch	10 inch
120	10 inch	10 inch	10 inch	10 inch	10 inch	10 inch	10 inch	10 inch	10 inch	10 inch	10 inch
135	10 inch	10 inch	10 inch	10 inch	10 inch	10 inch	10 inch	10 inch	10 inch	10 inch	10 inch
150	10 inch	10 inch	10 inch	10 inch	10 inch	10 inch	10 inch	10 inch	10 inch	10 inch	10 inch
160	10 inch	10 inch	10 inch	10 inch	10 inch	10 inch	10 inch	10 inch	10 inch	10 inch	10 inch
170	10 inch	10 inch	10 inch	10 inch	10 inch	10 inch	10 inch	10 inch	10 inch	10 inch	10 inch
180	10 inch	10 inch	10 inch	10 inch	10 inch	10 inch	10 inch	10 inch	10 inch	10 inch	10 inch
-170	10 inch	10 inch	10 inch	10 inch	10 inch	10 inch		10 inch		10 inch	
-120	10 inch		10 inch		10 inch						
-90	10 inch		10 inch		10 inch						
-60	10 inch		10 inch		10 inch						
-30	10 inch		10 inch		10 inch						
-10	10 inch	10 inch	10 inch	10 inch	10 inch	10 inch		10 inch		10 inch	

Table 3.2 Induced coefficient of surface pressure
at R = 4.0 and M_j = 0.74

R = 4.00; jet Mach number = 0.74; freestream q = 54.26 psf

r / D	+0°	+10°	+20°	+30°	+45°	+60°	+75°	+90°
0.58	0.501	0.448	0.260	-0.091	-0.818	-1.872	-3.065	-3.230
0.70	0.383	0.333	0.191	-0.024	-0.536	-1.230	-2.063	-2.718
0.75	0.369	0.326	0.204	0.004	-0.439	-1.066	-1.781	-2.405
0.80	0.352	0.311	0.204	0.027	-0.367	-0.919	-1.561	-2.135
0.90	0.305	0.274	0.188	0.045	-0.269	-0.719	-1.231	-1.715
1.00	0.268	0.239	0.169	0.070	-0.214	-0.579	-1.002	-1.421
1.20	0.209	0.188	0.134	0.048	-0.142	-0.410	-0.728	-1.027
1.40	0.168	0.151	0.111	0.058	-0.099	-0.315	-0.527	-0.768
1.60	0.140	0.131	0.095	0.042	-0.075	-0.225	-0.409	-0.600
1.80	0.121	0.112	0.085	0.040	-0.057	-0.179	-0.330	-0.485
2.00	0.108	0.099	0.076	0.040	-0.040	-0.141	-0.269	-0.393
2.25	0.091	0.085	0.066	0.040	-0.024	-0.113	-0.214	-0.318
2.50	0.084	0.076	0.063	0.039	-0.016	-0.090	-0.173	-0.267
2.75	0.074	0.071	0.059	0.037	-0.010	-0.071	-0.145	-0.226
3.00	0.069	0.064	0.053	0.036	-0.005	-0.059	-0.122	-0.185
3.25	0.065	0.061	0.051	0.035	0.000	-0.047	-0.101	-0.160
3.50	0.057	0.057	0.045	0.028	0.003	-0.040	-0.087	-0.136
3.75	0.051	0.052	0.045	0.036	0.005	-0.033	-0.072	-0.120
4.00	0.050	0.049	0.044	0.031	0.007	-0.026	-0.064	-0.104
5.00	0.039	0.037	0.035	0.029	0.012	-0.010	-0.037	-0.065
5.50	0.031	0.033	0.033	0.029	0.013	-0.006	-0.029	-0.052
6.00	0.029	0.033	0.033	0.025	0.013	-0.003	-0.023	-0.042

r / D	+90°	+105°	+120°	+135°	+150°	+160°	+170°	+180°
0.58	-3.230	-3.074	-2.809	-2.401	-2.259	-1.976	-1.782	-1.731
0.70	-2.718	-2.922	-2.535	-2.126	-1.954	-1.921	-1.790	-1.724
0.75	-2.405	-2.641	-2.343	-1.990	-1.801		-1.756	-1.696
0.80	-2.135	-2.379	-2.155	-1.850	-1.631	-1.466	-1.632	-1.599
0.90	-1.715	-1.963	-1.852	-1.592	-1.431		-1.339	-1.420
1.00	-1.421	-1.655	-1.603	-1.393	-1.208	-1.206	-1.192	-1.241
1.20	-1.027	-1.236	-1.239	-1.085	-0.913		-0.979	-1.004
1.40	-0.768	-0.947	-0.991	-0.875	-0.792	-0.788	-0.835	-0.844
1.60	-0.600	-0.752	-0.802	-0.725	-0.651	-0.663	-0.726	-0.739
1.80	-0.485	-0.605	-0.667	-0.614	-0.555	-0.560	-0.629	-0.655
2.00	-0.393	-0.505	-0.560	-0.523	-0.456	-0.475	-0.558	-0.589
2.25	-0.318	-0.414	-0.477	-0.450	-0.391	-0.400	-0.513	-0.533
2.50	-0.267	-0.340	-0.395	-0.378	-0.320	-0.334	-0.440	-0.462
2.75	-0.226	-0.288	-0.334	-0.323	-0.265	-0.276	-0.382	-0.415
3.00	-0.185	-0.245	-0.277	-0.276	-0.220	-0.229	-0.332	-0.372
3.25	-0.160		-0.243	-0.240	-0.185	-0.191	-0.292	-0.335
3.50	-0.136	-0.181	-0.208	-0.209	-0.156	-0.158	-0.255	-0.302
3.75	-0.120	-0.162	-0.185	-0.183	-0.132	-0.133	-0.222	-0.277
4.00	-0.104		-0.165	-0.158	-0.114	-0.113	-0.194	-0.251
5.00	-0.065	-0.089	-0.103	-0.100	-0.063	-0.051	-0.116	-0.183
5.50	-0.052	-0.071	-0.085	-0.081	-0.046	-0.034	-0.091	-0.159
6.00	-0.042	-0.058	-0.069	-0.065	-0.037	-0.021	-0.073	-0.142

Table 3.3 Induced coefficient of surface pressure
at R = 4.0 and M_j = 0.50

R = 3.98; jet Mach number = 0.50; freestream q = 24.21 psf

r / D	+0°	+10°	+20°	+30°	+45°	+60°	+75°	+90°
0.58	0.533	0.480	0.253	-0.165	-0.936	-2.163	-3.597	-4.617
0.70	0.418	0.364	0.204	-0.039	-0.603	-1.377	-2.315	-3.076
0.75	0.399	0.352	0.216	-0.008	-0.496	-1.189	-1.990	-2.705
0.80	0.375	0.332	0.211	0.014	-0.417	-1.027	-1.740	-2.390
0.90	0.321	0.286	0.191	0.033	-0.310	-0.803	-1.368	-1.910
1.00	0.279	0.253	0.170	0.058	-0.248	-0.647	-1.111	-1.572
1.20	0.214	0.192	0.132	0.037	-0.168	-0.460	-0.813	-1.094
1.40	0.170	0.153	0.107	0.049	-0.111	-0.325	-0.576	-0.836
1.60	0.142	0.132	0.094	0.037	-0.089	-0.254	-0.442	-0.646
1.80	0.123	0.113	0.084	0.035	-0.068	-0.196	-0.355	-0.518
2.00	0.110	0.100	0.077	0.037	-0.047	-0.152	-0.287	-0.417
2.25	0.094	0.088	0.067	0.039	-0.025	-0.121	-0.226	-0.334
2.50	0.088	0.079	0.065	0.041	-0.018	-0.094	-0.179	-0.277
2.75	0.077	0.075	0.064	0.039	-0.009	-0.073	-0.148	-0.230
3.00	0.074	0.069	0.057	0.040	-0.004	-0.059	-0.123	-0.183
3.25	0.072	0.066	0.056	0.039	0.002	-0.046	-0.101	-0.160
3.50	0.062	0.064	0.051	0.031	0.006	-0.037	-0.084	-0.134
3.75	0.056	0.058	0.052	0.043	0.010	-0.030	-0.067	-0.116
4.00	0.056	0.055	0.051	0.038	0.011	-0.022	-0.060	-0.100
5.00	0.049	0.043	0.043	0.037	0.019	-0.005	-0.032	-0.060
5.50	0.037	0.038	0.043	0.039	0.021	0.000	-0.024	-0.047
6.00	0.037	0.036	0.043	0.035	0.022	0.003	-0.017	-0.038

r / D	+90°	+105°	+120°	+135°	+150°	+160°	+170°	+180°
0.58	-4.617	-4.755	-3.653	-2.640	-2.428	-2.110	-1.881	-1.823
0.70	-3.076	-3.418	-2.909	-2.301	-2.101	-2.049	-1.894	-1.807
0.75	-2.705	-2.997	-2.614	-2.152	-1.934		-1.860	-1.793
0.80	-2.390	-2.676	-2.386	-2.000	-1.744	-1.550	-1.725	-1.691
0.90	-1.910	-2.186	-2.037	-1.721	-1.533		-1.397	-1.498
1.00	-1.572	-1.829	-1.755	-1.501	-1.283	-1.280	-1.235	-1.283
1.20	-1.094	-1.349	-1.346	-1.167	-0.964		-1.031	-1.024
1.40	-0.836	-1.025	-1.070	-0.940	-0.837	-0.828	-0.865	-0.859
1.60	-0.646	-0.808	-0.858	-0.774	-0.681	-0.694	-0.746	-0.744
1.80	-0.518	-0.646	-0.708	-0.651		-0.580	-0.645	-0.652
2.00	-0.417	-0.535	-0.590	-0.551	-0.471	-0.488	-0.573	-0.585
2.25	-0.334	-0.434	-0.502	-0.475	-0.401	-0.412	-0.518	-0.529
2.50	-0.277	-0.354	-0.413	-0.397	-0.329	-0.344	-0.447	-0.456
2.75	-0.230	-0.295	-0.346	-0.337	-0.270	-0.282	-0.389	-0.405
3.00	-0.183	-0.249	-0.285	-0.287	-0.221	-0.233	-0.339	-0.360
3.25	-0.160		-0.249	-0.248	-0.185	-0.194	-0.296	-0.322
3.50	-0.134	-0.182	-0.213	-0.215	-0.155	-0.159	-0.259	-0.287
3.75	-0.116	-0.160	-0.187	-0.186	-0.129	-0.133	-0.226	-0.261
4.00	-0.100		-0.166	-0.162	-0.111	-0.111	-0.198	-0.238
5.00	-0.060	-0.085	-0.095	-0.098	-0.060	-0.050	-0.118	-0.173
5.50	-0.047	-0.067	-0.081	-0.078	-0.042	-0.032	-0.092	-0.152
6.00	-0.038	-0.057	-0.065	-0.062	-0.034	-0.017	-0.074	-0.136

Table 3.4 Induced coefficient of surface pressure
at R = 6.0 and M_j = 0.91

R = 6.02; jet Mach number = 0.91; freestream q = 39.12 psf

r / D	+0°	+10°	+20°	+30°	+45°	+60°	+75°	+90°
0.58	0.468	0.388	0.116	-0.410	-1.412	-2.711	-4.022	-4.451
0.70	0.348	0.279	0.070	-0.243	-0.954	-1.845	-2.749	-3.225
0.75	0.315	0.255	0.080	-0.208	-0.819	-1.620	-2.405	-2.888
0.80	0.283	0.227	0.071	-0.183	-0.724	-1.429	-2.137	-2.593
0.90	0.213	0.170	0.045	-0.160	-0.593	-1.170	-1.741	-2.146
1.00	0.163	0.123	0.021	-0.210	-0.513	-0.985	-1.467	-1.835
1.20	0.090	0.060	-0.017	-0.141	-0.406	-0.768	-1.137	-1.411
1.40	0.044	0.023	-0.037	-0.149	-0.329	-0.626	-0.875	-1.118
1.60	0.019	0.007	-0.046	-0.121	-0.286	-0.494	-0.718	-0.921
1.80	0.006	-0.007	-0.047	-0.112	-0.250	-0.416	-0.610	-0.779
2.00	-0.001	-0.014	-0.047	-0.100	-0.212	-0.352	-0.519	-0.658
2.25	-0.006	-0.015	-0.044	-0.086		-0.300	-0.432	-0.553
2.50	-0.006	-0.017	-0.037	-0.071	-0.147	-0.255	-0.363	-0.478
2.75	-0.008	-0.012	-0.028	-0.062	-0.128	-0.217	-0.316	-0.415
3.00	-0.003	-0.011	-0.027	-0.052	-0.112	-0.190	-0.275	-0.352
3.25	0.001	-0.006	-0.021	-0.045	-0.096	-0.163	-0.237	-0.309
3.50	-0.003	-0.003	-0.020	-0.030	-0.084	-0.145	-0.209	-0.270
3.75	-0.004	-0.003	-0.012	-0.026	-0.072	-0.128	-0.177	-0.242
4.00	0.001	-0.001	-0.008	-0.027	-0.064	-0.111	-0.164	-0.215
5.00	0.009	0.001	0.000	-0.011	-0.035		-0.106	-0.142
5.50	0.002	0.001	0.004	-0.003	-0.026	-0.054	-0.088	-0.118
6.00	0.005	0.003	0.009	-0.001	-0.019	-0.043	-0.071	-0.098

r / D	+90°	+105°	+120°	+135°	+150°	+160°	+170°	+180°
0.58	-4.451	-3.944	-2.692	-2.021	-1.820	-1.500	-1.341	-1.294
0.70	-3.225	-3.090	-2.320	-1.827	-1.679	-1.594	-1.428	-1.365
0.75	-2.888	-2.783	-2.140	-1.731	-1.568		-1.430	-1.378
0.80	-2.593	-2.544	-2.007	-1.628	-1.428	-1.252	-1.352	-1.320
0.90	-2.146	-2.167	-1.785	-1.426	-1.263		-1.114	-1.185
1.00	-1.835	-1.887	-1.596	-1.262	-1.069	-1.036	-0.981	-1.017
1.20	-1.411	-1.497	-1.304	-1.009	-0.797		-0.773	-0.776
1.40	-1.118	-1.215	-1.097	-0.832	-0.677	-0.630	-0.612	-0.606
1.60	-0.921	-1.015	-0.928	-0.705	-0.545	-0.514	-0.500	-0.493
1.80	-0.779	-0.855	-0.804	-0.608	-0.455	-0.424	-0.409	-0.408
2.00	-0.658	-0.741	-0.701	-0.528	-0.376	-0.350	-0.350	-0.343
2.25	-0.553	-0.633	-0.621	-0.471	-0.329	-0.298	-0.310	-0.299
2.50	-0.478	-0.537	-0.532	-0.407	-0.270	-0.242	-0.255	-0.241
2.75	-0.415	-0.467	-0.464	-0.358	-0.227	-0.199	-0.215	-0.208
3.00	-0.352	-0.407	-0.395	-0.317	-0.188	-0.164	-0.181	-0.178
3.25	-0.309		-0.356	-0.285	-0.161	-0.136	-0.157	-0.154
3.50	-0.270	-0.314	-0.313	-0.255	-0.138	-0.114	-0.134	-0.134
3.75	-0.242	-0.285	-0.285	-0.230	-0.121	-0.096	-0.116	-0.116
4.00	-0.215		-0.259	-0.206	-0.106	-0.081	-0.098	-0.101
5.00	-0.142	-0.170	-0.172	-0.143	-0.066	-0.037	-0.053	-0.060
5.50	-0.118	-0.141	-0.147	-0.121	-0.052	-0.026	-0.039	-0.046
6.00	-0.098	-0.117	-0.124	-0.102	-0.045	-0.015	-0.028	-0.039

Table 3.5 Induced coefficient of surface pressure
at R = 6.0 and M_j = 0.74

R = 5.99; jet Mach Number = 0.74; freestream q = 24.62 psf

r / D	+0°	+10°	+20°	+30°	+45°	+60°	+75°	+90°
0.58	0.479	0.398	0.111	-0.450	-1.492	-2.957	-4.361	-4.894
0.70	0.354	0.285	0.066	-0.264	-1.010	-1.940	-2.882	-3.356
0.75	0.317	0.257	0.073	-0.229	-0.870	-1.706	-2.520	-3.003
0.80	0.281	0.224	0.061	-0.206	-0.771	-1.507	-2.240	-2.698
0.90	0.206	0.163	0.030	-0.184	-0.635	-1.236	-1.828	-2.236
1.00	0.153	0.125	0.005	-0.254	-0.552	-1.044	-1.542	-1.912
1.20	0.077	0.046	-0.035	-0.165	-0.439	-0.814	-1.205	-1.473
1.40	0.030	0.008	-0.056	-0.172	-0.364	-0.673	-0.923	-1.171
1.60	0.006	-0.007	-0.062	-0.140	-0.311	-0.529	-0.756	-0.962
1.80	-0.007	-0.019	-0.061	-0.129	-0.271	-0.443	-0.641	-0.812
2.00	-0.013	-0.026	-0.059	-0.114	-0.230	-0.374	-0.545	-0.684
2.25	-0.015	-0.024	-0.054	-0.097		-0.318	-0.452	-0.573
2.50	-0.014	-0.026	-0.046	-0.079	-0.158	-0.269	-0.379	-0.493
2.75	-0.014	-0.018	-0.033	-0.069	-0.137	-0.227	-0.328	-0.426
3.00	-0.007	-0.015	-0.031	-0.056	-0.120	-0.199	-0.284	-0.358
3.25	-0.002	-0.009	-0.024	-0.048	-0.102	-0.170	-0.244	-0.317
3.50	-0.005	-0.004	-0.022	-0.028	-0.089	-0.150	-0.214	-0.275
3.75	-0.006	-0.005	-0.012	-0.026	-0.075	-0.132	-0.180	-0.244
4.00	0.000	-0.002	-0.007	-0.026	-0.066	-0.114	-0.166	-0.217
5.00	0.011	0.003	0.004	-0.007	-0.033		-0.106	-0.142
5.50	0.003	0.004	0.009	0.004	-0.022	-0.052	-0.087	-0.118
6.00	0.007	0.007	0.016	0.005	-0.014	-0.041	-0.070	-0.097

r / D	+90°	+105°	+120°	+135°	+150°	+160°	+170°	+180°
0.58	-4.894	-4.210	-2.709	-2.037	-1.850	-1.510	-1.340	-1.289
0.70	-3.356	-3.171	-2.337	-1.850	-1.728	-1.634	-1.453	-1.375
0.75	-3.003	-2.857	-2.159	-1.754	-1.623		-1.468	-1.404
0.80	-2.698	-2.608	-2.025	-1.650	-1.474	-1.289	-1.395	-1.357
0.90	-2.236	-2.225	-1.806	-1.446	-1.304		-1.155	-1.231
1.00	-1.912	-1.940	-1.618	-1.279	-1.099	-1.077	-1.019	-1.059
1.20	-1.473	-1.543	-1.326	-1.024	-0.813		-0.786	-0.793
1.40	-1.171	-1.255	-1.119	-0.843	-0.685	-0.638	-0.612	-0.611
1.60	-0.962	-1.049	-0.947	-0.713	-0.544	-0.510	-0.484	-0.488
1.80	-0.812	-0.882	-0.818	-0.613		-0.414	-0.388	-0.398
2.00	-0.684	-0.763	-0.711	-0.529	-0.371	-0.339	-0.323	-0.329
2.25	-0.573	-0.648	-0.629	-0.473	-0.320	-0.288	-0.289	-0.276
2.50	-0.493	-0.550	-0.539	-0.407	-0.261	-0.232	-0.235	-0.218
2.75	-0.426	-0.475	-0.468	-0.356	-0.215	-0.187	-0.194	-0.181
3.00	-0.358	-0.414	-0.399	-0.314	-0.177	-0.152	-0.158	-0.149
3.25	-0.317		-0.359	-0.282	-0.151	-0.124	-0.136	-0.121
3.50	-0.275	-0.318	-0.315	-0.252	-0.127	-0.102	-0.113	-0.101
3.75	-0.244	-0.287	-0.285	-0.226	-0.111	-0.085	-0.094	-0.085
4.00	-0.217		-0.258	-0.202	-0.096	-0.070	-0.078	-0.072
5.00	-0.142	-0.169	-0.168	-0.138	-0.057	-0.030	-0.040	-0.039
5.50	-0.118	-0.140	-0.145	-0.117	-0.043	-0.016	-0.025	-0.028
6.00	-0.097	-0.119	-0.121	-0.098	-0.038	-0.005	-0.017	-0.022

Table 3.6 Induced coefficient of surface pressure
at R = 6.0 and M_j = 0.50

R = 5.99; jet Mach number = 0.50; freestream q = 10.82 psf

r / D	+0°	+10°	+20°	+30°	+45°	+60°	+75°	+90°
0.58	0.475	0.392	0.074	-0.587	-1.573	-3.187	-4.679	-5.210
0.70	0.348	0.274	0.045	-0.301	-1.066	-2.022	-2.982	-3.442
0.75	0.306	0.243	0.049	-0.265	-0.924	-1.780	-2.606	-3.076
0.80	0.265	0.206	0.036	-0.242	-0.820	-1.576	-2.315	-2.759
0.90	0.185	0.142	0.002	-0.220	-0.680	-1.295	-1.890	-2.290
1.00	0.130	0.089	-0.022	-0.192	-0.593	-1.095	-1.595	-1.955
1.20	0.052	0.022	-0.064	-0.198	-0.473	-0.861	-1.222	-1.449
1.40	0.005	-0.017	-0.082	-0.174	-0.398	-0.660	-0.956	-1.197
1.60	-0.018	-0.030	-0.087	-0.168	-0.343	-0.559	-0.782	-0.984
1.80	-0.028	-0.042	-0.084	-0.155	-0.300	-0.467	-0.665	-0.830
2.00	-0.033	-0.046	-0.080	-0.136	-0.255	-0.394	-0.566	-0.699
2.25	-0.033	-0.042	-0.074	-0.116		-0.341	-0.473	-0.589
2.50	-0.030	-0.043	-0.062	-0.096	-0.179	-0.288	-0.398	-0.507
2.75	-0.030	-0.034	-0.047	-0.084	-0.156	-0.244	-0.343	-0.437
3.00	-0.021	-0.029	-0.046	-0.071	-0.136	-0.214	-0.298	-0.332
3.25	-0.011	-0.021	-0.036	-0.062	-0.116	-0.184	-0.258	-0.328
3.50	-0.016	-0.013	-0.035		-0.101	-0.163	-0.226	-0.285
3.75	-0.018	-0.014	-0.022	-0.038	-0.086	-0.145	-0.189	-0.253
4.00	-0.009	-0.010	-0.017	-0.039	-0.077	-0.125	-0.176	-0.225
5.00	0.005	-0.004	-0.007	-0.015	-0.043		-0.113	-0.148
5.50	-0.007	-0.004	0.001	-0.003	-0.031	-0.059	-0.093	-0.122
6.00	-0.005	-0.002	0.005	-0.005	-0.023	-0.047	-0.075	-0.101

r / D	+90°	+105°	+120°	+135°	+150°	+160°	+170°	+180°
0.58	-5.210	-4.458	-2.693	-1.955	-1.759	-1.425	-1.260	-1.202
0.70	-3.442	-3.205	-2.316	-1.785	-1.658	-1.552	-1.359	-1.277
0.75	-3.076	-2.887	-2.132	-1.695	-1.559		-1.382	-1.317
0.80	-2.759	-2.630	-2.005	-1.594	-1.409	-1.211	-1.320	-1.281
0.90	-2.290	-2.242	-1.786	-1.388	-1.247		-1.081	-1.169
1.00	-1.955	-1.952	-1.601	-1.225	-1.035	-1.017	-0.953	-1.005
1.20	-1.449	-1.551	-1.311	-0.981	-0.755		-0.754	-0.764
1.40	-1.197	-1.261	-1.108	-0.775	-0.644	-0.597	-0.571	-0.585
1.60	-0.984	-1.058	-0.936	-0.687	-0.503	-0.474	-0.442	-0.461
1.80	-0.830	-0.888	-0.806	-0.591		-0.376	-0.341	-0.368
2.00	-0.699	-0.768	-0.700	-0.509	-0.336	-0.302	-0.277	-0.296
2.25	-0.589	-0.658	-0.628	-0.463	-0.297	-0.262	-0.250	-0.244
2.50	-0.507	-0.558	-0.541	-0.401	-0.243	-0.208	-0.201	-0.190
2.75	-0.437	-0.483	-0.470	-0.351	-0.201	-0.165	-0.163	-0.155
3.00	-0.332	-0.420	-0.400	-0.312	-0.165	-0.134	-0.132	-0.124
3.25	-0.328		-0.361	-0.279	-0.141	-0.108	-0.109	-0.097
3.50	-0.285	-0.325	-0.317	-0.250	-0.118	-0.089	-0.091	-0.077
3.75	-0.253	-0.293	-0.288	-0.223	-0.104	-0.074	-0.075	-0.061
4.00	-0.225		-0.261	-0.201	-0.091	-0.059	-0.063	-0.048
5.00	-0.148	-0.173		-0.139	-0.054	-0.021	-0.028	-0.017
5.50	-0.122	-0.129	-0.147	-0.118	-0.043	-0.012	-0.019	-0.008
6.00	-0.101	-0.118	-0.124	-0.100	-0.037	-0.001	-0.011	-0.004

Table 3.7 Induced coefficient of surface pressure
at R = 8.0 and M_j = 0.91

R = 8.00; jet Mach number = 0.91; freestream q = 21.98 psf

r / D	+0°	+10°	+20°	+30°	+45°	+60°	+75°	+90°
0.58	0.533	0.480	0.253	-0.165	-0.936	-2.163	-3.597	-4.617
0.70	0.418	0.364	0.204	-0.039	-0.603	-1.377	-2.315	-3.076
0.75	0.399	0.352	0.216	-0.008	-0.496	-1.189	-1.990	-2.705
0.80	0.375	0.332	0.211	0.014	-0.417	-1.027	-1.740	-2.390
0.90	0.321	0.286	0.191	0.033	-0.310	-0.803	-1.368	-1.910
1.00	0.279	0.253	0.170	0.058	-0.248	-0.647	-1.111	-1.572
1.20	0.214	0.192	0.132	0.037	-0.168	-0.460	-0.813	-1.094
1.40	0.170	0.153	0.107	0.049	-0.111	-0.325	-0.576	-0.836
1.60	0.142	0.132	0.094	0.037	-0.089	-0.254	-0.442	-0.646
1.80	0.123	0.113	0.084	0.035	-0.068	-0.196	-0.355	-0.518
2.00	0.110	0.100	0.077	0.037	-0.047	-0.152	-0.287	-0.417
2.25	0.094	0.088	0.067	0.039	-0.025	-0.121	-0.226	-0.334
2.50	0.088	0.079	0.065	0.041	-0.018	-0.094	-0.179	-0.277
2.75	0.077	0.075	0.064	0.039	-0.009	-0.073	-0.148	-0.230
3.00	0.074	0.069	0.057	0.040	-0.004	-0.059	-0.123	-0.183
3.25	0.072	0.066	0.056	0.039	0.002	-0.046	-0.101	-0.160
3.50	0.062	0.064	0.051	0.031	0.006	-0.037	-0.084	-0.134
3.75	0.056	0.058	0.052	0.043	0.010	-0.030	-0.067	-0.116
4.00	0.056	0.055	0.051	0.038	0.011	-0.022	-0.060	-0.100
5.00	0.049	0.043	0.043	0.037	0.019	-0.005	-0.032	-0.060
5.50	0.037	0.038	0.043	0.039	0.021	0.000	-0.024	-0.047
6.00	0.037	0.036	0.043	0.035	0.022	0.003	-0.017	-0.038

r / D	+90°	+105°	+120°	+135°	+150°	+160°	+170°	+180°
0.58	-4.617	-4.755	-3.653	-2.640	-2.428	-2.110	-1.881	-1.823
0.70	-3.076	-3.418	-2.909	-2.301	-2.101	-2.049	-1.894	-1.807
0.75	-2.705	-2.997	-2.614	-2.152	-1.934		-1.860	-1.793
0.80	-2.390	-2.676	-2.386	-2.000	-1.744	-1.550	-1.725	-1.691
0.90	-1.910	-2.186	-2.037	-1.721	-1.533		-1.397	-1.498
1.00	-1.572	-1.829	-1.755	-1.501	-1.283	-1.280	-1.235	-1.283
1.20	-1.094	-1.349	-1.346	-1.167	-0.964		-1.031	-1.024
1.40	-0.836	-1.025	-1.070	-0.940	-0.837	-0.828	-0.865	-0.859
1.60	-0.646	-0.808	-0.858	-0.774	-0.681	-0.694	-0.746	-0.744
1.80	-0.518	-0.646	-0.708	-0.651		-0.580	-0.645	-0.652
2.00	-0.417	-0.535	-0.590	-0.551	-0.471	-0.488	-0.573	-0.585
2.25	-0.334	-0.434	-0.502	-0.475	-0.401	-0.412	-0.518	-0.529
2.50	-0.277	-0.354	-0.413	-0.397	-0.329	-0.344	-0.447	-0.456
2.75	-0.230	-0.295	-0.346	-0.337	-0.270	-0.282	-0.389	-0.405
3.00	-0.183	-0.249	-0.285	-0.287	-0.221	-0.233	-0.339	-0.360
3.25	-0.160		-0.249	-0.248	-0.185	-0.194	-0.296	-0.322
3.50	-0.134	-0.182	-0.213	-0.215	-0.155	-0.159	-0.259	-0.287
3.75	-0.116	-0.160	-0.187	-0.186	-0.129	-0.133	-0.226	-0.261
4.00	-0.100		-0.166	-0.162	-0.111	-0.111	-0.198	-0.238
5.00	-0.060	-0.085	-0.095	-0.098	-0.060	-0.050	-0.118	-0.173
5.50	-0.047	-0.067	-0.081	-0.078	-0.042	-0.032	-0.092	-0.152
6.00	-0.038	-0.057	-0.065	-0.062	-0.034	-0.017	-0.074	-0.136

Table 3.8 Induced coefficient of surface pressure
at R = 8.1 and M_j = 0.74

R = 8.06; jet Mach number = 0.74; freestream q = 13.71 psf								
r / D	+0°	+10°	+20°	+30°	+45°	+60°	+75°	+90°
0.58	0.416	0.322	0.004	-0.644	-1.650	-3.082	-4.115	-4.171
0.70	0.283	0.205	-0.035	-0.391	-1.139	-1.975	-2.657	-2.781
0.75	0.235	0.167	-0.035	-0.356	-0.999	-1.756	-2.346	-2.510
0.80	0.192	0.128	-0.053	-0.336	-0.900	-1.565	-2.101	-2.272
0.90	0.104	0.060	-0.091	-0.319	-0.768	-1.311	-1.747	-1.926
1.00	0.046	0.004	-0.118		-0.687	-1.131	-1.505	-1.681
1.20	-0.040	-0.075	-0.164	-0.303	-0.576	-0.936	-1.259	-1.347
1.40	-0.093	-0.117	-0.187		-0.502	-0.785	-0.979	-1.118
1.60	-0.118	-0.130	-0.194	-0.278	-0.453	-0.656	-0.831	-0.955
1.80	-0.129	-0.142	-0.190	-0.265	-0.413	-0.569	-0.735	-0.837
2.00	-0.132	-0.147	-0.184	-0.244	-0.367	-0.500	-0.649	-0.730
2.25	-0.127	-0.138	-0.173	-0.222		-0.450	-0.565	-0.644
2.50	-0.122	-0.136	-0.158	-0.195	-0.282	-0.396	-0.493	-0.574
2.75	-0.117	-0.120	-0.137	-0.178	-0.256	-0.348	-0.440	-0.513
3.00	-0.102	-0.110	-0.130	-0.159	-0.233	-0.315	-0.395	-0.427
3.25	-0.088	-0.098	-0.117	-0.146	-0.208	-0.280	-0.351	-0.408
3.50	-0.089	-0.086	-0.110		-0.188	-0.255	-0.317	-0.365
3.75	-0.086	-0.083	-0.093	-0.111	-0.168	-0.233	-0.274	-0.333
4.00	-0.073	-0.075	-0.083	-0.110	-0.154	-0.208	-0.261	-0.303
5.00	-0.046	-0.056	-0.059	-0.071	-0.104		-0.183	-0.216
5.50	-0.054	-0.050	-0.047	-0.051	-0.085	-0.118	-0.157	-0.186
6.00	-0.048	-0.045	-0.036	-0.049	-0.071	-0.100	-0.133	-0.160

r / D	+90°	+105°	+120°	+135°	+150°	+160°	+170°	+180°
0.58	-4.171	-3.148	-1.740	-1.354	-1.238	-1.050	-0.959	-0.922
0.70	-2.781	-2.320	-1.566	-1.286	-1.229	-1.156	-1.019	-0.956
0.75	-2.510	-2.123	-1.465	-1.242	-1.195		-1.042	-0.988
0.80	-2.272	-1.964	-1.403	-1.190	-1.115	-0.952	-1.005	-0.968
0.90	-1.926	-1.720	-1.283	-1.066	-1.034		-0.841	-0.902
1.00	-1.681	-1.535	-1.180	-0.955	-0.886	-0.849	-0.755	-0.785
1.20	-1.347	-1.279	-1.008	-0.777	-0.667		-0.603	-0.615
1.40	-1.118	-1.080	-0.886	-0.638	-0.569	-0.510	-0.464	-0.468
1.60	-0.955	-0.940	-0.772	-0.554	-0.447	-0.401	-0.361	-0.370
1.80	-0.837	-0.818	-0.687	-0.482		-0.317	-0.275	-0.293
2.00	-0.730	-0.734	-0.615	-0.421	-0.301	-0.257	-0.221	-0.237
2.25	-0.644	-0.657	-0.570	-0.390	-0.265	-0.226	-0.198	-0.191
2.50	-0.574	-0.578	-0.508	-0.346	-0.217	-0.180	-0.157	-0.145
2.75	-0.513	-0.517	-0.456	-0.308	-0.180	-0.145	-0.125	-0.117
3.00	-0.427	-0.464	-0.399	-0.280	-0.147	-0.118	-0.095	-0.092
3.25	-0.408		-0.370	-0.257	-0.126	-0.093	-0.076	-0.069
3.50	-0.365	-0.379	-0.334	-0.235	-0.104	-0.076	-0.058	-0.052
3.75	-0.333	-0.351	-0.310	-0.214	-0.092	-0.062	-0.044	-0.037
4.00	-0.303		-0.288	-0.196	-0.078	-0.048	-0.032	-0.023
5.00	-0.216	-0.231	-0.199	-0.144	-0.044	-0.010	0.002	0.016
5.50	-0.186	-0.179	-0.184	-0.126	-0.033	-0.002	0.012	0.027
6.00	-0.160	-0.170	-0.160	-0.110	-0.028	0.009	0.020	0.031

Table 3.9 Induced coefficient of surface pressure
at R = 7.9 and M_j = 0.49

R = 7.87; jet Mach number = 0.49; freestream q = 6.08 psf								
r / D	+0°	+10°	+20°	+30°	+45°	+60°	+75°	+90°
0.58	0.436	0.345	0.006	-0.790	-1.667	-3.219	-4.283	-4.268
0.70	0.294	0.215	-0.030	-0.390	-1.153	-2.011	-2.709	-2.837
0.75	0.244	0.177	-0.030	-0.356	-1.013	-1.779	-2.389	-2.560
0.80	0.198	0.134	-0.048	-0.337	-0.912	-1.591	-2.137	-2.315
0.90	0.108	0.062	-0.089	-0.321	-0.778	-1.331	-1.775	-1.960
1.00	0.045	0.001	-0.118		-0.695	-1.147	-1.527	-1.684
1.20	-0.044	-0.076	-0.167	-0.309	-0.583	-0.906	-1.130	
1.40	-0.098	-0.120	-0.189	-0.290	-0.509	-0.651	-0.988	-1.129
1.60	-0.121	-0.134	-0.196	-0.282	-0.459	-0.662	-0.836	-0.961
1.80	-0.131	-0.147	-0.193	-0.269	-0.417	-0.571	-0.737	-0.837
2.00	-0.134	-0.148	-0.186	-0.246	-0.370	-0.498	-0.649	-0.730
2.25	-0.128	-0.139	-0.175	-0.222		-0.450	-0.564	-0.643
2.50	-0.123	-0.138	-0.158	-0.195	-0.283	-0.394	-0.493	-0.572
2.75	-0.119	-0.122	-0.135	-0.178	-0.255	-0.346	-0.437	-0.509
3.00	-0.102	-0.110	-0.130	-0.159	-0.231	-0.313	-0.391	
3.25	-0.085	-0.097	-0.115	-0.144	-0.207	-0.277	-0.347	-0.404
3.50	-0.089	-0.083	-0.110		-0.186	-0.252	-0.313	-0.361
3.75	-0.087	-0.081	-0.091	-0.107	-0.166	-0.229	-0.269	-0.327
4.00	-0.072	-0.074	-0.082	-0.109	-0.152	-0.204	-0.256	-0.296
5.00	-0.043	-0.054	-0.058	-0.069	-0.101		-0.178	-0.210
5.50	-0.053	-0.048	-0.044	-0.049	-0.084	-0.114	-0.152	-0.180
6.00	-0.048	-0.043	-0.035	-0.049	-0.070	-0.097	-0.127	-0.154

r / D	+90°	+105°	+120°	+135°	+150°	+160°	+170°	+180°
0.58	-4.268	-3.300	-1.714	-1.267	-1.144	-0.994	-0.906	-0.868
0.70	-2.837	-2.364	-1.541	-1.219	-1.178	-1.102	-0.955	-0.880
0.75	-2.560	-2.168	-1.436	-1.182	-1.155		-0.984	-0.919
0.80	-2.315	-1.995	-1.379	-1.135	-1.075	-0.897	-0.955	-0.911
0.90	-1.960	-1.744	-1.268	-1.016	-1.003		-0.793	-0.865
1.00	-1.684	-1.552	-1.170	-0.913	-0.858	-0.828	-0.720	-0.759
1.20		-1.285	-1.000	-0.748	-0.643		-0.604	-0.611
1.40	-1.129	-1.052	-0.879		-0.553	-0.495	-0.441	-0.471
1.60	-0.961	-0.945	-0.763	-0.538	-0.421	-0.384	-0.335	-0.362
1.80	-0.837	-0.819	-0.676	-0.469		-0.296	-0.245	-0.280
2.00	-0.730	-0.732	-0.602	-0.406	-0.275	-0.232	-0.192	-0.208
2.25	-0.643	-0.656	-0.570	-0.387	-0.250	-0.210	-0.179	-0.178
2.50	-0.572	-0.577	-0.508	-0.345	-0.206	-0.167	-0.140	-0.131
2.75	-0.509	-0.515	-0.455	-0.308	-0.170	-0.132	-0.110	-0.102
3.00		-0.460	-0.398	-0.280	-0.139	-0.104	-0.082	-0.077
3.25	-0.404		-0.368	-0.256	-0.118	-0.080	-0.063	-0.052
3.50	-0.361	-0.375	-0.332	-0.234	-0.097	-0.065	-0.046	-0.035
3.75	-0.327	-0.345	-0.307	-0.212	-0.086	-0.051	-0.033	-0.020
4.00	-0.296		-0.285	-0.195	-0.074	-0.038	-0.021	-0.009
5.00	-0.210	-0.225		-0.143	-0.042	-0.002	0.012	0.025
5.50	-0.180	-0.229	-0.179	-0.125	-0.034	0.006	0.021	0.036
6.00	-0.154	-0.164	-0.156	-0.109	-0.028	0.016	0.027	0.040

Table 3.10 Induced coefficient of surface pressure
at R = 12.1 and M_j = 0.91

R = 12.05; jet Mach number = 0.91; freestream q = 9.71 psf

r / D	+0°	+10°	+20°	+30°	+45°	+60°	+75°	+90°
0.58	0.315	0.221	-0.074	-0.705	-1.502	-2.708	-3.312	-3.286
0.70	0.191	0.123	-0.097	-0.422	-1.044	-1.697	-2.142	-2.133
0.75	0.138	0.076	-0.107	-0.391	-0.926	-1.504	-1.900	-1.922
0.80	0.102	0.040	-0.129	-0.380	-0.840	-1.357	-1.703	-1.737
0.90	0.009	-0.018	-0.166	-0.370	-0.727	-1.148	-1.423	-1.480
1.00	-0.036	-0.073	-0.190	-0.312	-0.664	-0.999	-1.238	-1.297
1.20	-0.118	-0.157	-0.236	-0.357	-0.570	-0.859	-1.061	-1.050
1.40	-0.181	-0.202	-0.269	-0.331	-0.511	-0.680	-0.835	-0.885
1.60	-0.209	-0.210	-0.279	-0.350	-0.489	-0.627	-0.718	-0.770
1.80	-0.223	-0.230	-0.277	-0.346	-0.467	-0.557	-0.658	-0.687
2.00	-0.229	-0.245	-0.277	-0.330	-0.424	-0.501	-0.603	-0.611
2.25	-0.222	-0.233	-0.269	-0.308		-0.485	-0.550	-0.568
2.50	-0.218	-0.238	-0.253	-0.282	-0.357	-0.441	-0.498	-0.522
2.75	-0.217	-0.214	-0.228	-0.270	-0.335	-0.403	-0.458	-0.481
3.00	-0.196	-0.208	-0.226	-0.252	-0.316	-0.376	-0.422	
3.25	-0.176	-0.192	-0.209	-0.239	-0.292	-0.346	-0.389	-0.405
3.50	-0.184	-0.175	-0.207		-0.274	-0.326	-0.360	-0.374
3.75	-0.183	-0.174	-0.181	-0.195	-0.253	-0.308	-0.322	-0.351
4.00	-0.162	-0.164	-0.169	-0.200	-0.241	-0.282	-0.314	-0.326
5.00	-0.122	-0.140	-0.143	-0.151	-0.183		-0.245	-0.256
5.50	-0.138	-0.133	-0.124	-0.125	-0.162	-0.190	-0.220	-0.232
6.00	-0.128	-0.124	-0.110	-0.127	-0.143	-0.168	-0.193	-0.207

r / D	+90°	+105°	+120°	+135°	+150°	+160°	+170°	+180°
0.58	-3.286	-2.380	-1.319	-0.976	-0.908	-0.760	-0.684	-0.662
0.70	-2.133	-1.711	-1.131	-0.904	-0.870	-0.787	-0.681	-0.634
0.75	-1.922	-1.550	-1.036	-0.865	-0.832		-0.673	-0.630
0.80	-1.737	-1.427	-0.985	-0.821	-0.765	-0.609	-0.622	-0.589
0.90	-1.480	-1.247	-0.886	-0.723	-0.698		-0.472	-0.500
1.00	-1.297	-1.105	-0.808	-0.642	-0.589	-0.512	-0.397	-0.389
1.20	-1.050	-0.924	-0.681	-0.520	-0.439		-0.305	-0.266
1.40	-0.885	-0.783	-0.603	-0.430	-0.387	-0.305	-0.209	-0.191
1.60	-0.770	-0.697	-0.526	-0.371	-0.307	-0.248	-0.161	-0.153
1.80	-0.687	-0.608	-0.473	-0.321		-0.202	-0.125	-0.123
2.00	-0.611	-0.562	-0.431	-0.280	-0.222	-0.175	-0.110	-0.113
2.25	-0.568	-0.530	-0.418	-0.272	-0.211	-0.173	-0.121	-0.100
2.50	-0.522	-0.479	-0.384	-0.245	-0.181	-0.150	-0.108	-0.081
2.75	-0.481	-0.442	-0.354	-0.220	-0.155	-0.128	-0.096	-0.074
3.00		-0.404	-0.317	-0.205	-0.127	-0.114	-0.079	-0.063
3.25	-0.405		-0.300	-0.193	-0.114	-0.096	-0.072	-0.051
3.50	-0.374	-0.349	-0.278	-0.181	-0.093	-0.087	-0.061	-0.043
3.75	-0.351	-0.331	-0.264	-0.166	-0.088	-0.078	-0.054	-0.035
4.00	-0.326		-0.249	-0.156	-0.074	-0.066	-0.047	-0.031
5.00	-0.256	-0.246		-0.119	-0.039	-0.033	-0.021	-0.003
5.50	-0.232		-0.183	-0.107	-0.028	-0.027	-0.014	0.007
6.00	-0.207	-0.190	-0.165	-0.097	-0.023	-0.013	-0.004	0.008

Table 3.11 Induced coefficient of surface pressure
at R = 12.1 and M_j = 0.74

R = 12.05; jet Mach number = 0.74; freestream q = 6.24 psf								
r / D	+0°	+10°	+20°	+30°	+45°	+60°	+75°	+90°
0.58	0.316	0.236	-0.058	-0.796	-1.470	-2.774	-3.474	-3.353
0.70	0.186	0.125	-0.088	-0.405	-1.026	-1.681	-2.133	-2.133
0.75	0.133	0.079	-0.099	-0.380	-0.912	-1.494	-1.892	-1.923
0.80	0.093	0.039	-0.124	-0.371	-0.830	-1.347	-1.698	-1.738
0.90	0.001	-0.024	-0.167	-0.365	-0.723	-1.142	-1.421	-1.479
1.00	-0.050	-0.099	-0.193	-0.343	-0.662	-0.996	-1.235	-1.295
1.20	-0.135	-0.166	-0.244	-0.363	-0.575	-0.871	-1.119	-1.000
1.40	-0.196	-0.214	-0.274	-0.357	-0.515	-0.710	-0.836	-0.881
1.60	-0.222	-0.225	-0.287	-0.357	-0.494	-0.634	-0.721	-0.765
1.80	-0.236	-0.244	-0.286	-0.352	-0.471	-0.561	-0.658	-0.681
2.00	-0.241	-0.255	-0.284	-0.335	-0.431	-0.506	-0.601	-0.607
2.25	-0.234	-0.244	-0.277	-0.315		-0.486	-0.547	-0.562
2.50	-0.230	-0.247	-0.261	-0.289	-0.361	-0.442	-0.495	-0.517
2.75	-0.227	-0.244	-0.236	-0.276	-0.339	-0.404	-0.455	-0.475
3.00	-0.207	-0.216	-0.233	-0.257	-0.318	-0.377	-0.420	
3.25	-0.185	-0.200	-0.216	-0.243	-0.295	-0.347	-0.386	-0.400
3.50	-0.192	-0.182	-0.212		-0.276	-0.326	-0.357	-0.370
3.75	-0.190	-0.180	-0.187	-0.200	-0.255	-0.307	-0.319	-0.346
4.00	-0.170	-0.170	-0.175	-0.204	-0.243	-0.281	-0.311	-0.322
5.00	-0.128	-0.143	-0.145	-0.154	-0.183		-0.242	-0.252
5.50	-0.140	-0.134	-0.125	-0.127	-0.162	-0.188	-0.216	-0.227
6.00	-0.129	-0.124	-0.111	-0.127	-0.143	-0.166	-0.189	-0.203

r / D	+90°	+105°	+120°	+135°	+150°	+160°	+170°	+180°
0.58	-3.353	-2.532	-1.318	-0.932	-0.855	-0.714	-0.651	-0.626
0.70	-2.133	-1.715	-1.119	-0.857	-0.813	-0.736	-0.644	-0.598
0.75	-1.923	-1.553	-1.017	-0.819	-0.778		-0.635	-0.598
0.80	-1.738	-1.425	-0.966	-0.777	-0.712	-0.553	-0.582	-0.564
0.90	-1.479	-1.241	-0.866	-0.681	-0.645		-0.431	-0.478
1.00	-1.295	-1.098	-0.786	-0.602	-0.540	-0.470	-0.362	-0.366
1.20	-1.000	-0.914	-0.659	-0.485	-0.403		-0.288	-0.243
1.40	-0.881	-0.772	-0.584		-0.356	-0.279	-0.179	-0.173
1.60	-0.765	-0.687	-0.507	-0.345	-0.280	-0.228	-0.139	-0.134
1.80	-0.681	-0.600	-0.454	-0.300		-0.187	-0.103	-0.105
2.00	-0.607	-0.552	-0.412	-0.260	-0.202	-0.159	-0.087	-0.100
2.25	-0.562	-0.521	-0.407	-0.258	-0.199	-0.161	-0.107	-0.084
2.50	-0.517	-0.472	-0.374	-0.234	-0.173	-0.141	-0.097	-0.066
2.75	-0.475	-0.434	-0.345	-0.211	-0.148	-0.121	-0.086	-0.059
3.00		-0.398	-0.309	-0.196	-0.122	-0.106	-0.069	-0.050
3.25	-0.400		-0.292	-0.185	-0.109	-0.089	-0.064	-0.039
3.50	-0.370	-0.344	-0.272	-0.175	-0.090	-0.081	-0.053	-0.032
3.75	-0.346	-0.325	-0.258	-0.160	-0.084	-0.073	-0.046	-0.025
4.00	-0.322		-0.244	-0.151	-0.071	-0.062	-0.039	-0.023
5.00	-0.252	-0.242		-0.117	-0.038	-0.031	-0.017	0.003
5.50	-0.227		-0.178	-0.106	-0.030	-0.025	-0.010	0.013
6.00	-0.203	-0.187	-0.162	-0.096	-0.025	-0.011	-0.002	0.013

Table 3.12 Induced coefficient of surface pressure
at R = 11.9 and M_j = 0.50

R = 11.90; jet Mach number = 0.50; freestream q = 2.71 psf								
r / D	+0°	+10°	+20°	+30°	+45°	+60°	+75°	+90°
0.58	0.307	0.217	-0.100	-1.175	-1.528	-3.053	-3.977	-3.713
0.70	0.176	0.099	-0.122	-0.443	-1.070	-1.730	-2.192	-2.210
0.75	0.123	0.058	-0.131	-0.416	-0.954	-1.538	-1.943	-1.992
0.80	0.078	0.016	-0.150	-0.406	-0.865	-1.387	-1.745	-1.800
0.90	-0.011	-0.048	-0.193	-0.395	-0.754	-1.175	-1.459	-1.525
1.00	-0.068	-0.108	-0.212	-0.356	-0.688	-1.022	-1.266	-1.216
1.20	-0.153	-0.183	-0.267	-0.390	-0.597	-0.842		
1.40	-0.208	-0.229	-0.286	-0.372	-0.538	-0.728	-0.851	-0.814
1.60	-0.235	-0.242	-0.301	-0.374	-0.514	-0.650	-0.733	-0.778
1.80	-0.246	-0.263	-0.302	-0.371	-0.484	-0.573	-0.670	-0.691
2.00	-0.250	-0.263	-0.297	-0.348	-0.447	-0.513	-0.606	-0.617
2.25	-0.240	-0.253	-0.291	-0.326		-0.498	-0.557	-0.572
2.50	-0.235	-0.256	-0.270	-0.297	-0.373	-0.452	-0.505	-0.527
2.75	-0.234	-0.234	-0.238	-0.282	-0.348	-0.412	-0.463	-0.483
3.00	-0.210	-0.221	-0.240	-0.264	-0.326	-0.386	-0.428	
3.25	-0.180	-0.201	-0.219	-0.250	-0.302	-0.354	-0.394	-0.408
3.50	-0.194	-0.181	-0.217		-0.282	-0.332	-0.365	-0.377
3.75	-0.195	-0.183	-0.189	-0.201	-0.259	-0.313	-0.330	-0.351
4.00	-0.170	-0.172	-0.178	-0.209	-0.250	-0.287	-0.316	-0.327
5.00	-0.123	-0.145	-0.152	-0.157	-0.188		-0.247	-0.257
5.50	-0.142	-0.138	-0.127	-0.128	-0.166	-0.191	-0.220	-0.231
6.00	-0.129	-0.131	-0.114	-0.133	-0.148	-0.172	-0.195	-0.208

r / D	+90°	+105°	+120°	+135°	+150°	+160°	+170°	+180°
0.58	-3.713	-3.090	-1.427	-0.903	-0.736	-0.643	-0.579	-0.563
0.70	-2.210	-1.831	-1.184	-0.816	-0.721	-0.644	-0.547	-0.493
0.75	-1.992	-1.660	-1.052	-0.774	-0.688		-0.530	-0.492
0.80	-1.800	-1.503	-0.997	-0.727	-0.617	-0.450	-0.478	-0.466
0.90	-1.525	-1.296	-0.881	-0.615	-0.550		-0.324	-0.387
1.00	-1.216	-1.139	-0.794	-0.539	-0.451	-0.384	-0.273	-0.287
1.20			-0.650	-0.437	-0.329		-0.248	-0.217
1.40	-0.814		-0.570		-0.301	-0.231	-0.134	-0.163
1.60	-0.778	-0.701	-0.492	-0.309	-0.217	-0.186	-0.098	-0.121
1.80	-0.691	-0.608	-0.432	-0.270		-0.147	-0.058	-0.095
2.00	-0.617	-0.557	-0.393	-0.231	-0.160	-0.125	-0.049	-0.095
2.25	-0.572	-0.528	-0.414	-0.257	-0.184	-0.149	-0.096	-0.074
2.50	-0.527	-0.480	-0.381	-0.239	-0.161	-0.132	-0.088	-0.058
2.75	-0.483	-0.442	-0.352	-0.215	-0.137	-0.111	-0.077	-0.052
3.00		-0.405	-0.315	-0.201	-0.115	-0.098	-0.061	-0.043
3.25	-0.408		-0.299	-0.191	-0.104	-0.083	-0.056	-0.032
3.50	-0.377	-0.352	-0.278	-0.180	-0.084	-0.075	-0.047	-0.026
3.75	-0.351	-0.331	-0.264	-0.164	-0.082	-0.068	-0.042	-0.019
4.00	-0.327		-0.251	-0.156	-0.071	-0.057	-0.036	-0.018
5.00	-0.257	-0.247		-0.124	-0.040	-0.027	-0.014	0.006
5.50	-0.231		-0.184	-0.111	-0.034	-0.020	-0.004	0.014
6.00	-0.208	-0.190	-0.167	-0.103	-0.030	-0.008	0.001	0.014

Table 3.13 Pressure transducer accuracy

Transducer Full Scale

in. H2O	69.253	20	10
psi	2.5	0.72199	0.36100
psf	360	103.967	51.983

Transducer uncertainty by transducer full scale

R *	Mach Jet *	q (psf)	uncert. p 2.5psi (±psf)	uncert. p 20 in. (±psf)	uncert. p 10 in. (±psf)	uncert. Cp 2.5psi (±Cp)	uncert. Cp 20 in. (±Cp)	uncert. Cp 10 in. (±Cp)
4	0.50	24.21	0.360	0.104	0.052	0.0149	0.0043	0.0021
4	**0.74**	**54.26**	0.360	0.104	0.052	**0.0066**	**0.0019**	**0.0010**
6	0.50	10.82	0.360	0.104	0.052	0.0333	0.0096	0.0048
6	0.74	24.62	0.360	0.104	0.052	0.0146	0.0042	0.0021
6	**0.91**	**39.12**	0.360	0.104	0.052	**0.0092**	**0.0027**	**0.0013**
8	0.50	6.08	0.360	0.104	0.052	0.0592	0.0171	0.0085
8	0.74	13.71	0.360	0.104	0.052	0.0263	0.0076	0.0038
8	**0.91**	**21.98**	0.360	0.104	0.052	**0.0164**	**0.0047**	**0.0024**
12	0.50	2.71	0.360	0.104	0.052	0.1328	0.0384	0.0192
12	0.74	6.24	0.360	0.104	0.052	0.0577	0.0167	0.0083
12	**0.91**	**9.71**	0.360	0.104	0.052	**0.0371**	**0.0107**	**0.0054**
					Average:	**0.0371**	**0.0107**	**0.0054**
					Avg,R best:	**0.0173**	**0.0050**	**0.0025**

```
      PROGRAM ldvall
c
c   11 15 92   1042 pm Robert F. Dennis
*************************************************************************
* filename: LDVALL6.FOR     adapted for jetdata with init data
* THIS PROGRAM IS DESIGNED TO READ THE FIRST 15 LINES OF TEXT OF EACH
* DATA FILE GENERATED WITH THE LDV SYSTEM, calc velocity, read traverse
* locations from both initfile and runfile,and read swits data from
* file SWITSLIST.DAT   note: only for initfiles 0 to 99 (inn*2)
*  recalc sample statistics ---feet per sec --
*    output filemame is: ldvlist**to**.dac
*        compact file form  lines 0 and 1 only
*          excludes samps for both deviation and zero f
*           -separate zeri filter
*        eliminates most runtime messages (for speed)
*************************************************************************
      CHARACTER FILENAM*11,R*1,RUN*3,P*1,PNT*2,DAT*4,B*2,BAK*2
      CHARACTER  initnam*10, inn*2,init*4,opt*1,dac*4
      character ldvnam*17,ldvh*7 ,to*2,firstr*2,lastr*2
      character rem1*58,rem2*58,rem3*58,date*16,time*16
c
      integer nchan,idbs,ico(3),indchan
      integer nbad1(3),nd1(3),nbad2(3),nd2(3)
     #        ,nbadz(3),ndz(3)
c
      real incrm, mjet
      real f(1000,3),fd(1000,3)
c
      real dmsv(3)
c
      real   v(1000,3)
     #    ,vgz(1000,3),vbadz(1000,3)
     #    ,vg1(1000,3),vbad1(1000,3)
     #    ,vg2(1000,3),vbad2(1000,3)
c
      real delx(3),ndata(3)
     #      ,ztol,kdev1,kdev2
c
      real  vavg0(3),vdev0(3),vhi,vlo
     #     ,vavgz(3),vdevz(3)
     #     ,vavg1(3),vdev1(3)
     #     ,vavg2(3),vdev2(3),vdevn(3)
c
      real fdavg0(3),fmavg0(3)
     #    ,fdavgz(3),fmavgz(3)
     #    ,fdavg1(3),fmavg1(3)
     #    ,fdavg2(3),fmavg2(3)
c
       DIMENSION  X(4), Y(4), Z(4),ICLC(4),DMDIR(4)
       dimension xt(4),yt(4),zt(4),xc(11),yc(11),zc(11)
c
      LOGICAL CHECK
c
      DATA P,R,DAT,B, init /'P','R','.DAT','.B','init'/
      data ldvh, to, dac  / 'ldvlist', 'to', '.dac' /

c=============initial values============================
      ifirst = 27
```

```
      ilast  = 27
c
      lastpnt= 15
c
      lastbak= 4
c---meas.freq and deviation tolerances--
        ztol = .5
        kdev1 = 4.0
        kdev2 = 3.0
c======== imputs =========
 810   format(/,1x,'PROGRAM LDVALL.FOR - ldv/swits data log'
     #       ,//,1x,' enter first run:')
 815   format(i3)
 820   format(/,'  enter last run:')
 825   format(/,'  enter new parameters? y ro n:')
 827   format(a1)
 830   format(/,'  enter first deviation limit(4.0):')
 835   format(f5.2)
 840   format(/,'  enter second dev limit(3.0):')
 850   format(/,'  enter maximum point numb.(15):')
 860   format(/,'  enter maximum backup numb.(4):')
c
       write(*,810)
        read(*,815) ifirst
       write(*,820)
        read(*,815) ilast
c
       write(*,825)
        read(*,827) opt
       if((opt.eq.'Y').or.(opt.eq.'y')) then
c           -------------------
            write(*,830)
             read(*,835)  fin
             if(fin.ne.0) kdev1=fin
            write(*,840)
             read(*,835)  fin
             if(fin.ne.0) kdev2=fin
            write(*,850)
             read(*,815)  iin
             if(iin.ne.0) lastpnt=iin
            write(*,860)
             read(*,815)  iin
             if(iin.ne.0) lastbak=iin
c           -------------------
       endif
c
890     continue
        print*,'parameters are:'
        write(*,*) kdev1,kdev2,lastpnt,lastbak
c
c=========================
C - conversion factors ----
      pi = 3.141593
C--------counters-----------
      jjj = 0
      flag1 = 0
c==============start output list======================
c
```

```
       WRITE(firstr,'(I2)') ifirst
       WRITE(lastr ,'(I2)') ilast
       ldvnam = ldvh//firstr//to//lastr//dac
c
       print*,' ----START FILE PROCESSING---'
        OPEN(UNIT=9,FILE=ldvnam,STATUS='NEW',recl=460)
c
ccc        OPEN(UNIT=9,FILE=ldvnam,STATUS='NEW',
ccc     #FORM='FORMATTED',RECL=430,ACCESS='SEQUENTIAL')
c
C----------- heading----------------------------
 710  format(1X,'file: ',a17,' for  LDV runs ',i2,' to ',i2
     #      ,' - tabular data ;ldv and swits',/)
c
      write(9,710) ldvnam,ifirst,ilast
c -----------colm.labels-----------------------------
cNote:label format 720 is with list colm.write stms.for clarity
        write(9,720)
           print*,' labels written'
c
c%%%%%%%%%%%%%%%%%%% input data %%%%%%%%%%%%%%%%%%%%%%%%%%%
c%%%%%%%% run loop %%%%%%%%%%%%%%%%%%%%%%%%%%%%%%%%%%%%%%
c
      DO 50 IR = ifirst,ilast
c
        IRUNUM = IR
        WRITE(RUN,'(I3)') IRUNUM
c
c    ************************************************
c    ********************* read init file **************
c
            write(inn,'(i2)') irunum
            initnam = init//inn//dat
              CHECK=.TRUE.
 12           format(1x,'testing for ',a10)
            write(*,12) initnam
              INQUIRE(FILE=INITNAM,EXIST=CHECK)
              if (.NOT.CHECK) then
                print*,' no such initfile'
                GO TO 41
              endif
cgoto
            OPEN(UNIT=11,FILE=initnam,STATUS='OLD',recl=350)
c           ------------------
 301         format(//,19x,i2)
 303         format(///,6x,a58,////,6x,a58,/,6x,a58)
 304         format(/////,9x,f8.3,2x,f8.3,2x,f8.3,//
     #        ,9x,f8.3,2x,f8.3,2x,f8.3)
 305         format(t29,f7.3)
 306         format(t43,i1,1x,i1,1x,i1)
            read(11,301)infr
            read(11,303)rem1,rem2,rem3
            read(11,304) Xt(1),Yt(1),Zt(1), Xt(3),Yt(3),Zt(3)
            read(11,305)incrm
            read(11,306) iac1,iac2,iac3
              indchan = iac1+iac2+iac3
            read(11,306) ico(1),ico(2),ico(3)
              indcoin = ico1+ico2+ico3
```

```
c
             CLOSE(UNIT=11,STATUS='KEEP')
              print*,' ----INITFILE READ----'
c           ===========calc. incr. components=============
             xlen = xt(3)-xt(1)
             ylen = yt(3)-yt(1)
             zlen = zt(3)-zt(1)
             tlen = sqrt( xlen**2 + ylen**2 + zlen**2 )
             rinc = sqrt( (incrm/tlen)**2 )
             xinc = rinc*xlen
             yinc = rinc*ylen
             zinc = rinc*zlen
             cjinc = sqrt( ( tlen/incrm )**2 )
             jinc = int(cjinc)
c            ============================================
              xc(1) = Xt(1)
              yc(1) = Yt(1)
              zc(1) = Zt(1)
               do 68    jj = 2, jinc+1
                  xc(jj) = Xt(1)+(jj-1)*xinc
                  yc(jj) = Yt(1)+(jj-1)*yinc
                  zc(jj) = Zt(1)+(jj-1)*zinc
  68           continue
              xc(jinc+2) = Xt(3)
              yc(jinc+2) = Yt(3)
              zc(jinc+2) = Zt(3)
              ntpnt = jinc+2
c           =========if no initfile for run===========
  41       continue
c
C%%%%%%%%%%%%%%%%%% point loops %%%%%%%%%%%%%%%%%%%%%%%%%%%%%%%%
c
          imseq = 0
          itpnt = 0
c
          DO 45 IP = 1,lastpnt
c
             IPTNUM = IP
             WRITE(PNT,'(I2)') IPTNUM
C
             DO 43 IB = 1,lastbak
                 IBAK = IB - 1
                 WRITE(BAK,'(I2)') IBAK
c
c    ************************************************
c    ********************* read point file **************
C
       IF (IBAK.EQ.0) THEN
          FILENAM = R//RUN//P//PNT//DAT
       ELSE
          FILENAM = R//RUN//P//PNT//B//BAK
       ENDIF
C
          IF (FILENAM(2:2).EQ.' ') FILENAM(2:2) = '0'
          IF (FILENAM(3:3).EQ.' ') FILENAM(3:3) = '0'
          IF (FILENAM(6:6).EQ.' ') FILENAM(6:6) = '0'
          IF (FILENAM(10:10).EQ.' ') FILENAM(10:10) = '0'
C
```

```
 13      format(1x,'testing for ',a11)
cbob          write(*,13) filenam
c-------------- test existance --------------
           CHECK=.TRUE.
           INQUIRE(FILE=FILENAM,EXIST=CHECK)
           IF (.NOT.CHECK) then
ccc             print*,'no such pointfile'
             GO TO 42
cgoto
           ENDIF
c---------------- if pointfile exists -----
c
          imrun=irunum
          imseq=imseq+1
          impnt=iptnum
          imbak=ibak
          if(ibak.eq.0) itpnt=itpnt+1
c
          imxseq=imseq
          imxpnt=iptnum
          imxbak=ibak
c
          i2wrt = 0
c
         OPEN(UNIT=8,FILE=FILENAM,STATUS='OLD')
c ================= read point data     =============
 600     FORMAT (//,10X,I4,6X,I4,8X,I4,8X,2(I2,1H/),I4,8X,2(I2,1H:),
     #I2,/)
 610     FORMAT (36X,F8.3,7X,F8.3,7X,F8.3)
 615     FORMAT (35X,F8.3,7X,F8.3,7X,F8.3)
 620     FORMAT (/,18X,I5)
 630     FORMAT (36X,I4,//)
c
cc 640     FORMAT (1X,I3,2F9.1,4X,F5.1,F9.2,F6.1,F10.3,F11.1,I9)
c
 640     FORMAT (t36,F5.2)
c
 650     format(/////,/////,////)
 660     format(t26,3(f7.2,1x))

           READ(8,600) ITEST,IRUN,IPT,IMON,IDAY,IYR,IHR,IMIN,ISEC
           READ(8,610) X(1),Y(1),Z(1)
           READ(8,615) X(2),Y(2),Z(2)
           READ(8,610) X(3),Y(3),Z(3)
cc              write(*,*) x(3),y(3),z(3)
           READ(8,620) IDBS
           READ(8,630) NCHAN
               if(nchan.ne.indchan) then
               print*,'NOTE: indchan/nchan mismatch, see below:'
               write(*,*) indchan, nchan
               else
cbob               print*,' channel number match'
               endif
          DO 30 J = 1,NCHAN
           READ(8,640)dmsv(j)
cc              print*,'downmix is:'
ccc              write(*,*) dmsv(J)
c
```

```
  30     CONTINUE
ccc         print*,'reading freq values for idbs ='
ccc             write(*,*) idbs
c
          read(8,650)
          do 31 i = 1,idbs
             READ(8,660) f(i,1),f(i,2),f(i,3)
c           check first,last 2
cc             if((i.lt.3).or.(i.gt.(idbs-2)))
cc     #          write(*,*) i,f(i,1),f(i,2),f(i,3)
  31      continue
c-------------------------
cbob             print*,'point data read'
            CLOSE(UNIT=8,STATUS='KEEP')

c%%%%%%%%%%%%%%%  stand dev + bad samples %%%%%%%%
C--- note: vbad(j) must be reset out of chan loop(memory)-
        do 36 j = 1,nchan
        do 37 n = 1 ,idbs
           vbadz(N,J)     = 0
             vgz(n,j)     = 0
           vbad1(N,J)     = 0
             vg1(n,j)     = 0
           vbad2(N,J)     = 0
             vg2(n,j)     = 0
  37    continue
  36    continue
c
C***************** channel loop ***************
       DO   25   J  =  1,  NCHAN
         NBADz(J)      =  0
         NBAD1(J)      =  0
         NBAD2(J)      =  0
         NDATA(J)     =  0
         vSUM         =  0
c
c================ various samples loops -==========
C        -- velocity conversion ------
            delx(1) = +18.83
            delx(2) = -17.60
            delx(3) = -19.72
c
         do 15   n = 1,idbs
           fd(n,j) =  f(n,j)-40+dmsv(j)
            v(n,j) = (fd(n,j)*delx(j))/.3048
  15     continue
c        ----- raw (0) v average + reset ---------
         vSUM         =  0
         DO    14   N  =  1, idbs
           vSUM          =  vSUM  +  v(N,J)
  14    CONTINUE
         vAVG0(J)      =   vSUM / idbs
            if(j.eq.1) then

           write(*,*) vavg0(j)
            endif
c        ------ 0 stand dev --------
         vSUMD        =  0
```

```
        DO   16   N  =  1,  idbs
          vSUMD       =  vSUMD + ( v(N,J) - vAVG0(J))**2
   16   CONTINUE
c
            vdev0(j)=sqrt(vsumd/idbs)
c------------
           if(j.eq.1) then
           print*,'dev0=:'
           write(*,*) vdev0(j)
           endif
c===========zero filter================
c       --------- exclude  zero f samples-------
        NBADz(J)      =  0
        DO   69   N  =  1,  idbs
c                --- this chan ---
          IF ( f(n,j).lt.ztol )   THEN
            vBADz(N,J)  =  1
            NBADz(J)    =  NBADz(J) + 1
          ENDIF
cbb               --- other chan if coin---
cbb          DO   68   K  =  1,  NCHAN
cbb            IF ( K.EQ.J )    GO TO 18
cbb            IF ( ico(J).EQ.1.AND.vBADz(N,J).EQ.1 )   THEN
cbb                 IF  ( ico(K).EQ.1 )    vBADz(N,K)  =  1
cbb            ENDIF
cbb   68     CONTINUE
c              -------
   69   CONTINUE
           if(j.eq.1) then
           print*,'nbadz=:'
           write(*,*) nbadz(j)
           endif

C       ---------- calc z mean dopp freq.-----------
        NDATA(J)    =  0
        SUMv     =  0
        DO   70   N  =  1,  idbs
          IF  (vBADz(N,J).EQ.0)   THEN
            NDATA(J)   = NDATA(J) + 1
            SUMv       =  SUMv + v(N,J)
            vgz(ndata(j),j) = v(n,j)
          ENDIF
   70   CONTINUE
        ndz(j) = ndata(j)
cc              write(*,*) ndz(j)
        if (ndz(j).gt.0) then
            vavgz(J)   =  sumv/ ndz(j)
        else
            vavgz(j) = 0
        endif
           if(j.eq.1) then
           print*,'uavgz=:'
          write(*,*) vavgz(j)
           endif
c
c       ------ z stand dev --------
        vSUMD       =  0
        DO   71   N  =  1,  ndz(j)
```

```
          vSUMD      =  vSUMD + ( vgz(N,J) - vAVGz(J) )**2
   71   CONTINUE
c
        if (ndz(j).gt.0) then
            vdevz(J) = SQRT(vsumd/ndz(j))
         else
            vdevz(j) = 99.99
         endif
c
c         -----------
          if(j.eq.1) then
          print*,'devz=:'
          write(*,*) vdevz(j)
          endif
c       ========== 1st (a) filtering ==========
c       ---1st hi-lo limits --------
        vhi = vAVG0(J) + kdev1*vDEVz(J)
        vlo = vAVG0(J) - kdev1*vDEVz(J)
c       --------- exclude bad samples-------
        NBAD1(J)     =  0
        DO   19   N  =  1,  ndz(j)
c                --- this chan ---
        IF ( v(N,J).GT.vHI .OR. v(N,J).LT.vLO )   THEN
cc          IF ((v(N,J).GT.vHI).OR.(v(N,J).LT.vLO).OR.
cc     #         (f(n,j).lt.ztol))   THEN
            vBAD1(N,J)  =  1
            NBAD1(J)    =  NBAD1(J) + 1
          ENDIF
cbb               --- other chan if coin---
cbb           DO   18   K  =  1,  NCHAN
cbb             IF ( K.EQ.J )    GO TO 18
cbb             IF ( ico(J).EQ.1.AND.vBAD1(N,J).EQ.1 )   THEN
cbb                  IF  ( ico(K).EQ.1 )    vBAD1(N,K)  =  1
cbb             ENDIF
cbb   18      CONTINUE
c               -------
   19   CONTINUE
           if(j.eq.1) then
           print*,'nbad1=:'
           write(*,*) nbad1(j)
           endif

C       ---------- calc 1 mean dopp freq.-----------
        NDATA(J)    =  0
        SUMv     =  0
        DO   20   N  =  1,  ndz(j)
          IF  (vBAD1(N,J).EQ.0)   THEN
            NDATA(J)   = NDATA(J) + 1
            SUMv       =  SUMv + v(N,J)
            vg1(ndata(j),j) = v(n,j)
          ENDIF
   20   CONTINUE
        nd1(j) = ndata(j)
cc             write(*,*) nd1(j)
        if (nd1(j).gt.0) then
            vavg1(J)   =  sumv/ nd1(j)
        else
            vavg1(j) = 0
```

```
        endif
cc           if(j.eq.1) then
cc           print*,'uavg1=:'
cc          write(*,*) vavg1(j)
cc           endif
c       ------ 1 stand dev --------
        vSUMD       =  0
        DO   21   N  =  1,  nd1(j)
          vSUMD      =  vSUMD + ( vg1(N,J) - vAVG1(J) )**2
   21   CONTINUE
c
        if (nd1(j).gt.0) then
            vdev1(J) = SQRT(vsumd/nd1(j))
         else
            vdev1(j) = 99.99
         endif
c
C     ====== 2nd filtering ============================
        vhi =  vAVG1(J) + kdev2*vDEV1(J)
        vlo =  vAVG1(J) - kdev2*vDEV1(J)
c       --------- exclude bad samples ---------------
        NBAD2(J)     =  0
        DO   17   N  =  1,  nd1(j)
          IF (vg1(N,J).GT.vHI.OR.vg1(N,J).LT.vLO)   THEN
            vBAD2(N,J)  =  1
            NBAD2(J)    =  NBAD2(J) + 1
          ENDIF
c           ----
c          DO   22   K  =  1,  NCHAN
c            IF ( K.EQ.J )    GO TO 22
c            IF ( ico(J).EQ.1.AND.vBAD2(N,J).EQ.1 ) THEN
c                  IF  ( ico(K).EQ.1 )    vBAD2(N,K)  =  1
c            ENDIF
c   22      CONTINUE
c           ----
   17   CONTINUE
cc           if(j.eq.1) then
cc           print*,'nbad2=:'
cc           write(*,*) nbad2(j)
cc           endif

C       ---------- 2 calc mean v.-----------
        NDATA(J)    =  0
        SUMv     =  0
        DO   23   N  =  1,  nd1(j)
          IF  (vBAD2(N,J).EQ.0)   THEN
            NDATA(J)   = NDATA(J) + 1
            SUMv       =  SUMv + vg1(N,J)
            vg2(ndata(j),j) = vg1(n,j)
          ENDIF
   23   CONTINUE
        nd2(j) = ndata(j)
cc            write(*,*) nd2(j)
        if (nd2(j).gt.0) then
            vAVG2(J)   =  SUMv/ nd2(j)
        else
            vavg2(j) = 0
        endif
```

```
cc            if(j.eq.1) then
cc           print*,'uavg2=:'
cc            write(*,*) vavg2(j)
cc            endif

c        ------ 2 stand dev --------
         vSUMD        =  0
         DO   24    N  =  1,  nd2(j)
           vSUMD      =  vSUMD + ( vg2(N,J) - vAVG2(J) )**2
    24   CONTINUE
          if (nd2(j).gt.0) then
             vdev2(J) = SQRT(vsumd/nd2(j))
          else
             vdev2(j) = 99.99
          endif
c        ---------normalized-----
           if(abs(vavg2(j)).gt.(.01)) then
              vdevn(j)=vdev2(j)/abs(vavg2(j))
           else
              vdevn(j)= 8.888
           endif
           if (vdevn(j).ge.10) vdevn(j)=9.999
c
cc            if(j.eq.1) then
cc            print*,'dev2=:'
cc            write(*,*) vdev2(j),vdevn(j)
cc            endif

c        ========= fmavg calc.======================
             fdavg0(j)= vavg0(j)*.3048/delx(j)
             fmavg0(j)=fdavg0(j)+40-dmsv(j)
             fdavg1(j)= vavg1(j)*.3048/delx(j)
             fmavg1(j)=fdavg1(j)+40-dmsv(j)
             fdavg2(j)= vavg2(j)*.3048/delx(j)
             fmavg2(j)=fdavg2(j)+40-dmsv(j)
c
cc            if(j.eq.1) then
cc            print*,'fmavg0=:'
cc            write(*,*) fmavg0(j)
cc            endif

c====================== end sample loops =======
   25 CONTINUE
C***************** end channel loop ***************
c
c%%%%%%%%%%% find and read switslist data for ldv point %%%%%%%%%
c
         OPEN(UNIT=11,FILE='switslist.dat',STATUS='OLD',recl=450)
cbob          print*,'start swits search'
c         ========= run search ==========
 400      format(//)
          read(11,400)
c
         do 404 is = 1,130
 402      format(t5,i3,t10,I3)
          read(11,402,err=405) isrun,isseq
cc              write(*,*) isrun,isseq,ir
          if(isrun.eq.IR) go to 406
```

```
 404      continue
 405      print*,'no such switsrun'
          go to 42
cgoto
 406      continue
c         ======= point search ============
ccc              print*,'point search'
               itldv=60* ihr+ imin
          if(isec.ne.0) itldv=itldv+1
c
         do 416 is = 1,15
c--------------------loop--------
 410      format( t5, i3  , t10, i3
     #           ,t25, i3  , t30, i3
     #           ,t50, f9.3, t70, f9.3
     #           ,t80, f9.3, t90, f9.3)
c
cc          read(11,410) isrun,isseq
           read(11,410,err=420) isrun,isseq
     #                          ,ishr,ismin
     #                          ,rjet,mjet
     #                          ,vtun,vjet
cc          write(*,*) isrun,isseq,ishr,ismin
cc          write(*,*) rjet,mjet,vtun,vjet
c
cc          write(*,*) is, ishr,ismin

c        --------tests------------
         if(isrun.gt.IR) then
cbob              print*,'end of run'
              go to 417
         endif
c
              itswt=60*ishr+ismin
         if(itswt.ge.itldv) then
cbob              print*,'later swits'
              go to 417
         endif
c       ----replace old values----
           iosseq=isseq
           iohr=ishr
           iomin= ismin
           iotswt=itswt
           orjet=rjet
           omjet=mjet
           ovtun=vtun
           ovjet=vjet
c
c         -------endloop------
 416      continue
           go to 418
c-------------pos test----
 420       print*,'end of switslist'
 417      continue
ccc             print*,'switspoint found'
c

c
```

```
            idts = itldv-iotswt
cc            write(*,*) itldv,iotswt,idts
            if(idts.lt.1) print*,'data time close'
c
            go to 419
c----------------------
 418         print*,'switspoint NOT found'
c           ======================================
 419         CLOSE(UNIT=11,STATUS='KEEP')
c
c%%%%%%%%%%%%%%%%%% write ldv output list%%%%%%%%%%%%%
c
c    -----column label format (written before run loop)---
 720     format(1x,'id,',t5,'  datafile,'
     #         ,t16,' run ,:,'
     #         ,t25,'msq,mpt,mbk,tsq,:,'
     #         ,t45,'mxs,mxp,mxb,uft,:,'
     #         ,t65,'hr, min,sec,:,'
     #         ,t80,' x loctn, y loctn, z loctn,:,'
     #        ,t110,'swsq, Rjet , Mjet , Vtun , Vjet ,:,'
     #        ,t150,'samp,'
     #        ,t155,'tolA,tolB,co2,co4,co6,:,'
c
cc      #        ,t180,' Uo (fps), Ua (fps), Ub (fps),'
cc      #        ,t210,'Udevo,Udeva,Udevb,bada,badb,'
cc      #        ,t240,' ndev, FmUo, FmUa, FmUb,:,'
c
     #        ,t180,'Uo;fps,Uz;fps,Ua;fps,Ub;fps,'
     #        ,t208,'Udevo,Udevz,Udeva,Udevb,badz,bada,badb,'
     #        ,t247,'  FmUo,FmUz,FmUa,FmUb,'
c
     #        ,t270,'Wo;fps,Wz;fps,Wa;fps,Wb;fps,'
     #        ,t298,'Wdevo,Wdevz,Wdeva,Wdevb,badz,bada,badb,'
     #        ,t337,'  FmWo,FmWz,FmWa,FmWb,'
c
     #        ,t360,'Vo;fps,Vz;fps,Va;fps,Vb;fps,'
     #        ,t388,'Vdevo,Vdevz,Vdeva,Vdevb,badz,bada,badb,'
     #        ,t427,'  FmVo,FmVz,FmVa,FmVb,'
c
     #        ,t450,'end')
c
c    -------first run line format (id=0) ----------
 730     format(1x,i1,', ',t5,9x,', '
     #         ,t16,i3,',:')
c
c    -------full list primary format (id=1)---------
c               -- datafile id--
 740     format(1x,i1,', ',t5,a11,', '
     #         ,t17,i3,',:, '
c               --sequence data--
     #         ,t25,4(  i2,', '),':,'
c               --run summary--
ccc      #        ,t45,4(  i2,', '),':,'
     #         ,t45,' , , , ,:,'
c               --time--
     #         ,t65,3(  i2,', '),':,'
c               --location--
     #         ,t80,3(f7.3,', '),':,'
```

```
c                --swits--
     #          ,t110,i3,',',t115,4(f6.2,',') ,':,'
c                --ldv param--
     #          ,t150,i4,','
     #          ,t155,2(f3.1,', '),3(i2,', '),':,'
c                --chan 2.ldv data+stats--
c
cc     #          ,t180,3(f8.2,', ')
cc     #          ,t210,3(f6.2,','),i4,',',i3,','
cc     #          ,t240,f5.3,',',3(f5.3,','),':,'
c
     #          ,t180,4(f7.2,',')
     #          ,t212,4(f6.2,','),i3,',',i2,',',i2,','
     #          ,t250,4(f4.2,',')
c
c                --chan 4--
     #          ,t270,4(f7.2,',')
     #          ,t302,4(f6.2,','),i3,',',i2,',',i2,','
     #          ,t340,4(f4.2,',')
c                --chan 6--
     #          ,t360,4(f7.2,',')
     #          ,t392,4(f6.2,','),i3,',',i2,',',i2,','
     #          ,t430,4(f4.2,',')
     #          ,t450)
c
c    -------- point summary format (id=2)-(line 43)----
 750    format(1x,i1,', ',t5,9x,', '
     #          ,t16,i3,',:, '
     #          ,t25,2(2x,', ',i2,', '),':,'
     #          ,t45,2(2x,', '),i2,', ,:')
c
c    -------- run summary format (id=3)--(line 45)-----
 760    format(1x,i1,', ',t5,9x,', '
     #          ,t16,i3,',:, '
     #          ,t25,' , , , ,:,'
     #          ,t45,2(i2,', '),2x,', ',i2,',:')
c
c============== write list ========================
cc          print*,'start datapoint write'
c
c---write new run line---------------
        if(iflag1.eq.0) then
          id = 0
ccc          write(9,730) id,irunum
          iflag1 = 1
        endif
c
c----correct runfile traverse info---
         if(irunum.ge.42) then
            xtt = x(2)
            ytt = y(2)
            ztt = z(2)
         else
            xtt = xc(itpnt)
            ytt = yc(itpnt)
            ztt = zc(itpnt)
         endif
c
```

```
c---full  i/o list----------------------
      id = 1
      write(9,740) id,filenam
     #             ,irunum
     #             ,imseq,impnt,imbak,itpnt
ccc     #             ,imxseq,imxpnt,imxbak,iufp
     #             ,ihr,imin,isec
     #             ,xtt,ytt,ztt
     #             ,iosseq,orjet,omjet,ovtun,ovjet
     #             ,idbs
     #             ,kdev1,kdev2,ico(1),ico(2),ico(3)
c
cc     #             ,vavg0(1), vavg1(1), vavg2(1)
cc     #             ,vdev0(1), vdev1(1), vdev2(1)
cc     #                      , nbad1(1), nbad2(1)
cc     #             ,vdevn(1),fmavg0(1),fmavg1(1),fmavg2(1)
c
     #            , vavg0(1), vavgz(1), vavg1(1), vavg2(1)
     #            , vdev0(1), vdevz(1), vdev1(1), vdev2(1)
     #                      , nbadz(1), nbad1(1), nbad2(1)
     #            ,fmavg0(1),fmavgz(1),fmavg1(1),fmavg2(1)
c
     #            , vavg0(2), vavgz(2), vavg1(2), vavg2(2)
     #            , vdev0(2), vdevz(2), vdev1(2), vdev2(2)
     #                      , nbadz(2), nbad1(2), nbad2(2)
     #            ,fmavg0(2),fmavgz(2),fmavg1(2),fmavg2(2)
c
     #            , vavg0(3), vavgz(3), vavg1(3), vavg2(3)
     #            , vdev0(3), vdevz(3), vdev1(3), vdev2(3)
     #                      , nbadz(3), nbad1(3), nbad2(3)
     #            ,fmavg0(3),fmavgz(3),fmavg1(3),fmavg2(3)

c
c%%%%%%%%%%%%%%%%%%%% end list write%%%%%%%%%%%%%%%%%%%%
c
 250    FORMAT (1X,'--- FILE ',A11,' COMPLETED')
        WRITE(*,250) FILENAM
        jjj = jjj+1
c
c%%%%%%%%%%%%%%%%%%%% loop termination %%%%%%%%%%%%%%%%%
  42    continue
c========== end nopointfile bypass ====
  43    continue
c============= end backup loop ========
c--write point summary----
c
        id = 2
        if(i2wrt.eq.0) then
ccc           write(9,750) id,irunum
ccc     #            ,impnt,itpnt
ccc     #            ,imxbak
          i2wrt=1
        endif
c
c----------------
  45    continue
c================== end point loop ====
        iflag1 = 0
```

```
c--write run summary-------
      iufp = ntpnt-itpnt
      id = 3
      write(9,760) id,irunum
     #            ,imxseq,imxpnt,iufp
c
c----------------
  50    CONTINUE
c================= end run loop =======
       CLOSE(UNIT=9,STATUS='KEEP')
c
  994    format(1x,'----JOB DONE: ',i3,' files completed----')
       WRITE(*,994) jjj
 995    format(1x,'saved outputfile: ',a17)
       write(*,995) ldvnam
       STOP
C%%%%%%%%%%%%%%%%%%%%%%%%%%%%%%%%%%%%%%%%%%%%%%%%%%%%%%%%%%%%
       END
```

Chapter 1

Introduction 1.0

The System 8400 is a unique data acquisition system offering a turnkey solution to pressure measurement while accepting analog, frequency, and digital signals from a variety of other sensing devices. This allows total integration of pressure, temperature, flow and various other parameters within one system to provide a common data path to the host computer. Pressure measurement is facilitated by multi-channel pressure sensing modules (Electronic Pressure Scanners) integral to the configuration, and complemented by On-Line Calibration and digital compensation operations to provide high accuracy measurement of both air and liquid pressures.

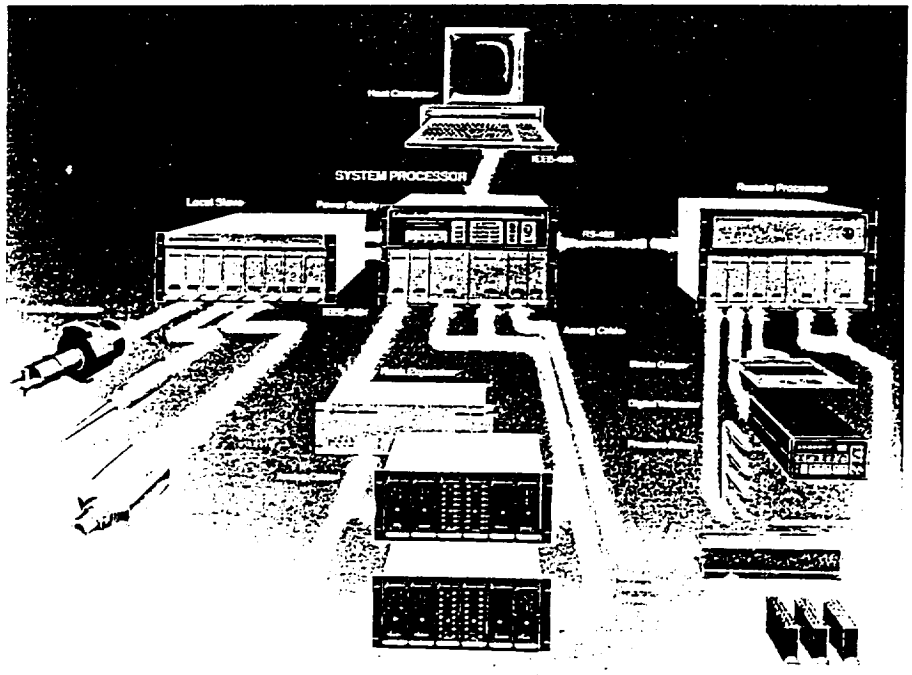

Figure 1.1: The System 8400

The System 8400 represents a new approach to data acquisition: a flexible system whose power and performance are a function of its configuration, and its configuration is determined by the customer's application(s).

The System is built on a parallel processing architecture to offer modularity, and high-speed data acquisition and reduction. Parallel processing frees the user from past technology, where performance was limited by a single A/D converter and one microprocessor.

The System has a master 32-bit microprocessor which controls up to 64 Input Units. Each Input Unit has a microprocessor and personality card(s) which define its function. A variety of Input Units allows the user to tailor his System to specific measurement and performance levels. The modular design permits entry-level Systems to be configured, and their performance can be enhanced later through expansion.

The System 8400 consists of one or more 19" rack mounted chassis, each capable of accepting up to eight Input Units. Each Input Unit digitizes input signals from devices such as electronic pressure scanners, discrete pressure transducers, thermocouples, flow meters, or most other analog or digital measurement devices.

The 8400 System Processor (SP) is the heart of the system, providing Input Unit control, data synchronization and processing, and host computer interfacing (IEEE-488). It has a VME chassis, MC68020 microprocessor, power supply, and Front Panel display. Should an application require more than eight Input Units, an 8400 SP can be expanded locally or remotely through expansion chassis.

Local expansion requires a Local Slave (LS) which has eight additional slots and communicates to the SP through the IEEE-488 interface. Up to seven Local Slaves can be attached to the SP.

Remote expansion is accomplished with the Remote Processor (RP) which has eight input slots. Up to four RP's may be interfaced to the SP through an RS-485 (RS-232C multidrop) communications link. The RP has its own power supply and may be expanded by adding LS's.

Input Units can be installed in an SP, LS, or RP to provide input capability for the System 8400. Maximum throughput performance is realized when the Input Units are housed in the SP.

The following Input Units are available:

1. Scanner Digitizer Unit (SDU)
2. Pressure Calibration Unit (PCU)
3. Pneumatic Input Unit (PIU)
4. Analog Input Unit (AIU)
5. Pressure Standard Unit (PSU)
6. Frequency Measurement Unit (FMU) (Available 1/92)
7. Digital Input Unit (DIU) (Available 1/92)

The Scanner Digitizer Unit (SDU) supports the electronic pressure scanners. Scanners have a transducer per port which permits high-speed electronic sampling of multiple pressures. The System's design permits parallel addressing and multiple SDU's for acquisition rates as high as 200,000 measurements per second. The System is capable of satisfying typical industrial applications or the most complex wind tunnel or gas turbine applications, yet it is simple to configure and operate. The System 8400 operates in a stand-alone mode as an independent instrument, or under the control of a host computer as part of a larger data acquisition system.

The System 8400 has a complete Front Panel display and keyboard (and an optional remote hand held display) to operate and diagnose each component. A series of menus leads the user through all system operations including initialization, calibration, data acquisition, and data display.

The host computer can be a small personal computer (PC) or any larger computer that supports the IEEE-488 standard interface. Control is primarily left to the SP, including scanning, multiplexing, timing, and data conversion, thus freeing the host to perform other functions. The host computer sends only high level commands, usually three characters plus parameters (i.e., channel numbers), and is signaled when the processor completes the operation and is ready to transmit data. PSI offers a start-up software package and a real-time data acquisition software package for controlling the System 8400 via an IBM-PC compatible computer with a National Instruments GPIB card. Contact the Applications Department at the factory for information on these software packages.

Version 3 is the latest version of System 8400 firmware and it offers improved performance and enhancements over Version 2 firmware. Some of the major new features are listed below:

1. Multitasking operation (Front Panel, Remote Display and host computer);
2. Enhanced Front Panel/Remote Display features;
3. Supports optional remote display;
4. Dynamic data buffering;
5. Data overflow protection; and,
6. Expanded data storage.

This manual is for installers, system operators, and programmers. Installation, cable hook-up, pneumatic hook-up, programming, and operations are detailed in this manual. Several examples, tables, photographs, and diagrams are presented as visual aides.

1.1 Features Of The System 8400

1. Pressure scanning up to 50,000 ch/sec. per SDU;
2. Raw data throughput up to 50,000 ch/sec.;
3. Engineering Units throughput up to 20,000 ch/sec.;
4. Up to 300,000 bytes per second data transfer (IEEE-488);
5. Memory expansion to 8 MByte;
6. Simple system configuration expansion;
7. Menu-driven Front Panel diagnostics;
8. Simplified computer control; and,
9. Flexible output formats.

1.2 System Specifications

Data Acquisition Rates:

Sequential Address Mode	20,000 measurements/second
Parallel Address Mode	50,000 measurements/second
Maximum (Using 4 SDU's)	200,000 measurements/second

System Throughput:	Up to 50,000 measurements/sec. (Binary Units) 20,000 Max measurements/sec. (Engineering Units)
Data Storage:	In excess of 1,000,000 measurements maximum
Interface:	IEEE-488 (300,000 bytes/sec.)
Software:	High level command language
Data Output Formats:	Signed Integer, ASCII, IEEE Floating Point and DEC, Engineering Units
Display:	40 Character Alphanumeric, Remote Hand-Held (Optional); Front Panel (Standard)
Power Requirements:	500 Watts Maximum

Physical Requirements:

Module	Height	Width	Depth	Weight
8400 SP	12.25" (31.12 cm)	19" (48.26 cm)	21" (53.34 cm)	40.5 lbs (18.4 kg)
8400 LS	8.75" (22.23 cm)	19" (48.26 cm)	20" (50.8 cm)	24.0 lbs (10.9 kg)
8400 RP	12.25" (31.12 cm)	19" (48.26 cm)	21" (53.34 cm)	39.0 lbs (17.7 kg)
8400 IFC	3.35" (8.51 cm)	3" (7.62 cm)	14" (35.56 cm)	1.75 lbs (0.8 kg)
8400 PCU	7" (17.78 cm)	4.125" (10.48 cm)	16" (40.64 cm)	12.25 lbs. (5.6 kg)
8400 SDU	7" (17.78 cm)	2" (5.08 cm)	16" (40.64 cm)	4.5 lbs. (2 kg)
8400 PIU	Same as SDU			
8400 AIU	Same as SDU			

1.3 Measurement Overview

Measurement	Channels per Mainframe	Resolution	Accuracy	Range
Air Pressure Scanning	4096	14 Bits-Std	=0.1%F.S.	10"WC to 2.5 PSID
		16 Bits-Opt.	=0.05%F.S.	5 PSID to 500 PSID
All Media	48	14-Bits	=0.25%F.S. typical	1.5 to 6,000 PSIA or PSIG
High Accuracy Pressure	4	=0.0001 PSID	=.02%F.S.	1.5 PSID,15 to 500 PSIA
Pressure Calibration	4	=0.001 PSI	=0.02%F.S.	1.5 PSID,15 to 500 PSIA
Analog Input	128	14 Bits-Std	=0.12%F.S. to =0.04% F.S.	=10mv to =10v

F.S. = Full Scale

1.4 System Overview

The primary elements of a high speed pressure scanning system are the SP, Pressure Calibration Units (PCU), SDU, and pressure scanners. The SP is connected to the user's host computer via an IEEE-488 interface. The host computer interfaces the user to the 8400 SP, issues all high level commands, and directs the flow of data within the system. The host computer can range from a small PC to a large mainframe computer.

The SP (Figure 1.2) provides all control and data reduction functions for the System 8400. A 32-bit microprocessor, VME Bus, parallel processing, and comprehensive firmware programs provide a high speed environment.

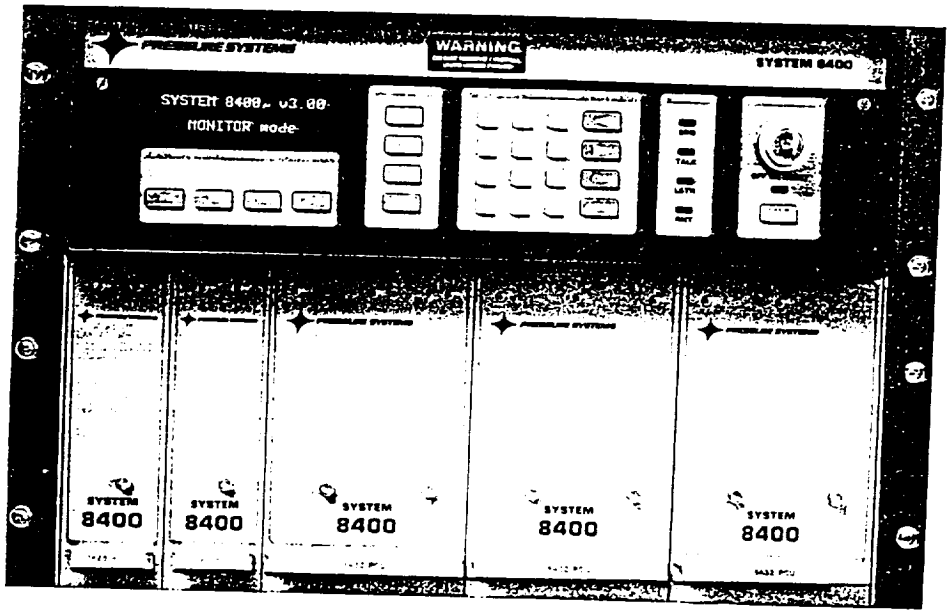

Figure 1.2: 8400 SP With Plug-in Units

To analyze a complex aerodynamic model, such as in a gas turbine development engine, a variety of parameters must be measured, such as pressure, temperature, flow, speed, torque, etc. Each parameter is important in evaluating engine performance. Gas turbine component tests (compressor, turbine, and inlet systems) generally have the same requirements, with perhaps an even greater quantity of pressure measurements. A sample pressure measurement configuration is illustrated in Figure 1.3, for a typical turbine engine application requiring 384 pressure channels, with full scale ranges of 5, 15, 50 and 100 PSIA, at a sampling rate of 50 KHz.

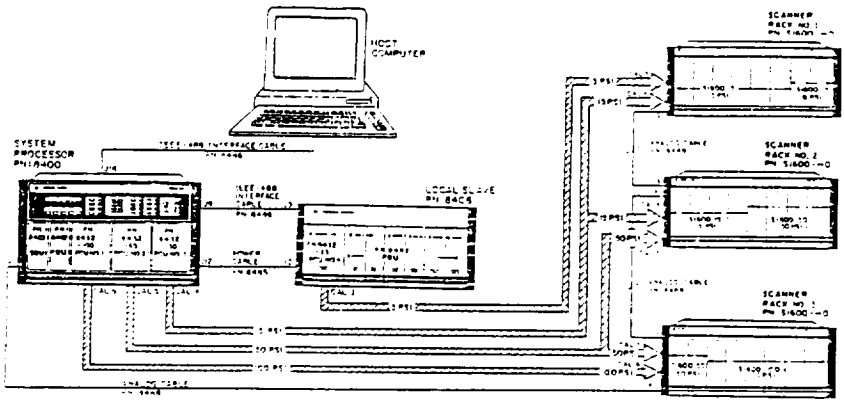

Figure 1.3: Typical Gas Turbine Engine Test Configuration

A SDU (PSI P/N: 8425) is in Slot 1 of the SP. Four ranges of transducers are required for the application, so four PCU's (PSI P/N: 8432) are needed. Three PCUs can be located in the SP, and a Local Slave (LS) houses the remaining unit. The SP is connected to the user's host computer via an IEEE-488 interface cable (PSI P/N: S486). The SP interfaces to the LS via a separate IEEE-488 bus, and provides power to the LS via a power supply cable (PSI P/N: 8485).

A total of 24 S1600-HD rack mounted pressure scanners are needed for 384 pressures. Three eight-slot scanner interface racks (PSI P/N: S1600-HD-RK) are needed to house the 24 scanners. The first rack of scanners is connected to the SP by an analog cable (PSI P/N: 8488). Each subsequent scanner rack is connected to the previous rack via analog cables (PSI P/N: 8488). The maximum distance from the SDU to the furthest rack can be 300 feet. However, in this application, both the SP and scanners are to be located in adjacent cabinets in the engine control room.

Each PCU consists of pneumatic valving, servo control and a high accuracy pressure transfer standard. Under SP control, the PCU switches the calibration valve within the scanners to the calibrate position and applies two to five calibration pressures to each scanner. The SP reduces the calibration data, and a characteristic equation as shown below is generated for each transducer.

$$P_x = C_0 + C_1V_x + C_2V_x^2 + C_3V_x^3 + C_4V_x^4$$

Where:

C_0, C_1, C_2, C_3 and C_4 are calibration coefficients.
V_x is a voltage reading at P_x; and,
P_x is an unknown pressure to be measured.

The calibration pressures are measured accurately by the PCU's pressure transfer standard. The host computer must specify the five pressures to set, the scanners to be calibrated, and then follow with the calibration command. The PCU sets the required pressures, the SDU reads the transducer voltages at each pressure, and the SP signals the host when the calibration is finished.

The coefficients for each transducer are stored in the SP. If the user elects to transfer Engineering Units (EU) data to the host after data acquisition, the SP uses the coefficients for conversion. Raw calibration data and coefficients can be sent to the host when the user intends to perform EU calculations in the host. For maximum throughput, subsequent pressure data can be sent to the host in raw binary form for later conversion. Single point and average data may be acquired and output to the host.

See Appendix E for more sample configurations.